

AD-A127 014

AEROELASTIC PROPERTIES OF STRAIGHT AND FORWARD SWEPT

1/2

GRAPHITE/EPOXY WINGS(U) AIR FORCE INST OF TECH

WRIGHT-PATTERSON AFB OH B J LANDSBERGER FEB 83

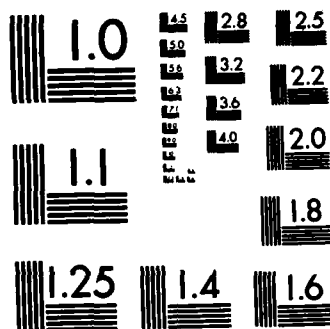
UNCLASSIFIED

AFIT/CI/NR-83-11T

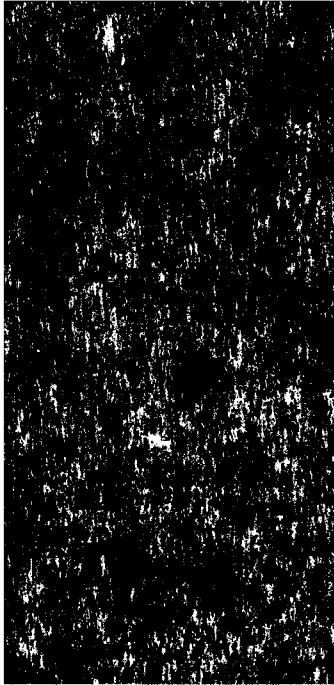
F/G 28/4

NL





MICROCOPY RESOLUTION TEST CHART
NATIONAL BUREAU OF STANDARDS-1963-A



UNCLASS

CLASSIFICATION OF THIS PAGE (When Data Entered)

①

REPORT DOCUMENTATION PAGE

READ INSTRUCTIONS
BEFORE COMPLETING FORM

1. REPORT NUMBER AFIT/CI/NR 83-11T	2. GOVT ACCESSION NO 112 / 114	3. RECIPIENT'S CATALOG NUMBER
4. TITLE (and Subtitle) Aeroelastic Properties of Straight and Forward Swept Graphite/Epoxy Wings		5. TYPE OF REPORT & PERIOD COVERED THESIS/DISSERTATION
7. AUTHOR(s) Brian Jerome Landsberger		6. PERFORMING ORG. REPORT NUMBER
9. PERFORMING ORGANIZATION NAME AND ADDRESS AFIT STUDENT AT: Massachusetts Institute of Technology		8. CONTRACT OR GRANT NUMBER(s)
11. CONTROLLING OFFICE NAME AND ADDRESS AFIT/NR WPAFB OH 45433		10. PROGRAM ELEMENT, PROJECT, TASK AREA & WORK UNIT NUMBERS
14. MONITORING AGENCY NAME & ADDRESS (if different from Controlling Office)		12. REPORT DATE Feb 83
		13. NUMBER OF PAGES 158
		15. SECURITY CLASS. (of this report) UNCLASS
		15a. DECLASSIFICATION/DOWNGRADING SCHEDULE

16. DISTRIBUTION STATEMENT (of this Report)

APPROVED FOR PUBLIC RELEASE; DISTRIBUTION UNLIMITED

17. DISTRIBUTION STATEMENT (of the abstract entered in Block 20, if different from Report)

18. SUPPLEMENTARY NOTES

APPROVED FOR PUBLIC RELEASE: IAW AFR 190-17

10 April 83

Lynn E. Wolaver
LYNN E. WOLAVER
Dean for Research and
Professional Development
AFIT, Wright-Patterson AFB OH

19. KEY WORDS (Continue on reverse side if necessary and identify by block number)

20. ABSTRACT (Continue on reverse side if necessary and identify by block number)

ATTACHED

DTIC
COLLECTED
1983
E

AEROELASTIC PROPERTIES OF STRAIGHT AND
FORWARD SWEPT GRAPHITE/EPOXY WINGS

by

BRIAN JEROME LANDSBERGER
B.S., United States Air Force Academy
(1972)

SUBMITTED TO THE DEPARTMENT OF
AERONAUTICS AND ASTRONAUTICS IN PARTIAL
FULFILLMENT OF THE REQUIREMENTS FOR
THE DEGREE OF

MASTER OF SCIENCE

IN

AERONAUTICS AND ASTRONAUTICS

at the

MASSACHUSETTS INSTITUTE OF TECHNOLOGY
February, 1983

© Massachusetts Institute of Technology 1983



Accession For	
NTIS GRA&I	<input checked="checked" type="checkbox"/>
DTIC TAB	<input type="checkbox"/>
Unannounced	<input type="checkbox"/>
Justification	
By	
Distribution/	
Availability Codes	
Dist	Avail and/or Special
A	

Signature of
Author

Brian J Landsberger
Department of Aeronautics and Astronautics
December 14, 1982

Certified
by

John Dugundji
John Dugundji
Thesis Supervisor

Accepted
by

Harold Y. Wachman
Chairman, Departmental Graduate Committee

AEROELASTIC PROPERTIES OF STRAIGHT AND
FORWARD SWEPT GRAPHITE/EPOXY WINGS

by

BRIAN JEROME LANDSBERGER

Submitted to the Department of Aeronautics and Astronautics on December 14, 1982, in partial fulfillment of the requirements for the degree of Master of Science in Aeronautics and Astronautics.

ABSTRACT

The aeroelastic deformation, divergence and flutter behavior of rectangular, graphite/epoxy, cantilevered plate type wings at zero sweep and thirty degrees of forward sweep is investigated for incompressible flow. Since the wings have varying amounts of bending stiffness, torsion stiffness and bending-torsion stiffness coupling, they each have unique aeroelastic properties. A five mode Rayleigh-Ritz formulation is used to calculate the equation of motion. From this equation static deflection, steady airload deflection, divergence velocities, natural frequencies and flutter velocities are calculated. Experimental two dimensional lift and drag curve data and approximations to three dimensional aerodynamics are used to calculate the aerodynamic forces for the steady airload analysis. The Weissinger L-Method for three dimensional aerodynamic forces is used in the divergence analysis. The V-g method is used to make flutter and natural frequency calculations. Tests on a static loading apparatus gave static deflections, while wind tunnel tests gave steady airload deflections for the wings at zero sweep, and divergence and flutter behavior data for all wings at both zero sweep and thirty degrees forward sweep. Wings were tested from zero to twenty degrees angle of attack for airspeeds up to divergence, flutter or the thirty meter per second limit of the tunnel.

Static deflection, natural frequencies, steady airload, divergence and flutter for the straight wing were predicted reasonably well by the theoretical calculations. For the swept forward wings, calculated flutter speeds were beyond the wind tunnel capabilities, while calculated divergence speeds were reasonable when divergence did occur. When swept forward, before reaching predicted divergence speeds some lightly bending-torsion stiffness coupled wings went into a torsional flutter, characterized by a large average bend which caused a high wing tip angle of attack. This flutter was not predicted by the theory used. The different wings exhibited markedly different stall flutter characteristics.

Thesis Supervisor: John Dugundji

Title: Professor of Aeronautics and Astronautics

ACKNOWLEDGEMENTS

I thank Professor John Dugundji for his continuous guidance during all phases of this project. I also thank Rob Dare, a fellow student, who assisted me during all experimental work.

Finally, to all the staff of M.I.T. who's instruction and assistance made this project possible, and to the United States Air Force which funded my education and the contract covering this project, a hearty thank you.

TABLE OF CONTENTS

	<u>Page</u>
List of Figures.....	6
List of Tables.....	7
List of Symbols.....	8
 <u>Chapter</u>	
1. Introduction.....	11
2. Theory	
2.1 Rayleigh-Ritz Analysis.....	12
2.2 Static Deflection Analysis.....	23
2.3 Steady Airload Analysis.....	25
2.4 Divergence Analysis.....	34
2.5 Flutter Analysis.....	44
3. Experiments	
3.1 Test Wing Selection.....	60
3.2 Static Deflection Tests.....	61
3.3 Wind Tunnel Test Setup.....	63
3.4 Natural Frequency Tests.....	66
3.5 Steady Airload Tests.....	66
3.6 Flutter Boundary Tests.....	67
3.7 Flutter Tests.....	67
4. Results	
4.1 Static Deflection.....	70
4.2 Steady Airload Deflection.....	73
4.3 Divergence Velocities.....	76
4.4 Natural Frequencies.....	78
4.5 Flutter Velocities.....	79

5. Conclusions and Recommendations.....	86
---	----

6. References and Bibliography.....	88
-------------------------------------	----

Appendices

A. Mode Shape Integrals and Their Numerical Values.....	90
---	----

B. Static Deflection Investigation Results.....	97
---	----

C. Steady Airload Investigation Results.....	105
--	-----

D. Flutter Investigation Results.....	119
---------------------------------------	-----

About the Author.....	158
-----------------------	-----

LIST OF FIGURES

<u>Figure</u>	<u>Page</u>
2.1 Wing coordinate system.....	12
2.2 Graph of k_{nT} vs. β	22
2.3 Flexible wing twist feedback system diagram.....	25
2.4 Lift and drag curves for a flat plate.....	26
2.5 Components of force for a wing at angle of attack.....	27
2.6 Approximation to the C_f curve.....	28
2.7 Approximation for the C_p curve.....	29
2.8 Center of pressure movement with changes in angle of attack.....	30
2.9 Spanwise lift distribution for various twist conditions for a straight wing.....	32
2.10 Changes in force due to drag with changes in angle of attack.....	33
2.11 Lift distribution in the spanwise x direction using the Weissinger L-Method.....	39
2.12 Swept forward wing coordinate system.....	40
3.1 Static deflection test apparatus.....	61
3.2 Static test stand with a moment being applied.....	62
3.3 M.I.T. wind tunnel setup.....	63
3.4 Looking down on a test wing by using a mirror.....	64
3.5 Equipment used to illuminate and record test data.....	65
3.6 Double exposure showing extremes of flutter motion.....	69
4.1 Static deflection test results for $[\pm 15/0]_s$ layup wing.....	71
4.2 Initial camber (exaggerated) in the $[\pm 15/0]_s$ layup wing.....	72
4.3 Steady airload analysis on the four wings with a 15 degree ply fiber angle.....	73
4.4 Flutter analysis diagrams for the four wings with a 15 degree ply fiber angle.....	82
4.5 Effects of ply fiber angle on flutter and divergence speeds.....	84

B.1 - B.7	Static deflection theoretical analysis and experimental data.....	98
C.1 - C.13	Steady airload theoretical analysis and experimental data.....	106
D.1 - D.8	Flutter boundary curves.....	124
D.9 - D.34	V-g method flutter analysis diagrams.....	132

LIST OF TABLES

<u>Table</u>	<u>Page</u>
2.1	Assumed modes used in the Rayleigh-Ritz analysis.....19
3.1	Different laminate layups used for the test wings.....60
4.1	Wing divergence speeds.....77
4.2	Wing natural frequencies.....78
D.1	Flutter data, unswept wing.....120
D.2	Flutter data, swept wing.....122

LIST OF SYMBOLS

Symbol

A	stress-strain modulus matrix; aerodynamic matrix
B	stress-bending modulus matrix
b	semi-chord of the wing
C	compliance matrix
c	chord of the wing
C _d	coefficient of drag
C _f	coefficient of force
C _l	coefficient of lift
C _m	coefficient of moment about the quarter chord
C _p	coefficient of pressure
cp	center of pressure
D	moment-bending modulus matrix
E _L	logitudinal Young's modulus
E _T	transverse Young's modulus
G _{LT}	shear modulus
g	structural damping
h	vertical deflection
K	stiffness matrix
k _{IT}	non-dimentional torsional stiffness
L	lift
l	length of wing from root to tip
L _A	lift associated with bending displacement
L _B	lift associated with torsional displacement
L _C	lift associated with chordwise displacement
M	moment per unit length; mass matrix
m	mass per unit area
M _A	moment associated with bending displacement
M _B	moment associated with torsional displacement
M _C	moment associated with chordwise displacement

N	force per unit length; chordwise force
N_A	chordwise body force associated with bending displacement
N_B	chordwise body force associated with torsional displacement
N_C	chordwise body force associated with chordwise displacement
P	distributed force per unit length
p	distributed force per unit area
Q_i	generalized external force
q	dynamic pressure
q_i	generalized coordinate
R	matrix used to transform K
S	matrix used to transform K
T	kinetic energy
V	potential (strain) energy; velocity
V_∞	free stream velocity
W	weighting matrix
w	deflection in the z direction
x	} cartesian coordinates
y	
z	
x	spanwise axis
y	chordwise axis
α	angle of attack
α_i	beam bending mode constant
β	warping stiffness parameter
γ_{xy0}	shear strain tensor at midplane
γ_i	Rayleigh-Ritz mode
δ_{ij}	delta function
ϵ_{x0}	strain tensor in the x direction at midplane
ϵ_{y0}	strain tensor in the y direction at midplane
ϵ_i	beam bending mode constant

θ	ply fiber angle; twist angle
κ_x	} curvature strain tensors
κ_y	
κ_{xy}	
Λ	wing sweep angle
ν_{LT}	Poisson's ratio
ξ	chordwise deflection
ρ	air density
ϕ	Rayleigh-Ritz mode shape part that is a function of x
ψ	Rayleigh-Ritz mode shape part that is a function of y

CHAPTER 1. INTRODUCTION

The use of composite materials in aircraft structures has added another design dimension to the aircraft designer. Useful not only for their high strength to weight ratio but by giving the designer the ability to vary the force deflection behavior by varying the layup scheme, they have made certain previously impractical design options attractive. In particular, forward swept wings have gained renewed interest because their major drawback, low wing divergence speeds, can be significantly improved by using tailored composite material in wing construction. A good discussion of this is contained in reference 1.

This project will draw on the work of four previous experimenters at M.I.T.; Hollowell, Jensen, Selby and Dugundji (references 2,3,4 and 5). Those men worked with some of the same wings that were used in this project. They made calculations and ran experiments to determine the wing stiffness and bending-torsion stiffness coupling, the steady airload deflection behavior and the flutter and divergence speeds at low and high angles of attack. Using their work as a foundation, we will extend its range by investigating several new ply angle layup patterns and by investigating aeroelastic properties at 30 degrees forward sweep. Primary interest is in the investigation of divergence and flutter speeds and the wing shapes during those conditions at both low and high angle of attack. Low angle of attack flutter is investigated both theoretically and experimentally while high angle of attack flutter investigation is experimental only. We also extend the work of Hollowell on steady airload deflection analysis by including a realistic non-linear lift curve, drag and approximations to three dimensional aerodynamics.

CHAPTER 2. THEORY

2.1 Rayleigh-Ritz Analysis

In this research both static and dynamic analysis are done using the Rayleigh-Ritz analysis technique. We therefore need to formulate an equation of motion for the dynamic analysis and then by setting the time derivatives equal to zero, we can use the same equation for the static analysis. Because of the complicated nature of anisotropic material, exact analysis is difficult and often impossible. Therefore I chose an approximate method of analysis, the assumed mode or so called Rayleigh-Ritz method. This is the same method used by Hollowell, Jensen and Selby (references 2, 3 and 4) who were mentioned in the introduction and in fact, due to the amount of work already done on these wings with this method I decided to use the same assumed modes in my analysis.

The analysis is linear and assumes all deflections are perpendicular to the wing in the z direction as shown in figure 2.1.

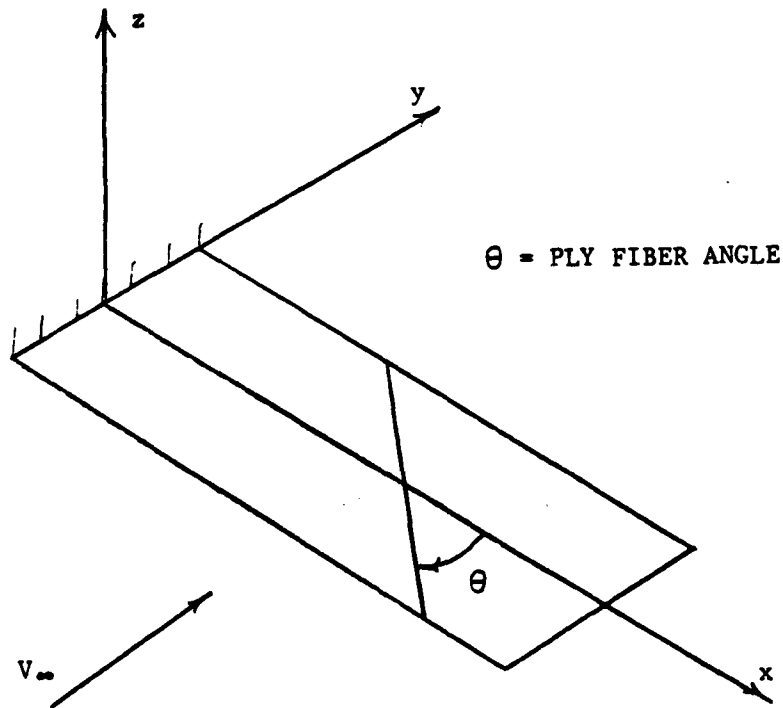


Figure 2.1 Wing coordinate system.

Note that the ply fiber angle is measured in the opposite direction as compared to the standard composite material direction.

The basic equation for the assumed modes is:

$$w(x,y,t) = \sum_{i=1}^n \gamma_i(x,y) q_i(t) \quad (2.1)$$

Where $\gamma_i(x,y)$ are the modes. In our case we have five modes so $n=5$. To get the equation of motion we start with Lagrange's equation.

$$\frac{d}{dt} \left(\frac{\partial T}{\partial \dot{q}_r} \right) - \frac{\partial T}{\partial q_r} + \frac{\partial V}{\partial q_r} = Q_r \quad \left\{ \dot{q} = \frac{\partial q}{\partial t} \right\} \quad (2.2)$$

Where Q represents the applied loads.

Now we need expressions for the kinetic and potential energies. For the kinetic energy of a plate we have:

$$T = \frac{1}{2} \int \int m (\dot{w})^2 dA \quad (2.3)$$

Where m = mass/unit area.

Using equation (2.1) for w we get:

$$T = \frac{1}{2} \int \int m \left[\sum_{i=1}^n \gamma_i \dot{q}_i \right] \cdot \left[\sum_{j=1}^n \gamma_j \dot{q}_j \right] dA \quad (2.4)$$

Moving summations and grouping terms:

$$T = \frac{1}{2} \sum_i^1 \sum_j^j M_{ij} \dot{q}_i \dot{q}_j \quad (2.5)$$

where $M_{ij} = \iint \gamma_i m \gamma_j dA \quad (2.6)$

The variational potential energy for a plate is:

$$\delta V = \iint \left(N_x \delta \epsilon_{x_0} + N_y \delta \epsilon_{y_0} + N_{xy} \delta \gamma_{xy_0} + M_x \delta \kappa_x + M_y \delta \kappa_y + M_{xy} \delta \kappa_{xy} \right) dx dy \quad (2.7)$$

where using conventional displacement notation:

$$\begin{aligned} \epsilon_{x_0} &= \frac{\partial u}{\partial x} & \kappa_x &= - \frac{\partial^2 w}{\partial x^2} \\ \epsilon_{y_0} &= \frac{\partial v}{\partial y} & \kappa_y &= - \frac{\partial^2 w}{\partial y^2} \\ \gamma_{xy_0} &= \frac{\partial u}{\partial y} + \frac{\partial v}{\partial x} & \kappa_{xy} &= - 2 \frac{\partial^2 w}{\partial x \partial y} \end{aligned} \quad (2.8)$$

To apply this to anisotropic plates we start with the modulus equations for the general laminate.

$$\begin{Bmatrix} N \\ M \end{Bmatrix} = \begin{bmatrix} A & B \\ B & D \end{bmatrix} \begin{Bmatrix} \epsilon \\ \kappa \end{Bmatrix} \quad (2.9)$$

N = Force/length vector
 M = Moment/length vector
 ϵ = strain vector
 κ = curvature strain vector
 A, B, D are the appropriate modulus matrices

Since this is for a plate we assume no strain or shear in the z direction. For a symmetric laminate, moments about x any y do not cause strain, only bending so $B = 0$. In our analysis all loads are in the z direction so $N = 0$, leaving us with, in expanded form:

$$\begin{Bmatrix} M_x \\ M_y \\ M_{xy} \end{Bmatrix} = \begin{bmatrix} D_{11} & D_{12} & D_{16} \\ D_{21} & D_{22} & D_{26} \\ D_{61} & D_{62} & D_{66} \end{bmatrix} \begin{Bmatrix} \kappa_x \\ \kappa_y \\ \kappa_{xy} \end{Bmatrix} \quad (2.10)$$

Using equation (2.10) for M , integrating with respect to the variational terms and using equations (2.8) for the curvatures we get:

$$V = 1/2 \iint \begin{bmatrix} -w_{,xx} & -w_{,yy} & -2w_{,xy} \end{bmatrix} \begin{bmatrix} D_{11} & D_{12} & D_{16} \\ D_{21} & D_{22} & D_{26} \\ D_{61} & D_{62} & D_{66} \end{bmatrix} \begin{Bmatrix} -w_{,xx} \\ -w_{,yy} \\ -2w_{,xy} \end{Bmatrix} \quad (2.11)$$

where:

$$w_{,xx} = \frac{\partial^2 w}{\partial x^2}, \text{ etc.}$$

expanding this equation and using $D_{21}=D_{12}$, $D_{16}=D_{61}$ and $D_{26}=D_{62}$:

$$\begin{aligned} V = \frac{1}{2} \iint \{ & D_{11} w_{,xx}^2 + 2 D_{12} w_{,xx} w_{,yy} + D_{22} w_{,yy}^2 + 4 D_{66} w_{,xy}^2 \\ & + 4 D_{16} w_{,xx} w_{,xy} + 4 D_{26} w_{,yy} w_{,xy} \} dA \end{aligned} \quad (2.12)$$

We now substitute in equation (2.1) for w bring summations and q 's out of the integral to get:

$$\begin{aligned} V = \frac{1}{2} \sum_{i=1}^I \sum_{j=1}^J q_i q_j \iint \{ & D_{11} Y_{i,xx} Y_{j,xx} + 2 D_{12} Y_{i,xx} Y_{j,yy} \\ & + D_{22} Y_{i,xx} Y_{j,yy} + 4 D_{66} Y_{i,xy} Y_{j,xy} + 4 D_{16} Y_{i,xx} Y_{j,xy} \\ & + 4 D_{26} Y_{i,yy} Y_{j,xy} \} dA \end{aligned} \quad (2.13)$$

Finally it is rewritten in the compact form:

$$V = \frac{1}{2} \sum_{i=1}^I \sum_{j=1}^J K_{ij} q_i q_j \quad (2.14)$$

where

$$\begin{aligned}
 K_{ij} = \int \int \{ & D_{11} \gamma_{i,xx} \gamma_{j,xx} + D_{22} \gamma_{i,yy} \gamma_{j,yy} + 4D_{66} \gamma_{i,xy} \gamma_{j,xy} \\
 & + D_{12} (\gamma_{i,xx} \gamma_{j,yy} + \gamma_{j,xx} \gamma_{i,yy}) \\
 & + 2D_{16} (\gamma_{i,xx} \gamma_{j,xy} + \gamma_{j,xx} \gamma_{i,xy}) \\
 & + 2D_{26} (\gamma_{i,yy} \gamma_{j,xy} + \gamma_{j,yy} \gamma_{i,xy}) \} dA
 \end{aligned} \quad (2.15)$$

Note that K_{ij} is symmetric.

Now we can put our expressions for T and V in equation (2.2). First for kinetic energy:

$$\frac{\partial T}{\partial \dot{q}_r} = \frac{1}{2} \sum_i^i \sum_j^j M_{ij} \left(\frac{\partial \dot{q}_i}{\partial \dot{q}_r} \dot{q}_j + \frac{\partial \dot{q}_j}{\partial \dot{q}_r} \dot{q}_i \right)$$

using $\frac{\partial \dot{q}_i}{\partial \dot{q}_r} = \delta_{ir}$ and expanding

$$\frac{\partial T}{\partial \dot{q}_r} = \frac{1}{2} \sum_i^i M_{rj} \dot{q}_j + \frac{1}{2} \sum_j^j M_{ir} \dot{q}_i \quad (2.17)$$

since M is symmetric we can sum the two parts:

$$\frac{\partial T}{\partial \dot{q}_r} = \sum_j^j M_{rj} \dot{q}_j \quad (2.18)$$

similarly for potential energy:

$$\frac{\partial V}{\partial q_r} = \sum_j^j K_{rj} q_j \quad (2.19)$$

finally

$$\frac{d}{dt} \frac{\partial T}{\partial \dot{q}_r} = \sum_j^j m_{rj} \ddot{q}_j$$

We note that:

$$\frac{\partial T}{\partial q_r} = 0$$

and put these into Lagranges equation, using $r=i$:

$$\sum_j^j m_{ij} \ddot{q}_j + \sum_j^j k_{ij} q_j = Q_i \quad (j = 1, 2, \dots, N) \quad (2.21)$$

in matrix form:

$$\underline{M} \ddot{\underline{q}} + \underline{K} \underline{q} = \underline{Q} \quad (2.22)$$

This equation will be used to derive all the displacements and motion of the wings. The five mode shapes used are listed on table (2.1) where the variables have been separated in the form:

$$\gamma_i(x, y) = \phi_i(x) \psi_i(y)$$

<u>Mode</u>	<u>$\phi_i(x)$</u>	<u>$\psi_i(y)$</u>
1.	$\cosh \left(\frac{\epsilon_1 x}{l} \right) - \cos \left(\frac{\epsilon_1 x}{l} \right)$ $- \alpha_1 \left\{ \sinh \left(\frac{\epsilon_1 x}{l} \right) - \sin \left(\frac{\epsilon_1 x}{l} \right) \right\}$	1
2.	$\cosh \left(\frac{\epsilon_2 x}{l} \right) - \cos \left(\frac{\epsilon_2 x}{l} \right)$ $- \alpha_2 \left\{ \sinh \left(\frac{\epsilon_2 x}{l} \right) - \sin \left(\frac{\epsilon_2 x}{l} \right) \right\}$	1
3.	$\sin \left(\frac{\pi x}{2l} \right)$	$\frac{y}{c}$
4.	$\sin \left(\frac{3\pi x}{2l} \right)$	$\frac{y}{c}$
5.	$\frac{x}{l} \left(1 - \frac{x}{l} \right)$	$\left(\frac{4y}{c^2} - \frac{1}{3} \right)$

where:

$$\epsilon_1 = 1.8785104$$

$$\alpha_1 = 0.734096$$

$$\epsilon_2 = 4.694091$$

$$\alpha_2 = 1.018466$$

Table 2.1 Assumed modes used in the Rayleigh-Ritz analysis.

The first two are cantilever beam bending modes the second two are beam torsion modes and the fifth is a chordwise bending mode. You may notice that modes 3 & 4 do not meet the boundary conditions for a cantilevered plate at the root where w, x is zero. But the error is small away from the root and an aspect ratio correction for this is made

in the stiffness matrix terms. Jensen in reference 3 goes through in detail the algebra for working out the mass and stiffness matrix terms and he also derives the torsion stiffness correction factor. In this report only the results are stated.

Mass Coefficients

$$\begin{aligned} M_{11} &= mcl I_1 & M_{33} &= \frac{mcl}{12} I_3 & M_{55} &= \frac{4mcl}{45} I_5 \\ M_{22} &= mcl I_2 & M_{44} &= \frac{mcl}{12} I_4 & M_{ij} &= 0 \quad i \neq j \end{aligned}$$

Stiffness Coefficients

$$\begin{aligned} K_{11} &= \frac{D_{11}^c}{l^3} I_6 & K_{22} &= \frac{D_{11}^c}{l^3} I_{10} & K_{34} &= 0 \\ K_{12} &= 0 & K_{23} &= \frac{2D_{26}}{l^2} I_{11} & K_{35} &= \frac{4D_{16}}{3l^2} I_{16} + \frac{16D_{26}}{c^2} I_{17} \\ K_{13} &= \frac{2D_{16}}{l^2} I_7 & K_{24} &= \frac{2D_{16}}{l^2} I_{12} & K_{44} &= \frac{4D_{66}}{cl} I_{19} \left(\frac{k_{2T}}{3\pi/2} \right)^2 \\ K_{14} &= \frac{2D_{16}}{l^2} I_8 & K_{25} &= \frac{8D_{16}}{cl} I_{13} & K_{45} &= \frac{4D_{16}}{3l^2} I_{20} + \frac{16D_{26}}{2} I_{21} \\ K_{15} &= \frac{8D_{12}}{cl} I_9 & K_{33} &= \frac{4D_{66}}{cl} I_{15} \left(\frac{k_{1T}}{\pi/2} \right)^2 \\ K_{55} &= \frac{4D_{11}^c}{45l^3} I_{22} + \frac{64D_{22}^l}{c^3} I_5 + \frac{64D_{66}}{3cl} I_{23} \end{aligned}$$

Where the original values for K_{33} and K_{44} were changed using the aspect ratio correction worked out by Crawley and Dugundji (contained in reference 4).

where:

$$\beta = \frac{D_{11}c^2}{48D_{66}l^2}$$

And the values of k_{nT} ($n = 1, 2$) are plotted vs. β in figure 2.2.

The integrals and their values are listed in table 2.1.

For our particular wings, values of D_{ij} were calculated using the material constants listed below.

$$E_L = 98 \times 10^9 \text{ N/m}^2$$

$$E_T = 7.9 \times 10^9 \text{ N/m}^2$$

$$\nu_{LT} = 0.28$$

$$G_{LT} = 5.6 \times 10^9 \text{ N/m}^2$$

$$\text{wing thickness} = .804 \text{ mm}$$

$$\text{density of wing} = 1520 \text{ kg/m}^3$$

The engineering constants are for Hercules ASI/3501-6 graphite/epoxy for out-of-plane loading (see reference 5 for an explanation on the differences in the engineering constants for in plane and out of plane loading).

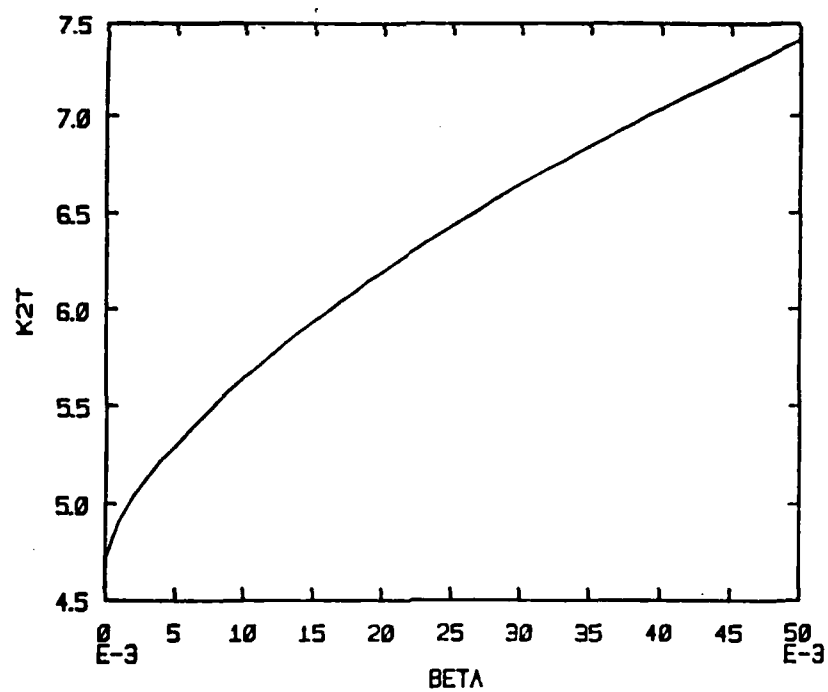
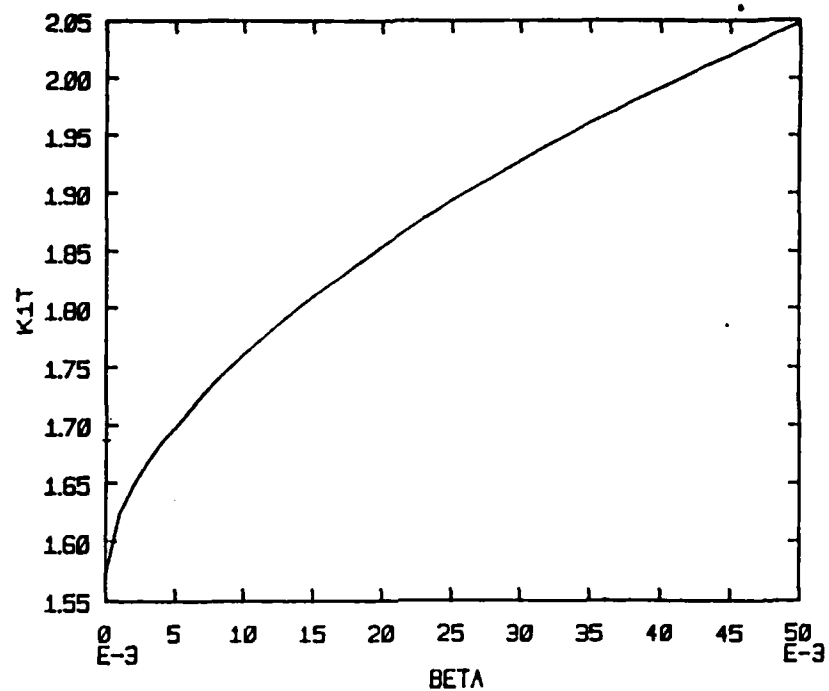


Figure 2.2 Graph of k_{nT} vs. β .

2.2 Static Deflection Analysis

For static loading, all inertia terms in equation (2.22) are zero so we have left:

$$\underline{K} \underline{q} = \underline{Q} \quad (2.23)$$

\underline{Q} is the modal force where:

$$Q_r = \iint p \gamma_r dA \quad (2.24)$$

where p is a distributed load per unit area.

For our tests the load was applied at $x = l$ so we have:

$$\begin{aligned} Q_r &= \int_{-c/2}^{c/2} \int_0^l p(x,y) \delta(x-l) \gamma_r(x,y) dA \\ &= \int_{-c/2}^{c/2} P(l,y) \gamma_r(l,y) dy \end{aligned} \quad (2.25)$$

where P is the load per unit length.

For the bending load the apparatus used was assumed to apply a

load constant in the y direction so we can take P out of the integral.

$$Q_r = P \int_{-c/2}^{c/2} \gamma_r(l, y) dy \quad (2.26)$$

Now we need only insert the five modes to get the five values of Q_r . They are listed below.

$$Q_1 = 2Pc$$

$$Q_2 = -2Pc$$

$$Q_3 = Q_4 = Q_5 = 0$$

For the torsional load the test apparatus was assumed to apply load linear to y such that:

$$p = ay$$

where a is a constant.

Our equation becomes:

$$Q_r = a \int_{-c/2}^{c/2} y \gamma_r(l, y) dy \quad (2.27)$$

Again, putting in the five modes we get:

$$Q_1 = Q_2 = Q_5 = 0$$

$$Q_3 = \frac{ac^2}{12}$$

$$Q_4 = -\frac{ac^2}{12}$$

The values for Q were calculated and put into equation (2.23) which was solved for the column vector q . The values of q were then put into equation (2.1) to get the analytical deflection. The results are shown together with the experimental data on figure B.1 to B.7.

2.3 Steady Airload Analysis.

When put in an airstream at a given angle of attack a wing generates airforces, indeed this is its purpose. These airforces not only support the weight of the airplane but they also bend and twist the wing itself. This deformation of the wing, in return, by changing the angle of attack, changes the airforces on the wing. The result, shown in figure (2.3) is a simple feedback system.

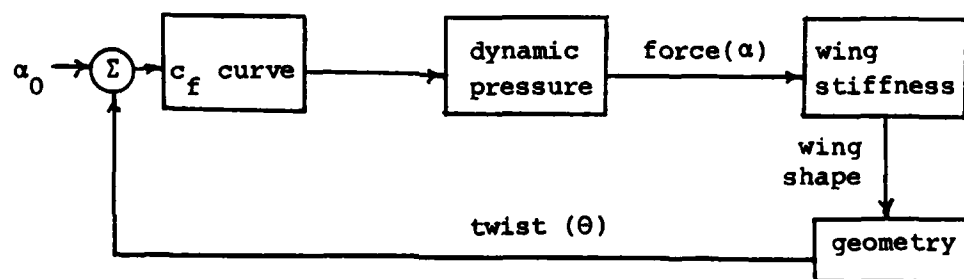


Figure 2.3 Flexible wing twist feedback system diagram.

When the loop converges to a certain value we have the final deflection. In certain linear theory analysis when the airspeed is increased beyond a critical value the loop does not converge and airforces and deflection increase without limit. This is called divergence. In the real world there are limits to the actual increase in deflection and airforces. They come about due to destruction of the wing, non-linear stiffness of the wing or non-linear increase of airload with increases in the angle of attack. With our wings the most important non-linearity, especially at airspeeds at and below the divergence airspeed, is the non-linear increase of airload with angle of attack.

For the steady airload analysis we put in this non-linearity by using the lift and drag curves for a flat plate from reference 10 shown in figure 2.4.

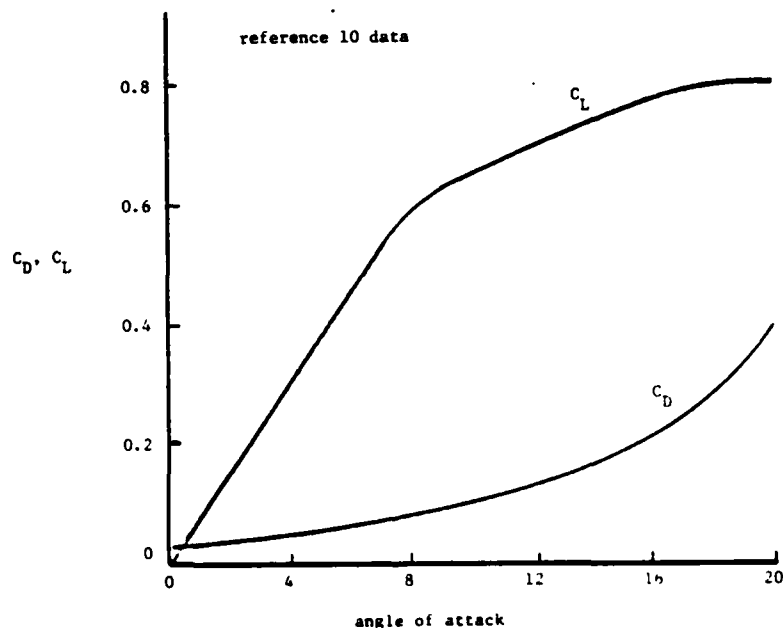


Figure 2.4 Lift and drag curves for a flat plate.

The force that deflects the wing is the force perpendicular to the wing (in the z direction). This force has a component from lift and drag dependent on angle of attack as shown in figure 2.5.

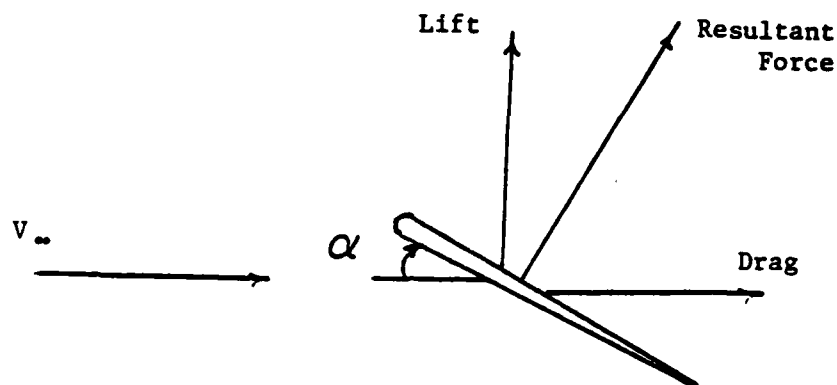


Figure 2.5 Components of force for a wing at angle of attack α .

From figure 2.5 we get:

$$C_f = C_l \cos \alpha + C_d \sin \alpha \quad (2.28)$$

For the lift component of force, I made a $C_{f(\text{lift})}$ vs. α curve. This curve was approximated by a polynomial of the form:

$$C_{f(\text{lift})} = \sum_{i=1}^n A_i \alpha^i \quad (2.29)$$

For our purposes $n = 4$ gave a sufficiently accurate curve. Both the coefficient of force curve and the polynomial approximation are shown in figure 2.6.

$$C_f = -37.7072\alpha^4 + 42.472\alpha^3 - 23.167\alpha^2 + 6.6746\alpha \quad \{\alpha \text{ in radians}\} \quad (2.30)$$

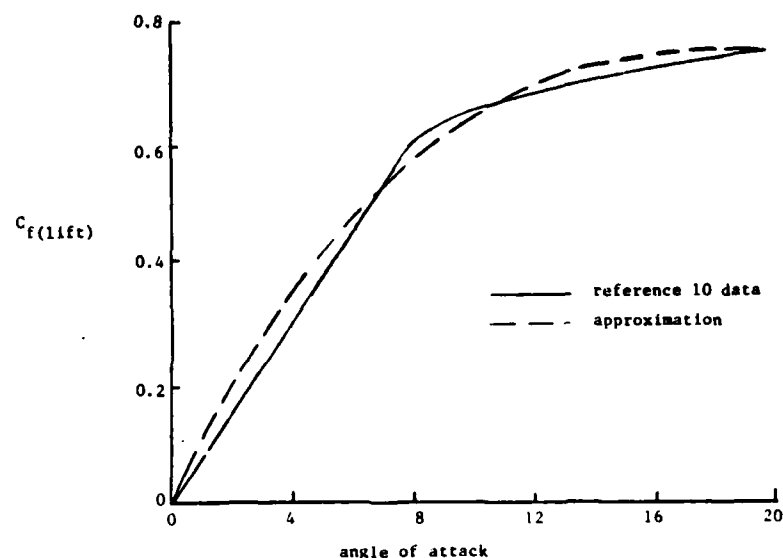


Figure 2.6 Approximation for the C_f curve.

This gives the section coefficient of force from lift as a function of angle of attack but we also need to know the dependance on x and y , or in other words, force distribution on the wing. In reference 4 Selby showed the lift distribution of a rigid wing. This was used as a guide for modeling the force distribution on our wing. Again a polynomial approximation was used. The distribution in the chordwise y

direction and the approximation are shown in figure 2.7 as coefficients of pressure versus chord.

Approximation equation for force distribution in the chordwise y direction:

$$C_p = C_{p \text{ avg}} \cdot 3(0.5 - y)^2 \quad (2.31)$$

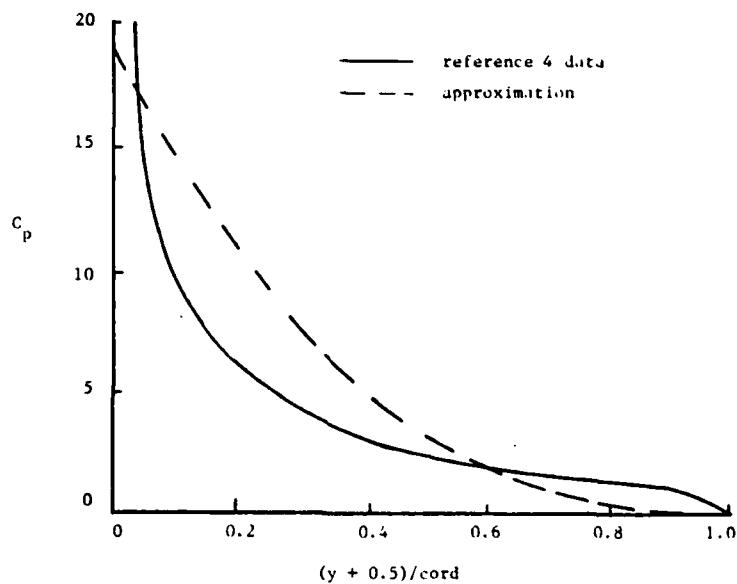


Figure 2.7 Approximation for the C_p curve.

Both the approximation and the theory give 25% chord as the center of pressure in the y direction. Reference 10 shows the coefficient of moment about the quarter chord vs. angle of attack. From this we can calculate the center of pressure movement with changing angle of attack by using:

$$C_m = (y_{cp} - y_{.25c}) C_l \quad (2.32)$$

where y_{cp} is the center of pressure location.

To approximate this, a modification was made to equation (2.31). The center of pressure movement and its approximation are shown in figure 2.8.

Approximation equation for force distribution in the chordwise y direction with a correction for c_p movement:

$$C_p = C_{p \text{ avg}} (3.5 - 5.71\alpha) \cdot (0.5 - y)^{2.5} + 1.63\alpha \quad (2.33)$$

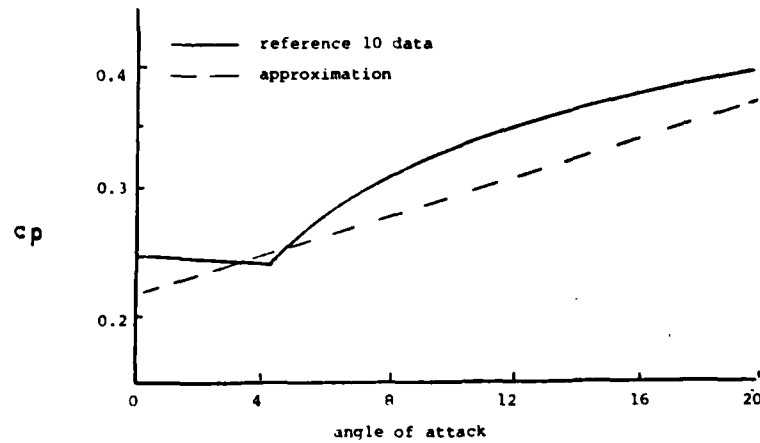


Figure 2.8 Center of pressure movement with changes in angle of attack.

In the spanwise x direction, the lift distribution was calculated using lifting line theory. I used the matrix equation given in reference 7.

$$\{ \alpha \} = \begin{bmatrix} 1 \\ \alpha_0 \end{bmatrix} + \frac{1}{8l} \begin{bmatrix} 1 \\ \sin\phi \end{bmatrix} \begin{bmatrix} r \sin r\phi \end{bmatrix} \begin{bmatrix} \sin r\phi \end{bmatrix}^{-1} \{ cC_l \} \quad (2.34)$$

where: $\alpha_0 = 2\pi$

c = chord

l = semi-span

$$\phi_m = \cos^{-1} \left(\frac{x_m}{l} \right)$$

$$r = (2n - 1)$$

n = column number

m = row number

The lift distribution was calculated for three cases, a rigid wing at 2 degrees angle of attack, a wing with positive twist of 4 degrees with the root angle of attack at 2 degrees and a wing with negative twist of 4 degrees with the root angle of attack at 6 degrees. These three cases span a good part of the low angle of attack deformation conditions for our wings. The three cases along with the approximation used are plotted in figure 2.9. The same approximation was used in all cases. Note that $C_{l_{\alpha}(\text{root})} = C_{l/\alpha}(\text{root})$

Approximation equation for force distribution in the spanwise x direction:

$$C_f = C_{f \text{ avg}} \cdot 1.11 \left\{ 1 - \left(\frac{x}{l} \right)^9 \right\} \quad (2.35)$$

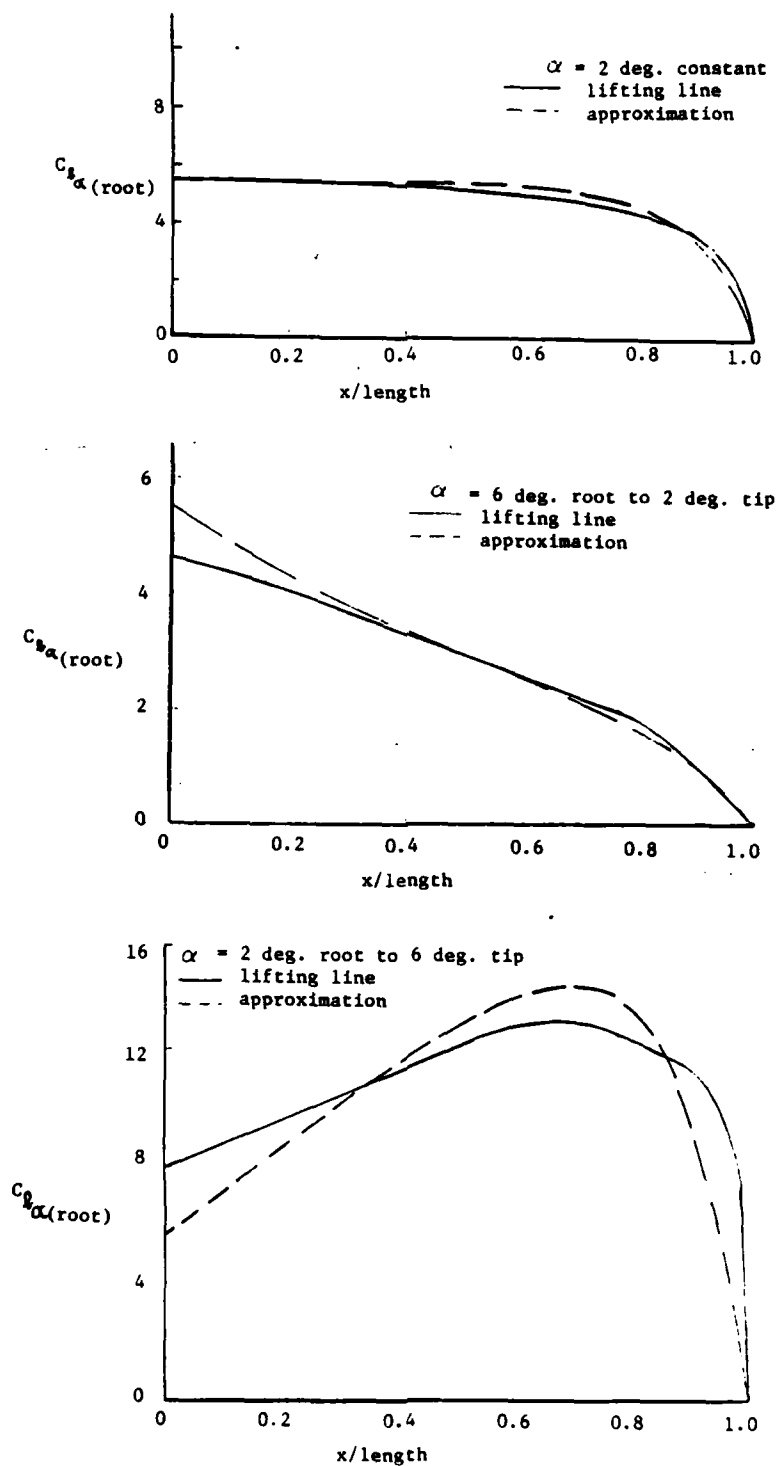


Figure 2.9 Spanwise lift distribution for various twist conditions for a straight wing ($\Lambda = 0$).

Finally, for drag I used the curve from reference 10 shown in figure 2.10 with its approximation. Drag was assumed to be a function of angle of attack only and not of x and y .

Approximation equation for force due to drag:

$$C_{f \text{ (drag)}} = C_d \sin \alpha = 3.5 \alpha^3 \quad (2.36)$$

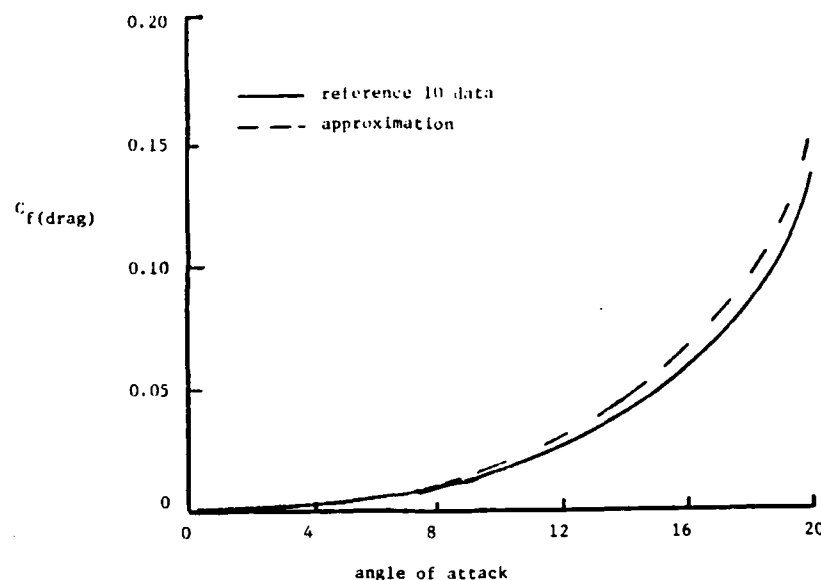


Figure 2.10 Change in force due to drag with changes in angle of attack

Putting all the approximations together we get a two dimensional force distribution on the wing where:

$$C_p = C_p \left(\alpha, \frac{x}{l}, \frac{y}{c} \right)$$

$$\begin{aligned}
C_p = & (A_4 \alpha^4 + A_3 \alpha^3 + A_2 \alpha^2 + A_1 \alpha) \\
& \cdot 1.11 \left[1 - \left(\frac{x}{l} \right) \right] \left\{ \left(3.5 - 5.71 \alpha \right) \left[0.5 - \left(\frac{y}{c} \right)^{2.5} \right] + 1.63 \alpha \right\} \\
& + 3.5 \alpha^3
\end{aligned} \tag{2.37}$$

For α , the vast majority of the twist (θ) is from the first assumed torsion mode so I used equation (2.38) for $\alpha = \alpha_0 + \theta$.

$$\alpha(x) = \alpha_0 + \sin^{-1} \left(\frac{q_3}{c} \right) \sin \left(\frac{\pi x}{2} \right) \tag{2.38}$$

This completes the distributed force coefficient term. Multiply this by dynamic pressure and we get the distributed force per unit area. This was put in the Rayleigh-Ritz analysis to get the modal force Q .

$$Q_r = \int_0^l \int_{-c/2}^{c/2} f(x,y) \gamma(x,y) dx dy \tag{2.40}$$

The equation was solved on a digital computer by numerical integration. Then equation (2.23) was solved for q . Solutions were calculated for three airspeeds 5, 11.5 and 16 meters per second at angles of attack from 2 to 20 degrees at 2 degree increments. If 16 m/s was higher than the wing divergence speed, I omitted the calculation at that speed. For 5 m/s three iterations were sufficient, for 11.5 m/s five iterations were sufficient and for 16 m/s up to seven iterations were used. The results for a straight wing ($\Lambda = 0$) are plotted along with experimental data in figures C.1 through C.13.

2.4 Wing Divergence Analysis.

Basically a wing diverges when the aerodynamic forces from increased angle of attack due to twist are stronger than the resisting

forces from the wing's torsional stiffness. When wings are swept, bending also causes changes in angle of attack while bending stiffness resists these changes.

To calculate divergence, therefore we need to relate the stiffness forces to the aerodynamic forces. In matrix form the torsional stiffness equation is :

$$\{ \theta \} = [C^{z\theta}] \{ F \} + [C^{\theta\theta}] \{ M \} \quad (2.41)$$

If the forces and moments can be combined to make a force at a specific chordwise point we get:

$$\{ \theta \} = [C] \{ F \} \quad (2.42)$$

The aerodynamic forces for a station along the span are:

$$l = cC_l q \quad \{ q = \text{dynamic pressure} \} \quad (2.43)$$

In matrix form we have:

$$\{ L \} = q [\bar{W}] \{ cC_l \} \quad (2.44)$$

Where $[\bar{W}]$ is a weighting matrix for the stations chosen and contains the appropriate amount of spanwise length to make the running lift the lift for the area covered by the station. In this case lift is the force in equation (2.42) so we have:

$$\{ \theta \} = [C] q [\bar{W}] \{ cC_l \} \quad (2.45)$$

By use of an aerodynamic scheme we will get:

$$\alpha = A (cC_l) \quad (2.46)$$

Where A is the aerodynamic operator. In matrix form:

$$\{ \alpha \} = [A] \{ cC_l \} \quad (2.47)$$

or:

$$\{ cC_l \} = [A]^{-1} \{ \alpha \} \quad (2.48)$$

putting this into equation (2.45) we get:

$$\{ \theta \} = q [C] [\bar{W}] [A]^{-1} \{ \alpha \} \quad (2.49)$$

We note that $\alpha = \alpha_0 + \theta$

Where α_0 is the rigid or root angle of attack.

To calculate divergence, we set $\alpha_0 = 0$, so we get:

$$\{ \alpha \} = \{ \theta \} \quad (2.50)$$

and

$$\frac{1}{q} \{ \theta \} = [C] [\bar{W}] [A]^{-1} \{ \theta \} \quad (2.51)$$

This we recognize as a characteristic value equation where for the first characteristic value, say λ , we have:

$$\lambda = \frac{1}{q_{(\text{divergence})}} \quad (2.52)$$

This is the form of the solution to the divergence problem. We need only determine the three matrices $[C]$, $[\bar{W}]$ and $[A]$. Because the compliance matrix will be made to match the aerodynamic matrix we will determine the aerodynamic matrix first.

To derive the aerodynamic matrix I used the Weissinger L-Method. This method and its theoretical foundation are outlined in reference 7. The final matrix form for lift symmetric about the fuselage is:

$$\{ \alpha^S \} = [A^S] \{ cC_{\ell}^S \} \quad (2.53)$$

DeYoung and Harper in reference 11 write this equation in the form:

$$a_v = \sum_{n=1}^{(m-1)/2} a_{vn} G_n \quad (2.54)$$

The a_{vn} terms are the terms of the aerodynamic matrix and G_n is a form of the chord times the lift coefficient. They have graphed values

for the aerodynamic matrix terms versus wing geometry giving a 4 x 4 aerodynamic matrix. Although the swept wing was of primary interest in the divergence analysis, I constructed an aerodynamic matrix for both the straight wing and a 30 degree swept forward wing ($\Lambda = 0, -30$). With the aerodynamic matrix and known angle of attack, a simple simultaneous solution of the four equations gives the section coefficient of lift. The results are shown for constant angle of attack for both straight and sweep forward wings in figure 2.11. The lifting line results for the straight wing are coplotted for comparison.

The four stations used by Harper and DeYoung are the four so called Multhopp stations and are at:

$$\frac{x}{l} = .9239, .7071, .3827, 0.0$$

for the stations 1, 2, 3 and 4 respectively. This method puts the bound vortex at the quarter chord while meeting boundary conditions at the three quarter chord. This is equivalent to saying the force is at the quarter chord while the angle of attack is measured at the three quarter chord position. This gives us the necessary information to match the compliance matrix to the aerodynamic matrix.

Also reference 7 gives the terms in $[\bar{W}]$ when using the Multhopp stations.

To calculate the compliance matrix we will use the coordinate system in figure 2.12.

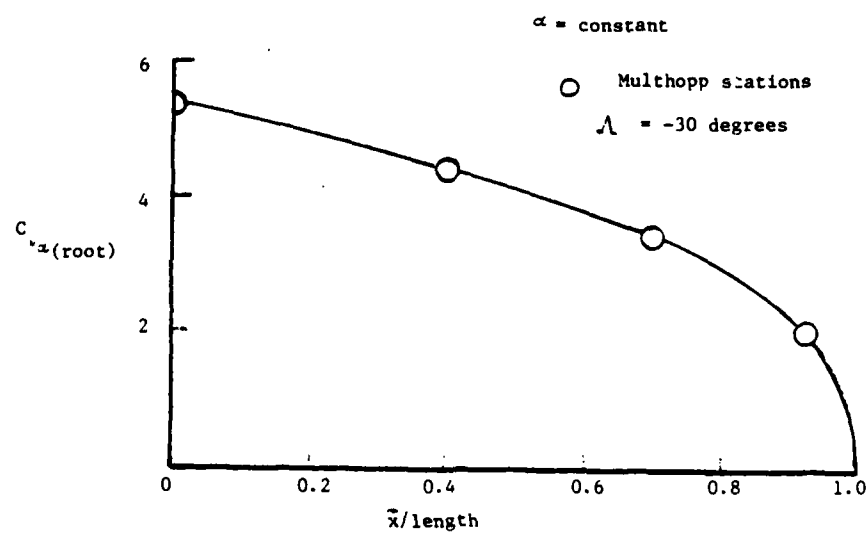
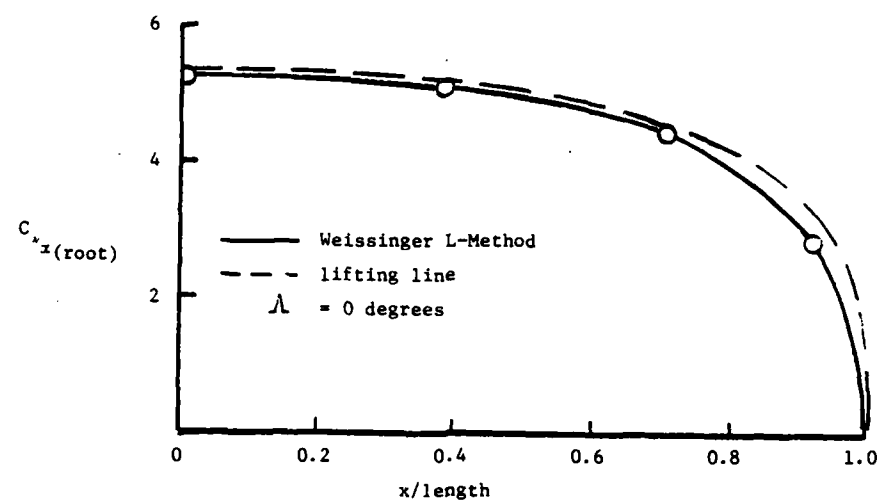


Figure 2.11 Lift distribution in the spanwise x direction using the Weissinger L-method

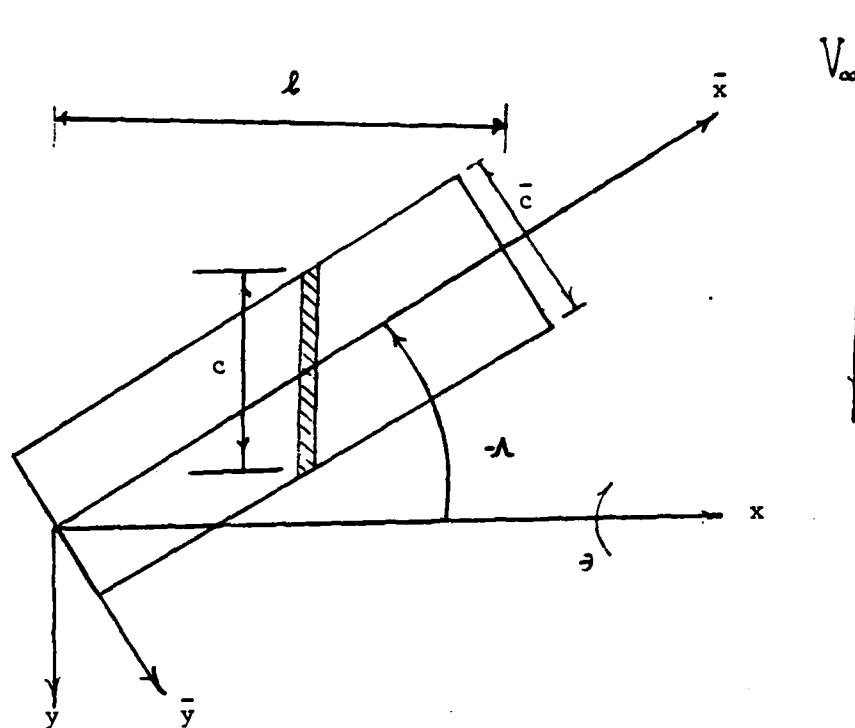


Figure 2.12 Swept forward wing coordinate system.

In our case all loads can be considered point loads applied at quarter chord in the \bar{y} -axis and at the Multhopp stations in the \bar{x} -axis. This reduces equation (2.24) to:

$$Q_r = \sum_{j=1}^4 F_j(\bar{x}_j, \bar{y}_j) \quad (2.55)$$

expanding this:

$$\begin{Bmatrix} Q_1 \\ Q_2 \\ \vdots \\ Q_5 \end{Bmatrix} = \begin{bmatrix} \gamma_1(\bar{x}_1, \bar{y}_1) & \gamma_1(\bar{x}_2, \bar{y}_2) & \dots & \gamma_1(\bar{x}_4, \bar{y}_4) \\ \gamma_2(\bar{x}_1, \bar{y}_1) & \gamma_2(\bar{x}_2, \bar{y}_2) & \dots & \gamma_2(\bar{x}_4, \bar{y}_4) \\ \vdots & \vdots & & \vdots \\ \gamma_5(\bar{x}_1, \bar{y}_1) & \gamma_5(\bar{x}_2, \bar{y}_2) & \dots & \gamma_5(\bar{x}_4, \bar{y}_4) \end{bmatrix} \begin{Bmatrix} F_1 \\ F_2 \\ \vdots \\ F_4 \end{Bmatrix}$$

Let's call the matrix that premultiplies $\{F\}$, $[R]$, so in short form:

$$\{Q\} = [R] \{F\} \quad (2.57)$$

Now putting that aside for the moment, let's get a relation for twist angle θ . Using small twist angle assumptions we can say:

$$\theta = - \frac{\partial w}{\partial y} \quad (2.58)$$

$$= - \frac{\partial w}{\partial \bar{y}} \cos \Lambda - \frac{\partial w}{\partial \bar{x}} \sin \Lambda \quad (2.59)$$

For w we substitute in equation (2.1)

$$\theta = - \sum_{i=1}^5 \left(\frac{\partial \gamma_i(\bar{x}, \bar{y})}{\partial \bar{y}} \cos \Lambda + \frac{\partial \gamma_i(\bar{x}, \bar{y})}{\partial \bar{x}} \sin \Lambda \right) q_i \quad (2.60)$$

To get the twist at the four Multhopp stations we use the \bar{x} -axis position of the station for \bar{x}_j and three quarter chord for \bar{y}_j where j is the index for the Multhopp station. This gives us:

$$\theta_j = - \sum_{i=1}^5 \left(\frac{\partial \gamma_i(\bar{x}_j, \bar{y}_j)}{\partial \bar{y}} \cos \Lambda + \frac{\partial \gamma_i(\bar{x}_j, \bar{y}_j)}{\partial \bar{x}} \sin \Lambda \right) q_i \quad (2.61)$$

in expanded form:

$$\begin{Bmatrix} \theta_1 \\ \theta_2 \\ \vdots \\ \theta_4 \end{Bmatrix} = \begin{bmatrix} \frac{\partial \gamma_1(\bar{x}_1, \bar{y}_1)}{\partial \bar{y}} & \frac{\partial \gamma_2(\bar{x}_1, \bar{y}_1)}{\partial \bar{y}} & \dots & \frac{\partial \gamma_5(\bar{x}_1, \bar{y}_1)}{\partial \bar{y}} \\ \frac{\partial \gamma_1(\bar{x}_2, \bar{y}_2)}{\partial \bar{y}} & \frac{\partial \gamma_2(\bar{x}_2, \bar{y}_2)}{\partial \bar{y}} & \dots & \frac{\partial \gamma_5(\bar{x}_2, \bar{y}_2)}{\partial \bar{y}} \\ \vdots & \vdots & \vdots & \vdots \\ \frac{\partial \gamma_1(\bar{x}_4, \bar{y}_4)}{\partial \bar{y}} & \frac{\partial \gamma_2(\bar{x}_4, \bar{y}_4)}{\partial \bar{y}} & \dots & \frac{\partial \gamma_5(\bar{x}_4, \bar{y}_4)}{\partial \bar{y}} \end{bmatrix} \cos \Lambda - \begin{bmatrix} \frac{\partial \gamma_1(\bar{x}_1, \bar{y}_1)}{\partial \bar{x}} & \frac{\partial \gamma_2(\bar{x}_1, \bar{y}_1)}{\partial \bar{x}} & \dots & \frac{\partial \gamma_5(\bar{x}_1, \bar{y}_1)}{\partial \bar{x}} \\ \frac{\partial \gamma_1(\bar{x}_2, \bar{y}_2)}{\partial \bar{x}} & \frac{\partial \gamma_2(\bar{x}_2, \bar{y}_2)}{\partial \bar{x}} & \dots & \frac{\partial \gamma_5(\bar{x}_2, \bar{y}_2)}{\partial \bar{x}} \\ \vdots & \vdots & \vdots & \vdots \\ \frac{\partial \gamma_1(\bar{x}_4, \bar{y}_4)}{\partial \bar{x}} & \frac{\partial \gamma_2(\bar{x}_4, \bar{y}_4)}{\partial \bar{x}} & \dots & \frac{\partial \gamma_5(\bar{x}_4, \bar{y}_4)}{\partial \bar{x}} \end{bmatrix} \sin \Lambda \begin{Bmatrix} q_1 \\ q_2 \\ \vdots \\ q_5 \end{Bmatrix}$$

Calling the matrix that premultiplies $\{q\}$ in equation (2.62), $[S]$, we have in short form:

$$\{\theta\} = [S] \{q\} \quad (2.63)$$

Now using equation (2.23) where we premultiply by the inverse of $[K]$.

$$\{ q \} = [K]^{-1} \{ Q \} \quad (2.64)$$

putting this in equation (2.63) we have:

$$\{ \theta \} = [S] [K]^{-1} \{ Q \} \quad (2.65)$$

putting equation (2.57) into equation (2.65)

$$\{ \theta \} = [S] [K]^{-1} [R] \{ F \} \quad (2.66)$$

We can now see that our compliance matrix is of the form:

$$[C] = [S] [K]^{-1} [R] \quad (2.67)$$

Finally, we put equation (2.67) in equation (2.51) giving us:

$$\frac{1}{q} \{ \theta \} = [S] [K]^{-1} [R] [\bar{W}] [A]^{-1} \{ \theta \} \quad (2.68)$$

This equation was solved in a digital computer and the first characteristic value gives the divergence velocity. With some of the wings with negative bending torsion coupling, for the straight wing case, the divergence velocity was imaginary. This indicates that according to linear theory the wing will not diverge. The results of the analysis are shown together with experimental data in table 4.1.

2.5 Flutter Analysis.

For flutter analysis, I used the well known V - g method. In this method, structural damping (g) is introduced into the equation of motion. since solutions of the equation of motion represent the neutral stability condition solution, when g is negative the wing is stable. When g is positive we see that damping is required for neutral stability. Flutter occurs when g is equal to the actual damping of the structure.

Assuming harmonic motion ($q(t) = q e^{i\omega t}$), the equation of motion is:

$$(\underline{K} \underline{q} - \omega^2 \underline{M} \underline{q}) e^{i\omega t} = \underline{Q} \quad (2.69)$$

First we need to derive the unsteady aerodynamic forces in terms of Q in equation (2.22). We will do this by deriving the variational work (δW) and put that in terms of Q by using equation (2.70).

$$\delta W = \sum_{n=1}^5 Q_r q_r \quad (2.70)$$

The general form for δW is:

$$\delta W = \int_0^1 \int_{-c/2}^{c/2} p \delta w dy dx \quad (2.71)$$

The term $p \delta w$ can be separated into three components and their respective displacements; lift, moment and camber force about the

midchord ($L\delta h$, $M\delta\theta$ and $N\delta\xi$).

where:

$$L = \int_{-c/2}^{c/2} p \, dy$$

$$M = - \int_{-c/2}^{c/2} yp \, dy$$

$$N = \int_{-c/2}^{c/2} \psi_5 p \, dy \quad (2.72)$$

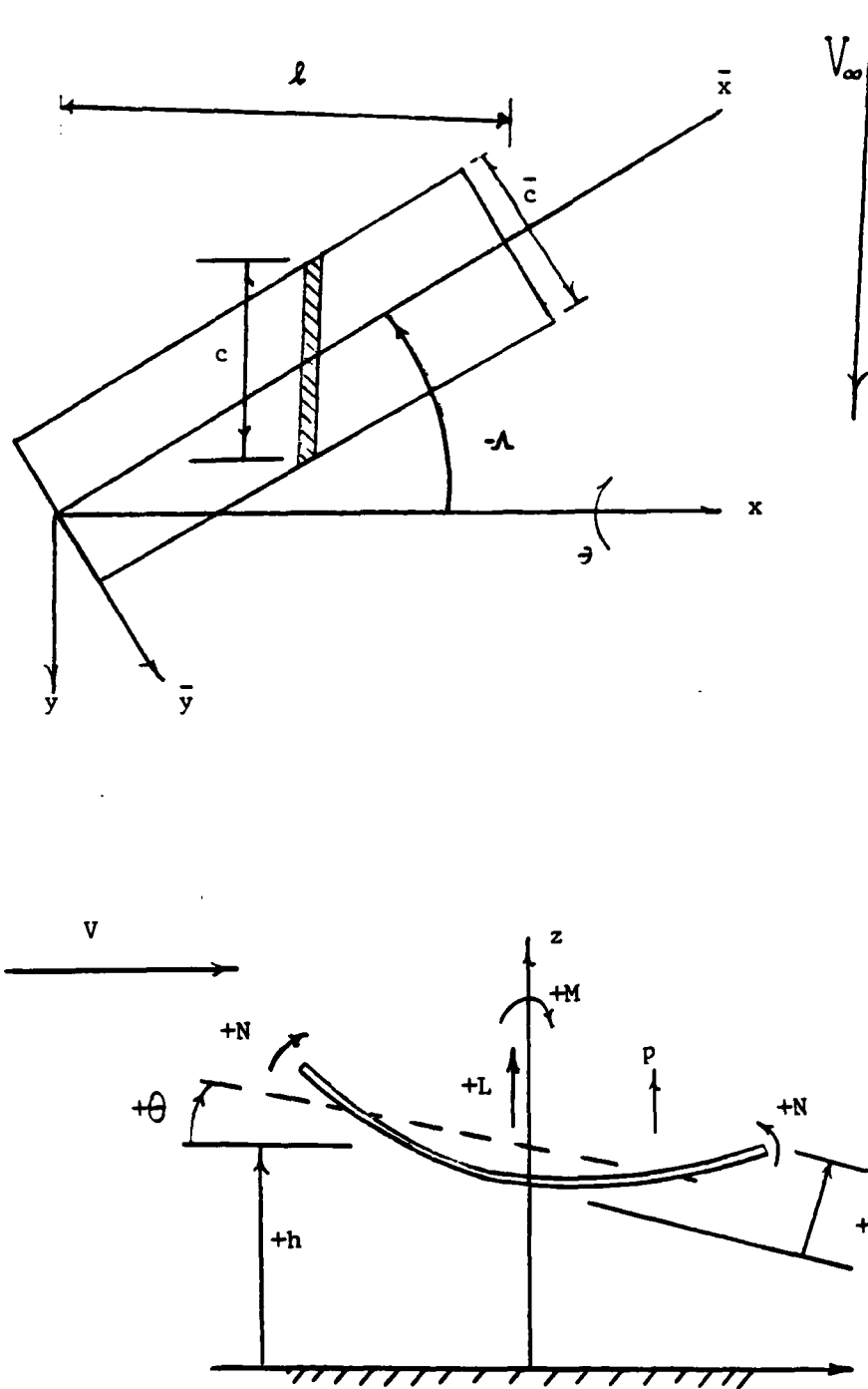


Figure 2.13 Swept wing coordinate system and the displacement sign convention.

Using figure 2.12 (reproduced here) for the swept wing geometry and figure 2.13 for the displacement sign convention, then relating the assumed modes to the different displacements we can write:

$$h = \phi_1(\bar{x}) q_1 + \phi_2(\bar{x}) q_2 \quad (2.73)$$

$$\theta = - \left\{ \frac{1}{c} \left[\phi_3(\bar{x}) q_3 + \phi_4(\bar{x}) q_4 \right] \cos\Lambda + \frac{dh}{d\bar{x}} \sin\Lambda \right\} \quad (2.74)$$

$$\xi = \phi_5(\bar{x}) q_5 \quad (2.75)$$

Using equation (2.73) we can write equation (2.74) as:

$$\begin{aligned} \theta = - \left\{ \frac{1}{c} \left[\phi_3(\bar{x}) q_3 + \phi_4(\bar{x}) q_4 \right] \cos\Lambda \right. \\ \left. + \left[\frac{d\phi_1}{d\bar{x}} q_1 + \frac{d\phi_2}{d\bar{x}} q_2 \right] \sin\Lambda \right\} \end{aligned} \quad (2.76)$$

Putting equation (2.72) in equation (2.71) we get:

$$\delta W = \int_0^l L \delta h \, dx + \int_0^l M \delta \theta \, dx + \int_0^l N \delta \xi \, dx \quad (2.77)$$

Now putting equation (2.73), (2.75), and (2.76) into equation (2.77) and rearranging terms we get:

$$\begin{aligned}
\delta W = & \left\{ \int_0^l L \phi_1(\bar{x}) dx - \sin\Lambda \int M \frac{d\phi_1(\bar{x})}{d\bar{x}} dx \right\} \delta q_1 \\
& + \left\{ \int_0^l L \phi_2(\bar{x}) dx - \sin\Lambda \int M \frac{d\phi_2(\bar{x})}{d\bar{x}} dx \right\} \delta q_2 \\
& - \frac{\cos\Lambda}{c} \int_0^l M \phi_3(\bar{x}) dx \delta q_3 \\
& - \frac{\cos\Lambda}{c} \int_0^l M \phi_4(\bar{x}) dx \delta q_4 \\
& + \int_0^l N \phi_5(\bar{x}) dx \delta q_5
\end{aligned} \tag{2.78}$$

Now, taking the relations worked out by Spielberg for 2-D incompressible aerodynamic theory in reference 12, and adapting them to our swept wing case, we get equations for lift, moment and camber force.

$$\begin{aligned}
L &= \pi \rho \omega^2 b^3 e^{i\omega t} \left(L_A \frac{h}{b} + L_B \theta + L_C \frac{\xi}{b} \right) \cos\Lambda \\
M &= \pi \rho \omega^2 b^4 e^{i\omega t} \left(M_A \frac{h}{b} + M_B \theta + M_C \frac{\xi}{b} \right) \cos\Lambda \\
N &= \pi \rho \omega^2 b^3 e^{i\omega t} \left(N_A \frac{h}{b} + N_B \theta + N_C \frac{\xi}{b} \right) \cos\Lambda
\end{aligned} \tag{2.79}$$

Where ρ is the air density, ω is the oscillating frequency, b is the

semichord and the functions L_A , L_B , L_C , M_A , etc are non-dimensional complex functions of reduced frequency $k = \omega b/V$, given by:

$$L_A = 1 - i \frac{2C(k)}{k}$$

$$L_B = \frac{i}{k} + i \frac{C(k)}{k} + \frac{2C(k)}{k^2}$$

$$L_C = -\frac{1}{12} - i \frac{C(k)}{3k} - \frac{2C(k)}{k^2}$$

$$M_A = -i \frac{C(k)}{k}$$

$$M_B = \frac{1}{8} - \frac{i}{2k} + i \frac{C(k)}{2k} + \frac{C(k)}{k^2}$$

$$M_C = \frac{i}{2k} - i \frac{C(k)}{6k} + \frac{1}{k^2} - \frac{C(k)}{k^2}$$

$$N_A = -\frac{1}{12} - i \frac{C(k)}{3k}$$

$$N_B = -\frac{i}{3k} + i \frac{C(k)}{6k} + \frac{C(k)}{3k^2}$$

$$N_C = \frac{1}{36} - i \frac{C(k)}{18k} + \frac{1}{2k^2} - \frac{C(k)}{3k^2} \quad (2.80)$$

where $C(k)$ is the Theodorsen function.

These equations assume harmonic motion such that:

$$h(x,y,t) = h(x,y) e^{i\omega t}, \text{ etc.} \quad (2.81)$$

Putting equations (2.79), (2.73), (2.76) and (2.75) in equation (2.78), using equation (2.70) and rearranging terms we get for Q_1 :

$$Q_1 = \pi \rho \omega^2 b^3 e^{i\omega t}.$$

$$\begin{aligned} & \left\{ \left[\cos \Lambda \frac{L_A}{b} \int_0^l \left(\phi_1(\bar{x}) \right)^2 dx - \cos \Lambda \sin \Lambda L_B \int_0^l \bar{\phi}_1(x) \frac{d\phi_1(\bar{x})}{d\bar{x}} dx \right. \right. \\ & - \cos \Lambda \sin \Lambda M_A \int_0^l \frac{d\phi_1(\bar{x})}{d\bar{x}} \phi_1(\bar{x}) dx + b \cos \Lambda \sin^2 \Lambda M_B \int_0^l \left(\frac{d\phi_1(\bar{x})}{d\bar{x}} \right)^2 dx \left. \right] q_1 \\ & + \left[\cos \Lambda \frac{L_A}{b} \int_0^l \phi_1(\bar{x}) \phi_2(\bar{x}) dx - \cos \Lambda \sin \Lambda L_B \int_0^l \phi_1(\bar{x}) \frac{d\phi_2(\bar{x})}{d\bar{x}} dx \right. \\ & - \cos \Lambda \sin \Lambda M_A \int_0^l \frac{d\phi_1(\bar{x})}{d\bar{x}} \phi_2(\bar{x}) dx \\ & \left. \left. + b \cos \Lambda \sin^2 \Lambda M_B \int_0^l \frac{d\phi_1(\bar{x})}{d\bar{x}} \frac{d\phi_2(\bar{x})}{d\bar{x}} dx \right] q_2 \right\} \end{aligned}$$

$$\begin{aligned}
& - \left[\frac{\cos^2 \Lambda}{c} L_B \int_0^{\ell} \phi_1(\bar{x}) \phi_3(\bar{x}) dx - \frac{b \cos^2 \Lambda \sin \Lambda}{c} M_B \int_0^{\ell} \frac{d\phi_1(\bar{x})}{dx} \phi_3(\bar{x}) dx \right] q_3 \\
& - \left[\frac{\cos^2 \Lambda}{c} L_B \int_0^{\ell} \phi_1(\bar{x}) \phi_4(\bar{x}) dx - \frac{b \cos^2 \Lambda \sin \Lambda}{c} M_B \int_0^{\ell} \frac{d\phi_1(\bar{x})}{dx} \phi_4(\bar{x}) dx \right] q_4 \\
& + \left[\cos \Lambda \frac{L_C}{b} \int_0^{\ell} \phi_1(\bar{x}) \phi_5(\bar{x}) dx - \cos \Lambda \sin \Lambda M_C \int_0^{\ell} \frac{d\phi_1(\bar{x})}{dx} \phi_5(\bar{x}) dx \right] q_5
\end{aligned}$$

$$Q_2 = \pi \rho \omega^2 b^3 e^{i\omega t}.$$

$$\begin{aligned}
& \left\{ \left[\cos \Lambda \frac{L_A}{b} \int_0^{\ell} \phi_2(\bar{x}) \phi_1(\bar{x}) dx - \cos \Lambda \sin \Lambda L_B \int_0^{\ell} \phi_2(\bar{x}) \frac{d\phi_1(\bar{x})}{dx} dx \right. \right. \\
& \quad \left. \left. - \cos \Lambda \sin \Lambda M_A \int_0^{\ell} \frac{d\phi_2(\bar{x})}{dx} \phi_1(\bar{x}) dx \right. \right. \\
& \quad \left. \left. + b \cos \Lambda \sin^2 \Lambda M_B \int_0^{\ell} \frac{d\phi_2(\bar{x})}{dx} \frac{d\phi_1(\bar{x})}{dx} dx \right] q_1 \right. \\
& \quad \left. + \left[\cos \Lambda \frac{L_A}{b} \int_0^{\ell} \phi_2(\bar{x})^2 dx - \cos \Lambda \sin \Lambda L_B \int_0^{\ell} \phi_2(\bar{x}) \frac{d\phi_2(\bar{x})}{dx} dx \right. \right. \\
& \quad \left. \left. - \cos \Lambda \sin \Lambda M_A \int_0^{\ell} \frac{d\phi_2(\bar{x})}{dx} \phi_2(\bar{x}) dx + b \cos \Lambda \sin^2 \Lambda M_B \int_0^{\ell} \left(\frac{d\phi_2(\bar{x})}{dx} \right)^2 dx \right] q_2 \right\}
\end{aligned}$$

$$- \left[\frac{\cos^2 \Lambda}{\bar{c}} L_B \int_0^{\ell} \phi_2(\bar{x}) \phi_3(\bar{x}) dx - \frac{b \cos^2 \Lambda \sin \Lambda}{\bar{c}} M_B \int_0^{\ell} \frac{d\phi_2(\bar{x})}{d\bar{x}} \phi_3(\bar{x}) dx \right] q_3$$

$$- \left[\frac{\cos^2 \Lambda}{\bar{c}} L_B \int_0^{\ell} \phi_2(\bar{x}) \phi_4(\bar{x}) dx - \frac{b \cos^2 \Lambda \sin \Lambda}{\bar{c}} M_B \int_0^{\ell} \frac{d\phi_2(\bar{x})}{d\bar{x}} \phi_4(\bar{x}) dx \right] q_4$$

$$+ \left[\frac{\cos \Lambda}{b} L_C \int_0^{\ell} \phi_2(\bar{x}) \phi_5(\bar{x}) dx - \cos \Lambda \sin \Lambda M_C \int_0^{\ell} \frac{d\phi_2(\bar{x})}{d\bar{x}} \phi_5(\bar{x}) dx \right] q_5$$

$$Q_3 = -\pi \rho \omega^2 b^3 e^{i\omega t}.$$

$$\left\{ \left[\frac{\cos^2 \Lambda}{\bar{c}} M_A \int_0^{\ell} \phi_3(\bar{x}) \phi_1(\bar{x}) dx - \frac{b \cos^2 \Lambda \sin \Lambda}{\bar{c}} M_B \int_0^{\ell} \phi_3(\bar{x}) \frac{d\phi_1(\bar{x})}{d\bar{x}} dx \right] q_1 \right.$$

$$+ \left[\frac{\cos^2 \Lambda}{\bar{c}} M_A \int_0^{\ell} \phi_3(\bar{x}) \phi_2(\bar{x}) dx - \frac{b \cos^2 \Lambda \sin \Lambda}{\bar{c}} M_B \int_0^{\ell} \phi_3(\bar{x}) \frac{d\phi_2(\bar{x})}{d\bar{x}} dx \right] q_2$$

$$- \left[\frac{b \cos^3 \Lambda}{\bar{c}^2} M_B \int_0^{\ell} \phi_3(\bar{x})^2 dx \right] q_3$$

$$- \left[\frac{b \cos^3 \Lambda}{\bar{c}^2} M_B \int_0^{\ell} \phi_3(\bar{x}) \phi_4(\bar{x}) dx \right] q_4$$

$$+ \left[\frac{\cos^2 \Lambda}{\bar{c}} M_C \int_0^l \phi_3(\bar{x}) \phi_5(\bar{x}) dx \right] q_5$$

$$Q_4 = -\pi \rho \omega^2 b^3 e^{i\omega t}.$$

$$\left\{ \left[\frac{\cos^2 \Lambda}{\bar{c}} M_A \int_0^l \phi_4(\bar{x}) \phi_1(\bar{x}) dx - \frac{b \cos^2 \Lambda \sin \Lambda}{\bar{c}} M_B \int_0^l \phi_4(\bar{x}) \frac{d\phi_1(\bar{x})}{d\bar{x}} dx \right] q_1 \right.$$

$$+ \left[\frac{\cos^2 \Lambda}{\bar{c}} M_A \int_0^l \phi_4(\bar{x}) \phi_2(\bar{x}) dx - \frac{b \cos^2 \Lambda \sin \Lambda}{\bar{c}} M_B \int_0^l \phi_4(\bar{x}) \frac{d\phi_2(\bar{x})}{d\bar{x}} dx \right] q_2$$

$$- \left[\frac{b \cos^3 \Lambda}{\bar{c}^2} M_B \int_0^l \phi_4(\bar{x}) \phi_3(\bar{x}) dx \right] q_3$$

$$- \left[\frac{b \cos^3 \Lambda}{\bar{c}^2} M_B \int_0^l \phi_4(\bar{x})^2 dx \right] q_4$$

$$+ \left[\frac{\cos^2 \Lambda}{\bar{c}} M_C \int_0^l \phi_4(\bar{x}) \phi_5(\bar{x}) dx \right] q_5$$

$$Q_5 = \pi \rho \omega^2 b^3 e^{i\omega t}.$$

$$\left\{ \left[\frac{\cos \Lambda}{b} N_A \int_0^l \phi_5(\bar{x}) \phi_1(\bar{x}) dx - \cos \Lambda \sin \Lambda N_B \int_0^l \phi_5(\bar{x}) \frac{d\phi_1(\bar{x})}{d\bar{x}} dx \right] q_1 \right.$$

$$\begin{aligned}
& + \left[\frac{\cos \Lambda}{b} N_A \int_0^{\ell} \phi_5(\bar{x}) \phi_2(\bar{x}) dx - \cos \Lambda \sin \Lambda N_B \int_0^{\ell} \phi_5(\bar{x}) \frac{d\phi_2(\bar{x})}{d\bar{x}} dx \right] q_2 \\
& - \left[\frac{\cos^2 \Lambda}{c} N_B \int_0^{\ell} \phi_5(\bar{x}) \phi_3(\bar{x}) dx \right] q_3 \\
& - \left[\frac{\cos^2 \Lambda}{c} N_B \int_0^{\ell} \phi_5(\bar{x}) \phi_4(\bar{x}) dx \right] q_4 \\
& + \left[\frac{\cos \Lambda}{b} N_C \int_0^{\ell} \phi_5(\bar{x})^2 dx \right] q_5
\end{aligned} \tag{2.82}$$

In order to integrate with respect to the variable x we use the substitution;

$$x = \bar{x} \cos \Lambda \tag{2.83}$$

This makes the limits of integration: 0 to $\ell/\cos \Lambda$ or 0 to ℓ , which is the original distance in the unswept case. Now we write Q in the form:

$$Q_1 = \pi \rho \omega^2 b^3 e^{i\omega t} \sum_{j=1}^5 A_{1j} q_j \tag{2.84}$$

where the terms of $[A]$ are:

$$A_{11} = \frac{\cos^2 \Lambda}{b} L_A \ell I_1 - \cos^2 \Lambda \sin \Lambda L_B I_{24} - \cos^2 \Lambda \sin \Lambda M_A I_{24} \\ + b \cos^2 \Lambda \sin^2 \Lambda M_B \frac{1}{\ell} I_{25}$$

$$A_{12} = -\cos^2 \Lambda \sin \Lambda L_B I_{26} - \cos^2 \Lambda \sin \Lambda M_A I_{27} + \frac{b \cos^2 \Lambda \sin^2 \Lambda}{\ell} M_B I_{28}$$

$$A_{13} = -\frac{\cos^3 \Lambda}{c} L_B \ell I_{29} + \frac{b \cos^3 \Lambda \sin \Lambda}{c} M_B I_{30}$$

$$A_{14} = -\frac{\cos^3 \Lambda}{c} L_B \ell I_{31} + \frac{b \cos^3 \Lambda \sin \Lambda}{c} M_B I_{32}$$

$$A_{15} = \frac{\cos^2 \Lambda}{b} L_C \ell I_{33} - \cos^2 \Lambda \sin \Lambda M_C I_{34}$$

$$A_{21} = -\cos^2 \Lambda \sin \Lambda L_B I_{27} - \cos^2 \Lambda \sin \Lambda M_A I_{26} + \frac{b \cos^2 \Lambda \sin^2 \Lambda}{\ell} M_B I_{28}$$

$$A_{22} = \frac{\cos^2 \Lambda}{b} L_A \ell I_2 - \cos^2 \Lambda \sin \Lambda L_B I_{35} - \cos^2 \Lambda \sin \Lambda M_A I_{35} \\ + b \cos^2 \Lambda \sin^2 \Lambda M_B \frac{1}{\ell} I_{36}$$

$$A_{23} = -\frac{\cos^3 \Lambda}{c} L_B \ell I_{37} + \frac{b \cos^3 \Lambda \sin \Lambda}{c} M_B I_{38}$$

$$A_{24} = -\frac{\cos^3 \Lambda}{c} L_B \ell I_{39} + \frac{b \cos^3 \Lambda \sin \Lambda}{c} M_B I_{40}$$

$$A_{25} = \frac{\cos^2 \Lambda}{b} L_C \ell I_{41} - \cos^2 \Lambda \sin \Lambda M_C I_{42}$$

$$A_{31} = -\frac{\cos^3 \Lambda}{c} M_A \ell I_{29} + \frac{b \cos^3 \Lambda \sin \Lambda}{c} M_B I_{30}$$

$$A_{32} = -\frac{\cos^3 \Lambda}{c} M_A \ell I_{37} + \frac{b \cos^3 \Lambda \sin \Lambda}{c} M_B I_{38}$$

$$A_{33} = \frac{b \cos^4 \Lambda}{c^2} M_B \ell I_3$$

$$A_{34} = 0$$

$$A_{35} = -\frac{\cos^3 \Lambda}{c} M_C \ell I_{43}$$

$$A_{41} = -\frac{\cos^3 \Lambda}{c} M_A \ell I_{31} + \frac{b \cos^3 \Lambda \sin \Lambda}{c} M_B I_{32}$$

$$A_{42} = -\frac{\cos^3 \Lambda}{c} M_A \ell I_{39} + \frac{b \cos^3 \Lambda \sin \Lambda}{c} M_B I_{40}$$

$$A_{43} = 0$$

$$A_{44} = \frac{b \cos^4 \Lambda}{c^2} M_B \ell I_4$$

$$A_{45} = -\frac{\cos^3 \Lambda}{c} M_C \ell I_{44}$$

$$A_{51} = \frac{\cos^2 \Lambda}{b} N_A \ell I_{33} - \cos^2 \Lambda \sin \Lambda N_B I_{34}$$

$$A_{52} = \frac{\cos^2 \Lambda}{b} N_A \ell I_{41} - \cos^2 \Lambda \sin \Lambda N_B I_{42}$$

$$A_{53} = - \frac{\cos^3 \Lambda}{c} N_B \ell I_{43}$$

$$A_{54} = - \frac{\cos^3 \Lambda}{c} N_B \ell I_{44}$$

$$A_{55} = \frac{\cos^2 \Lambda}{b} N_C \ell I_5 \quad (2.85)$$

The integrals and their values are listed in table A.1.

From this point on, the flutter analysis for the swept wing is the same as the analysis for the straight wing as give by Hollowell and Dugundji in reference 5.

Equation (2.84) is put in equation (2.69) and both sides are divided by $e^{i\omega t}$.

$$\underline{K} \underline{q} - \omega^2 \underline{M} \underline{q} = \pi \rho \omega^2 b^3 \underline{A} \underline{q} \quad (2.86)$$

In the normal fashion for the V - g flutter analysis, structural damping (g) is introduced by multiplying K by (1 + ig). We define a complex eigenvalue Z as:

$$Z = \frac{1 + ig}{\omega^2} \quad (2.87)$$

we define a new matrix \underline{B} as:

$$\underline{B} = \underline{M} + \pi \rho b^3 \underline{A} \quad (2.88)$$

Finally putting equations (2.87) and (2.88) in equation (2.86) we have, a standard form, complex eigenvalue problem:

$$\{ \underline{B} - Z \underline{K} \} \underline{q} = 0 \quad (2.89)$$

This equation was solved on a digital computer. Selected values of reduced frequency k were used to calculate the aerodynamic matrix. The eigenvalues Z were used to get the oscillating frequency ω , the structural damping required g , and the velocity V , according to equations (2.90).

$$\omega = \frac{1}{\sqrt{\text{Re}(Z)}} \quad g = \frac{\text{Im}(Z)}{\text{Re}(Z)} \quad V = \frac{b\omega}{k} \quad (2.90)$$

The flutter velocity was chosen as the velocity at which the structural damping required to maintain neutral stability became zero on any of the five modes. The associated value of ω is the flutter frequency. To simplify calculation of the Theodorsen function $C(k)$, I used the R. T. Jones approximation given in equation (2.91).

$$C(p) = \frac{0.5 p^2 + 0.2808 p + 0.01365}{p^2 + 0.3455 p + 0.01365} \quad \{ p = ik \} \quad (2.91)$$

Note that by using large values of k the output frequency will be the natural vibration frequency of the wing in an atmosphere of density ρ . This technique was used to get the theoretical natural frequencies.

This analysis was done for all thirteen wings. The results are plotted in figure D.9 through D.34.

CHAPTER 3. EXPERIMENTS

3.1 Test Wing Selection

The criteria defining desirable characteristics of the test wings are the same criteria used by Hollowell in reference 2. they are:

- a) The wings should have a wide range of bending-torsion stiffness coupling.
- b) The wings should have constant chord, thickness, sweep and zero camber.
- c) The wings should flutter or diverge within the 0-30 m/s speed range of the available wind tunnel.
- d) The wings should be small enough to be made with the available equipment for manufacturing graphite/epoxy plates at M.I.T..
- e) The wings should not sustain any damage under repeated large static and dynamic deflections.

To give a good cross section of the range of bending-torsion coupling and stiffness, both balanced and unbalanced laminates were made at three different ply angles. In table 3.1 we can see the range covered.

[0 ₂ /90] _s			
[+15 ₂ /0] _s	[±15/0] _s	[∓15/0] _s	[-15 ₂ /0] _s
[+30 ₂ /0] _s	[±30/0] _s	[∓30/0] _s	[-30 ₂ /0] _s
[+45 ₂ /0] _s	[±45/0] _s	[∓45/0] _s	[-45 ₂ /0] _s

← increased negative	0	increased positive →
bending-torsion coupling		bending-torsion coupling

Table 3.1 Different laminate layups used for the test wings.

The $[0_2/90]_s$ serves as the only uncoupled example. Positive bending-torsion coupling means when the wing is bent in the positive z direction the wing will twist in the positive twist direction. The positive twist direction is the same direction as positive angle of attack. Because of the layup convention shown in figure 2.1, $+ \theta$ fibers on the outside plies result in negative bending-torsion stiffness coupling and vice versa.

3.2 Static Deflection Tests

The goal for the static deflection tests was to test the wings under static loads of pure force and pure moment. Also the loads should be large enough to cause large deformations, in order to identify any non-linearities in the stress-strain relations and thus identify the limitations of our linear analysis.

The static deflection setup is shown in fig 3.1. It is

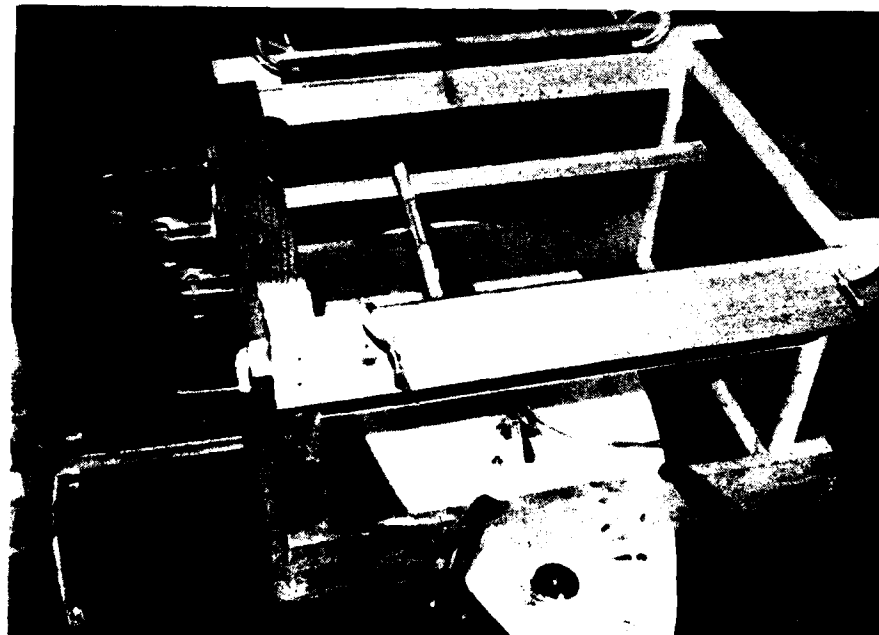


Figure 3.1 Static deflection test apparatus.

constructed of sturdy wood beams with metal rulers attached to the insides of the top horizontal beams. These rulers were used to measure horizontal deflection while a carpenters square was used to measure vertical deflection. To minimize measuring error we extended pins from a balsa wood clamp at the wing tip. threads ran from two eyelets on the balsa wood clamp around pulleys clamped to the side of the test apparatus

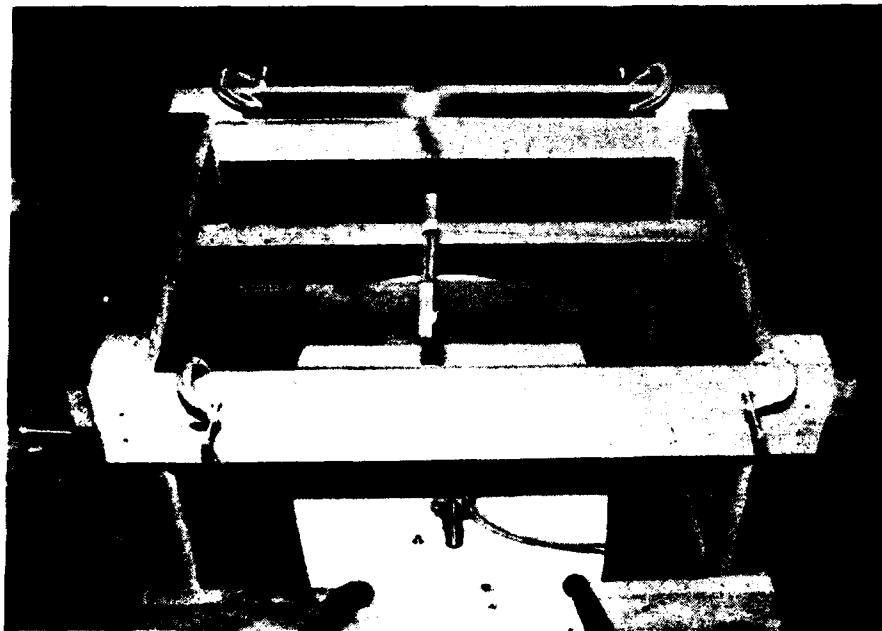


Figure 3.2 Static test stand with a moment being applied.

and down to weight holders. One eyelet was at the wing leading edge while the other was at the trailing edge. To apply a force the pulleys and weights were put on the same side of the test apparatus while to apply a moment the pulleys and weights for the leading edge were put on one side and those for the trailing edge were put on the other side. (see figure 3.2)

We applied force in increments of approximately 0.2 N up to 1.0 N then in double increments till a bending deflection of approximately 12 cm. Moment was applied in a similar manner with initial increments of .0075 NM till approximately 0.2 NM. This caused a twist of from 8 to 22 degrees depending upon the torsional stiffness of the wing.

3.3 Wind Tunnel Test Setup.

We did the wind tunnel tests in the M.I.T. acoustic wind tunnel. This tunnel has continuous flow with a 1.5 by 2.3 meter free-jet test

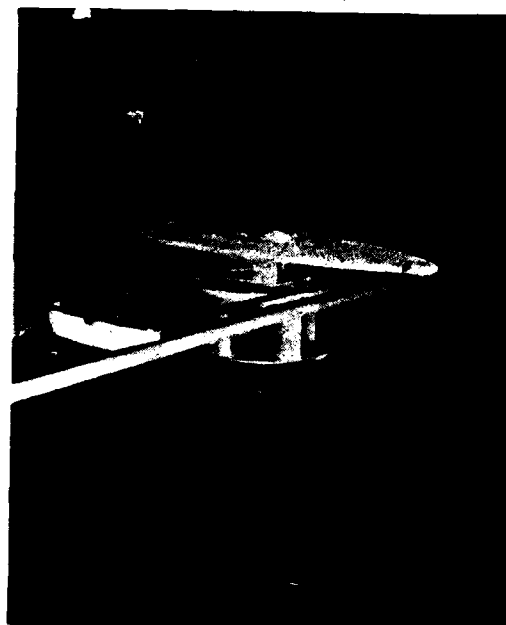


Figure 3.2 M.I.T. wind tunnel test setup.

section 2.3 meter long, located inside a large anechoic chamber. The tunnel speed range is continuously variable up to approximately 30 m/s. Velocity was sensed by a pitot tube in the throat immediately before the test section and registered on a electrical baratron.

The test setup is shown in figure 3.2. The wing mount consists of

a turntable machined from alluminum and mounted on a rigid pedestal. The mount for the wing is attached to the top of the turntable. The turntable allows rotation of the wing to angles of attack from -4 to 20 degrees while the top of the wing mount allows wing sweep in increments of 15 degrees from -45 to $+45$ degrees of sweep. The photo shows the wing in -30 degrees of sweep. In our testing only the -30 and 0 degrees of sweep positions were used. Slightly below the base of the wing we



Figure 3.4 Looking down on a test wing by using a mirror.

mounted a flat disk to provide smooth airflow past the model, a good background for the vertical photos, a place to mount the angle of attack control rod and also a place to mount a terminal for the strain gauge wires. The disk was also labeled for each test to identify the still and video pictures. A typical photo taken during a test is shown in

figure 3.4. We hung a mirror over the wing to get the pictures looking down on the wing. Figure 3.5 shows the location of the video camera, still camera, strobe and floodlight. When it was necessary to "slow down" the motion during a flutter test we used a strobe, otherwise floodlights were used. By checking the strobe frequency we could determine the wing flutter frequency.

The scale on the disk was used to measure wing tip bending and twisting. It is graduated in 1 cm increments. Since viewing angle and position affect the picture you see when looking at the test wing through the mirror, tests and calculations were made to adjust the apparent displacement to the actual displacement. These adjustments were then applied to the data readings off the pictures.

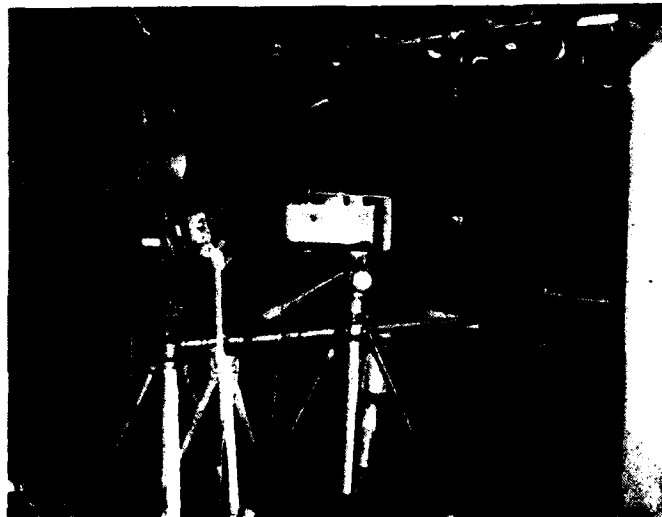


Fig.3.5 Equipment used to illuminate and record test wing movement.

3.4 Natural Frequency Tests.

Hollowell, Jensen, and Selby (references 2,3 and 4), already tested many of these wings for their natural frequencies. Also they have shown that the theoretical analysis using the five Rayleigh-Ritz modes gives accurate results for the first and second bending and first torsional natural frequencies. Therefore instead of doing extensive natural frequency tests we did a simple initial deflection vibration test. With the wing mounted for the wind tunnel test we gave it an initial deflection in twist and bending, released the wing and recorded the oscillations on the strip chart recorder. The resulting oscillations contained strong first bending with weak second bending and first torsion oscillations.

3.5 Steady Airload Test.

The steady airload tests were to be run at zero sweep and wind speeds of 5, 10 and 15 m/s. However after investigating the results and repeating selected tests we determined that the baratron on the original tests was indicating a lower airspeed than the actual tunnel airspeed. Using a different and accurately calibrated baratron during the repeat tests we determined that the actual tunnel airspeeds on the original tests were 5, 11.5 and 16 m/s within a tolerance of 0.5 m/s.

To run the test, first we set the tunnel speed, then using the strain gauge readings we zeroed the angle of attack by setting it so that the average bending and torsion gauge readings were zero. (The tunnel, especially at higher speeds has enough turbulence to cause small irregular deflections in the wing causing temporary non zero readings even at zero degrees angle of attack.) The wing was then run through angles of attack from 0 to 20 degrees at two degree increments. We made records of each incremental stop by strip chart records of the strain gauge readings, still photos and video recordings. Following the completion of tests at one airspeed we repeated the procedure at the next higher airspeed. Once a wing showed moderate flutter, angle of attack

was not increased at that speed. Some of the wings will flutter at 16 m/s at any angle of attack so that portion of the test for those wings was omitted.

3.6 Flutter Boundary Tests.

A flutter boundary is a curve plotted on a airspeed vs. angle of attack graph for a particular wing where one side of the graph, invariably the lower airspeed side, is a flutter free area while the other is a flutter area. Previous experimenters had found the flutter boundaries of many of the wings in our tests. Our goal was to complete these tests for all the wings at both no sweep and 30 degrees forward sweep. Our procedure was to set the airspeed, zero the angle of attack and then run through the different angles of attack checking for flutter. When we encountered any flutter, either bending or torsion, we made strip chart recordings and checked the frequency with the strobe. After finishing tests at that airspeed the angle of attack was reduced, the airspeed was increased by 1 m/s and the test procedure was repeated. When airspeed is increased to the point where the wing flutters at all angles of attack or the maximum tunnel speed is reached final readings are taken and the test for that wing is complete.

3.7 Flutter Test.

Our goal was to observe the actual shapes of the wing during both low and high angle of attack flutter. In particular we wanted to concentrate on observing the wing tip, getting not only qualitative data but actual measurements of the bending and twisting seen at the tip. We chose 1 degrees AOA for the low angle of attack flutter and 10 degrees AOA for the high angle of attack flutter. Using data from the previously run flutter boundary tests, we set the airspeed at the flutter speed and then set the angle of attack. If the flutter was intermittent or of very small amplitude we increased the airspeed by as much as one meter per second in order to get a flutter motion visible on the video pictures. Of

all the flutter cases with the various wings, the wings fell into two main categories; ones that had flutter dominated by torsion oscillations and ones that had flutter dominated by bending oscillations. The torsion flutter frequencies were in the area of 30 to 60 hz. This is much too fast to see clearly with the eye and even using a video camera the motion will come out blurred on each frame. However since the motion is steady in a periodic sense it can be captured by use of a strobe. The strobe flash frequency is set near the flutter frequency by visual observation, resulting in flutter motion that can be viewed at apparent slow motion. The images also record relatively well on a video camera. The strobe has a very fast flash during which the wing moves very little, giving a sharp but brief image. The video camera elements, however, have a certain amount of persistency, holding the image after the flash has stopped. So when the video camera scans it has an image nearly all the time even though the flash lasts less than 1/1000th of a second. For this reason the video pictures made using the strobe provided all the quantitative data on the high frequency flutter. When the flutter frequency was low, as in bending flutter, we took video pictures using alternately strobe and floodlight. Under floodlighting the video picture was clear but still too fast to take measurements. While recording under the strobe the video recording was blank with an occasional brief picture. However, when individual frames were viewed in still motion, the floodlight video pictures were easy to interpret. The strobe lighted video pictures were another matter. When the strobe had flashed a single video frame was clear, otherwise it was blank. With the strobe flashing at about 5 hz and the video camera scanning at 30 hz there is one clear frame followed by approximately 6 blank frames. This large spacing between good video frames along with the slow flash rate in relation to random turbulence induced motion in the tunnel made it difficult to know when we had a picture of the wing at maximum deflection. Therefore the floodlight video pictures provided the bulk of the data for the bending flutter cases.

In all cases, we took video pictures from the side and looking down of the wing under both strobe and floodlight. By properly positioning the mirror we could change from the side view of the wing to the top view by merely changing the camera viewing angle. The side views are used for qualitative evaluation of the flutter motion. The side view can identify nodes in the vibration shapes and is especially helpful to identify the presence of any second mode bending. The top view clearly showed the motion of the wingtip relative to the root. Using the scale on the background we were able to measure the deflection in both bending and torsion of both extremes of the flutter motion. With the strobe frequency set at approximately twice the flutter frequency the two extremes of the flutter motion could be captured on the same picture. Similarly by using a double exposure on the still camera the two extremes are caught on the same picture. This is shown in figure 3.6.



Figure 3.6 Double exposure showing extremes of flutter motion.

CHAPTER 4. RESULTS

4.1 Static Deflection

Perhaps the best way to examine the results of the static deflection Rayleigh-Ritz analysis and experiment is by looking at two typical examples. Picking the $[0_2/90]_s$ and the $[+15_2/0]_s$ layup wings results as shown in figures B.1 and B.2, we can compare the deflections produced under similar loading. The most striking thing we see is the effect of bending-torsion coupling. While the $[0_2/90]_s$ layup wing only bends under a force and only twists under a moment load, the $[+15_2/0]_s$ layup wing both bends and twists under either a force load or a moment load. It is this property that gives the wings their interesting aeroelastic properties.

Some of the noteworthy properties of all the wings are:

- 1) Bending-torsion coupling increases with increased absolute value of the fiber angle of the outer plies for both the balanced and unbalanced layups (balanced means that for every $+\theta$ ply in the wing there is a $-\theta$ ply).

- 2) The bending-torsion coupling for a $[+\theta/0]_s$ layup is opposite in sign from a $[-\theta/0]_s$ layup, but equal in magnitude.

- 3) Bending stiffness decreases as ply fiber angle is increased.

- 4) Torsion stiffness increases with increases in ply fiber angle up to 30 degrees. The 45 degree ply fiber angle layup reverses the trend and has a slightly lower torsional stiffness than the 30 degree ply fiber angle layup.

With a few exceptions all wings deformed in close agreement with linear theory in the so called small deflection range. For these wings the linear range was bending up to 5 centimeters and twist up to 6 degrees. At larger deflections the wings show a general tendency to become stiffer than linear theory predicts. This was an expected result due to the increasing influence of non-linear factors in the wing and in the test procedure. For example, loads were always applied perpendicular

to the wing undeflected position (force in the z direction and moments about the x axis). But with large deflections the loads were no longer at right angles to the wings new position. Therefore the amount of effective load was somewhat less than the actual applied load.

The coupling deflections, that is, the twist due to applied force and the bending due to applied moment, held close to linear theory on the wings that had a large amount of coupling. The exceptions were the coupling deflections of bending due to moment for some of the lightly coupled wings. In particular, the two balanced layup wings with the lowest bending-torsion coupling, the $[\pm 15/0]_s$ and $[\pm 30/0]_s$ layup wings. Both of these wings had large deviations from linear theory with bending due to moment in one direction. Moments of opposite sign produced expected bending results in the other direction. In particular, examining the $[\pm 15/0]_s$ layup wing test results, shown in figure 4.1, we

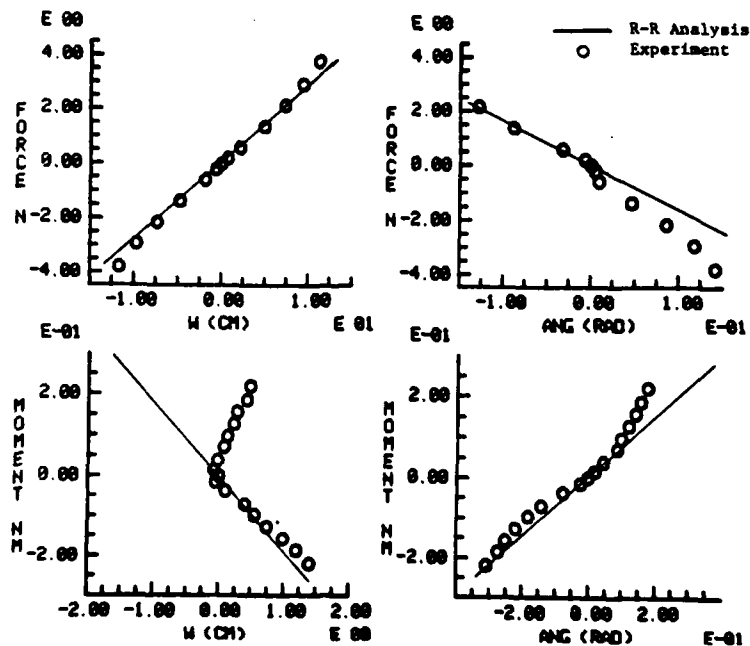


figure 4.1 static deflection test results for $[\pm 15/0]_s$ layup wing.

see that when a positive moment was applied the wing bent slightly in the direction opposite of the one predicted by theory. Yet, for a negative moment the wing bent as predicted. Upon close examination of the wing we found that in its unloaded state it had a slight chordwise camber, negative looking down the wing from the wingtip, as shown in figure 4.2. According to plate theory, a certain minimum load must be applied in the

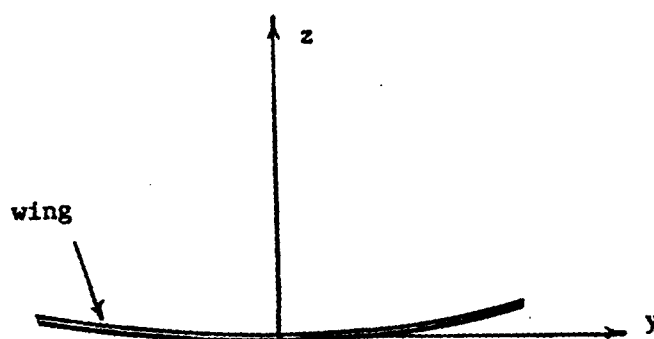


Figure 4.2 Initial camber (exaggerated) in the $[\pm 15/0]_s$ layup wing.

negative direction to buckle the plate in order to get any deflection in the negative direction. Since the coupling force is weak (at 0.2 Nm of moment the expected bending is equivalent to that produced by a force of only 0.3N) it apparently is unable to "pop out" the camber in the wing and therefore the wing does not deflect in the positive direction. The $[\pm 30/0]_s$ wing had a similar problem although somewhat less severe.

The initial camber in the wings was probably caused by not orienting the plies exactly at the proper angle during layup, causing them to be cured slightly out of alignment. This is not an easy problem to avoid, and very small deviations will produce significant warping. Nearly all wings had some inadvertent warp but the large coupling present

in most wings could develop enough force to overcome the problem. It was only in the lightly coupled wings that initial camber caused significant deviation from linear theory.

One point to note is that if we bent the wing enough to pop out the camber and then applied the moment, coupling behavior was normal. When airloads are applied in the wind tunnel the lift is strong enough to pop out the camber so the wing could still be expected to act according to the linear analysis.

4.2 Steady Airload Deflection

Qualitatively, both the analysis and the test results were what one would logically expect. The wings with negative bending-torsion coupling (positive bending produces negative twist) deflected much less than their counterparts with positive bending-torsion coupling. This indicates that the negative coupled wing did reduce and redistribute the airload by decreasing the angle of attack of the wing sections. The video pictures confirmed the decreased angle of attack of the wing tip. However, if we compare the $[+15_2/0]_s$ layup wing with the $[+30_2/0]_s$ layup wing, we see that the wing with the more negative bending-torsion coupling deflects more than the one with the less negative coupling. The reason is that as we increase the ply fiber angle we not only increase bending-torsion coupling but we also decrease the bending stiffness. Therefore, although the $[+30_2/0]_s$ layup wing may twist more and therefore lower the airload more than the $[+15_2/0]_s$ layup wing the difference in bending stiffness offsets the difference in coupling.

We can see the interplay between bending stiffness and bending-torsion coupling if we examine the steady airload deflection at one airspeed and no sweep ($\Lambda = 0$) for the four wing layups that use a particular degree ply fiber angle. Figure 4.3 shows the theoretical calculations results for the four 15 degree fiber angle layup wings at 11.5 meters per second airspeed. The twist angles follow directly the amount of bending-torsion coupling. The bending deflection (w) however, depends on the combined effects of bending stiffness and bending-torsion

coupling. The $[\pm 15/0]_s$ layup wing bends the least because of its

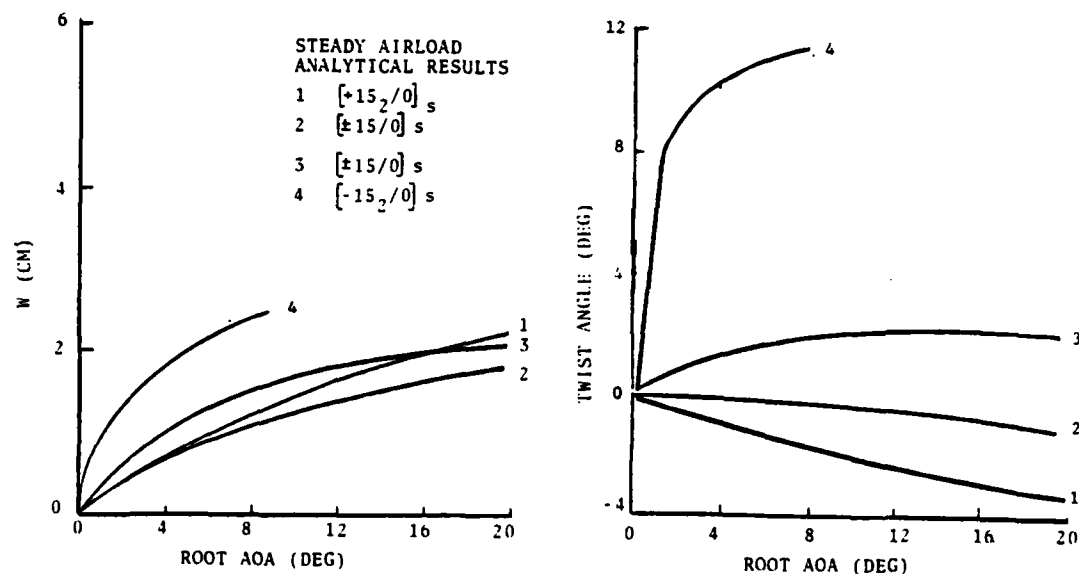


Figure 4.3 Steady airload analysis on the four wings with a 15 degree ply fiber angle at 11.5 m/s and $\Lambda = 0$.

higher bending stiffness and slight negative twist. The $[+15_2/0]_s$ bends just slightly more. Apparently its negative coupling could not completely compensate for the decreased bending stiffness. The following two wings follow in order of bending-torsion coupling at low angles of attack. Then at higher angles of attack the $[\mp 15/0]_s$ layup wing bends a little less than the $[+15_2/0]_s$ layup wing. At a root angle of attack of 20 degrees the slightly higher angle of attack of the $[\mp 15/0]_s$ layup wing results in only a very minor increase in the coefficient of force. Therefore, the higher wing stiffness dominates. In general we can say that when at a fixed root angle of attack negative bending-torsion coupling will cause a wing to both lessen the total airload and also redistribute the airload toward the root, while positive bending-torsion coupling will cause a wing to increase the total load and redistribute it toward the wing tip.

. One point worth noting concerning the $[\pm 15/0]_s$ layup wing is the

fact that under airload it had very little twist. In this case the coupling force was approximately just strong enough to cancel the twisting force generated by the airload. In twisting this particular wing acted much like a rigid wing. It is easy to imagine a case where this could be an advantage in a wing design.

At the higher airspeeds used in the test the highly positive coupled wings showed a tendency even at low root angles of attack to continue twisting until the wing sections near the tip reached angles that produce a coefficient of force near the maximum coefficient of force. For example, the $[-45_2/0]_s$ layup wing at 11.5 m/s at 4 degrees root angle of attack had twisted an additional 6 degrees and reached a deflection of 6 cm. This put the tip at 84 percent of maximum coefficient of force. In a practical sense we can say the wing has diverged. Unlike classical divergence there are limits to the twist because we have used a realistic coefficient of force that has a maximum value.

Comparing the analytical and experimental data quantitatively (see figures C.1 through C.13) the agreement is satisfactory considering attainable accuracy in measurement except for a few areas. In particular at higher angle of attack the $[0_2/90]_s$ layup wing at 11.5 and 16 m/s and the $[\pm 15/0]_s$ layup wing at 16 m/s had experimental values much higher than those predicted by the analysis. The high experimental readings were coincidental with the appearance of torsional flutter of the wings. In other words once the wing started to flutter in torsion it also bent more than predicted by the analysis. This is a preliminary indication that when in torsional flutter, the wings have a higher average coefficient of force at a certain airspeed and angle of attack than they would without the flutter. This means that either the lift or drag or both increase or are redistributed toward the tip when the wing flutters. Clearly the wings are taking more energy out of the air in order to sustain the vibrations. Also it seems logical that the vibrations cause some additional disturbance to the airstream thus increasing the drag. These reasons for the increased deflection are

speculation, however, the one conclusion we can draw is: Once a wing starts to flutter it does not vibrate about the steady state position it would have were it not fluttering. Therefore we also conclude that any steady airload analysis that does not include the average of forces generated by the unsteady airloads in flutter will underestimate the average airload and therefore underpredict the average deflection.

4.3 Divergence Velocities

The divergence investigation can be considered the limit of the steady airload investigation. We are looking for the static stability limit, the point where the linear feedback system mentioned in chapter two no longer converges.

The investigation pointed out the extreme differences between the wings due solely to different ply fiber angle layup patterns. By examining table 4.1 we see that for a straight wing divergence ranges from a low of 12.4 m/s to a high of infinity. For a straight wing ($\Lambda=0$) the rule is simple: With a sufficient amount of negative bending-torsion coupling the wing will not diverge. The actual value of the critical amount is somewhere below that of the $[\pm 15/0]_s$ layup wing, our most lightly coupled wing. On the other hand, positive bending-torsion coupling lowers the divergence speed in relation to its magnitude.

For the 30 degree swept forward wing ($\Lambda=-30$) the investigation showed there is an optimum fiber angle layup pattern for increasing divergence speed. Because bending causes increases in angle of attack due to geometry, all the wings have a finite divergence speed. However, by using the optimum layup pattern the divergence speed can be more than doubled over that of the uncoupled layup wing. The optimum layup pattern among those we used was the $[+15_2/0]_s$ pattern. By examining the $[0_2/90]_s$ and the $[+30_2/0]_s$ layup wing results we can speculate that around a $[+20_2/0]_s$ layup wing would have the highest divergence speed.

Of all the analysis done in this project the divergence analysis gave results that best agreed with experimental results. This can

WING	$\Lambda = 0$ degrees		$\Lambda = -30$ degrees	
	Theoretical (m/s)	Experimental (m/s)	Theoretical (m/s)	Experimental (m/s)
[0 ₂ /90]s	29	*****	24	*****
[+15 ₂ /0]s	∞	*****	56	*****
[\pm 15/0]s	∞	*****	31.4	*****
[\mp 15/0]s	24.2	*****	20.9	19
[-15 ₂ /0]s	16.5	18	15.6	15
[+30 ₂ /0]s	∞	*****	39.4	*****
[\pm 30/0]s	∞	*****	26.1	*****
[\mp 30/0]s	24.7	24	18.5	17
[-30 ₂ /0]s	14.2	15	12.4	11
[+45 ₂ /0]s	∞	*****	21	20
[\pm 45/0]s	∞	*****	18.4	20
[\mp 45/0]s	24.1	22	14.9	14
[-45 ₂ /0]s	14.0	14	11.3	10

Table 4.1 Wing divergence speeds.

probably be attributed to the use of three dimensional aerodynamics. For the experiments, the wings were said to have diverged when at near zero degrees root angle of attack, the wing bent to a large deflection. Many times this deflection was oscillatory at a low frequency below first bending frequency. This oscillation was due to non linear effects and was beyond the scope of our analysis. For a few wings, like the [0₂/90]s layup wing, the divergence velocity was within the wind tunnel speed range but before reaching that speed in the experiment the wing fluttered. Therefore those divergence speeds, along with the ones higher

than maximum tunnel speed, were not verified by experiment.

4.4 Natural Frequencies

Ascertaining the natural frequencies from the initial deflection tests is a skill that requires some fine discrimination. Due to the nature of composite material, vibrations are damped in relation to their frequency. For some of the wings the second bending and first torsion vibrations were detectable on the strip chart for only a fraction of a second. The fact that all three frequencies are present on the same chart and for some wings the second bending and the first torsion frequencies are not very different and are highly coupled also complicated the problem. As a result for two wings we could not ascertain the second bending frequency and for all wings the measured second bending and first torsion frequencies are no more accurate than within about 2 hertz.

WING	First Bending		First Torsion		Second Bending	
	Theo.	Exp.	Theo.	Exp.	Theo.	Exp.
	(hz)	(hz)	(hz)	(hz)	(hz)	(hz)
[0 ₂ /90] _s	10.8	10.5	39	44	67	****
[+15/0] _s	8.5	9.2	48	48	58	66
[±15/0] _s	9.9	10.0	50	52	63	77
[+30 ₂ /0] _s	6.0	7.1	60	60	41	44
[±30/0] _s	7.8	8.0	65	68	50	****
[+45 ₂ /0] _s	4.6	6.2	55	48	31	32
[±45/0] _s	5.7	6.0	69	76	37	36

Table 4.2 Wing natural frequencies.

The results of the test along with the analytic results are shown in table 4.2. As expected, since all wings have the same mass, the bending and torsion frequencies are directly related to the bending and torsion stiffness. Comparing the calculated to the measured frequencies, we have generally good agreement. For the three highly coupled wings, the $[+15_2/0]_s$, $[+30_2/0]_s$ and $[+45_2/0]_s$, the measured first bending frequency was higher than calculated, while the measured first torsion frequency of the $[+45_2/0]_s$ was lower than calculated. These differences are probably due to the bending-torsion coupling in the wings, since both modes of vibration were present at the same time in the test.

4.5 Flutter Velocities

The data from the flutter boundary tests is plotted in Appendix D. Because of the way the boundaries are graphed we can see how the root angle of attack changes the flutter speed. The results of the flutter tests are shown in table D.1. From this table we can see the twist of the wing tip during flutter and therefore can calculate the tip angle of attack as well.

For those wings that at zero degrees angle of attack flutter before they diverge, a few general statements can be made concerning the change in flutter characteristics with root angle of attack. The type of flutter changes from a bending-torsion to more of a pure torsion flutter as angle of attack is increased. This can be seen by the flutter frequency increasing toward the first torsion frequency and a smaller amount of bending in the flutter. Also, the flutter airspeed decreases. For example, the $[0_2/90]_s$ layup wing unswept went from 33 hz to 40 hz, from a Δw of 0.7 cm to 0 cm, and from an airspeed of 26 m/s to 13 m/s at 10 degrees angle of attack. These same trends were noted by Rainey in previous stall flutter work in reference 14. However as the wings become coupled in bending and torsion these trends are changed. In the case of the $[+30_2/0]_s$ layup wing there is no frequency change and the airspeed is nearly the same for both 0 and 12 degrees angle of attack flutter. If we

examine the wing conditions we see that at 0 degrees angle of attack the average twist is +2.4 degrees, while at 12 degrees angle of attack the average twist is -4.8 degrees. Thus the tip is at an increased angle of attack of only about 4.8 degrees versus 12 degrees for the root. This could account for the similarity in flutter behavior at the two different root angles of attack.

The wings that diverged at 0 degrees root angle of attack before they would flutter all exhibited similar bending flutter behavior as angle of attack was increased. Generally the flutter speed would decrease, the frequency would increase and the flutter would become more mild, making it more like a bending flutter and less like divergence.

The wings that resisted flutter the best at low angle of attack were the [$\pm 30/0$]s and the [$\pm 45/0$]s layup wings. In fact, their flutter speeds were beyond the maximum speed of the wind tunnel. However, as angle of attack was increased their flutter speeds dropped below that of their unbalanced counterparts, the [$+30_2/0$]s and the [$+45_2/0$]s layup wings. Due to the light bending-torsion coupling of the balanced layup wings they exhibited the normal flutter trends talked about earlier including the decrease in flutter speed as root angle of attack is increased. Among the wings with an unbalanced laminate layup pattern a ply fiber angle of 30 degrees seems to give the highest flutter speed.

When the wings were swept forward the addition to angle of attack made by bending had a strong effect on flutter. The [$0_2/90$]s layup wing at 0 degrees angle of attack fluttered at a lower airspeed than when unswept, while at higher than about 8 degrees angle of attack it changed from a bending torsion flutter to a bending flutter. The [$+15_2/0$]s and [$+30_2/0$]s layup wings' bending-torsion coupling could not offset the increase in tip angle of attack due to bending so they also showed a decrease in flutter speed with an increase in root angle of attack. The [$+45_2/0$]s layup wing, being weak in bending, now diverged at all angles of attack. The frequency shown in table D.2 is a post divergence oscillation. Note that the average bending is nearly 17 cm! The wings

that had diverged at 0 degrees sweep also diverged at -30 degrees sweep, the speeds were just slightly lower.

The differences in the low angle of attack behavior of the various wings was also evident in the theoretical analysis. In order to examine a typical cross section of the wings I have taken the graphs for the four wings with 15 degree fiber ply angles from appendix D and reproduced them here in figure 4.4. Looking at the $[+15_2/0]_s$ layup wing first, the V-g method predicts the torsional branch will go unstable at 24 m/s at a frequency around 27 hz. The experimental values were 25 m/s and 32 hz. Note that as flutter velocity is approached the torsional branch has a large change in frequency. Looking at the other wing with negative bending-torsion flutter, the $[\pm 15/0]_s$ layup wing, we see behavior very similar to the $[+15_2/0]_s$ layup wing. The $[\pm 15/0]_s$ layup wing also goes unstable in the torsional branch, just at a slightly higher airspeed. The next two wings, the $[\mp 15/0]_s$ and the $[-15_2/0]_s$ layup wings both go unstable in the first bending branch. The branch is initially very stable but then at the critical velocity it rapidly goes to neutral stability while the frequency goes to zero. This shows classical divergence. The main difference between the two wings is that the $[-15_2/0]_s$ layup wing has a slightly lower divergence speed. The divergence speeds indicated here are lower than the experimental values because this analysis does not consider finite span effects in the aerodynamics.

For 0 degrees angle of attack the results of the divergence and V-g flutter analysis along with experimental data points are shown in figure 4.5. The unbalanced and balanced laminate wings are shown on separate graphs. The $[0_2/90]_s$ layup wing is plotted on both graphs. For completeness the V-g flutter analysis for the wings at 30 degrees swept back is included. There is no experimental data for 30 degrees swept back.

Let's look at the unbalanced laminate wings first. For the unswept wing if the fiber angle is below about -5 degrees divergence is the limiting factor otherwise the wing will flutter first. Despite the

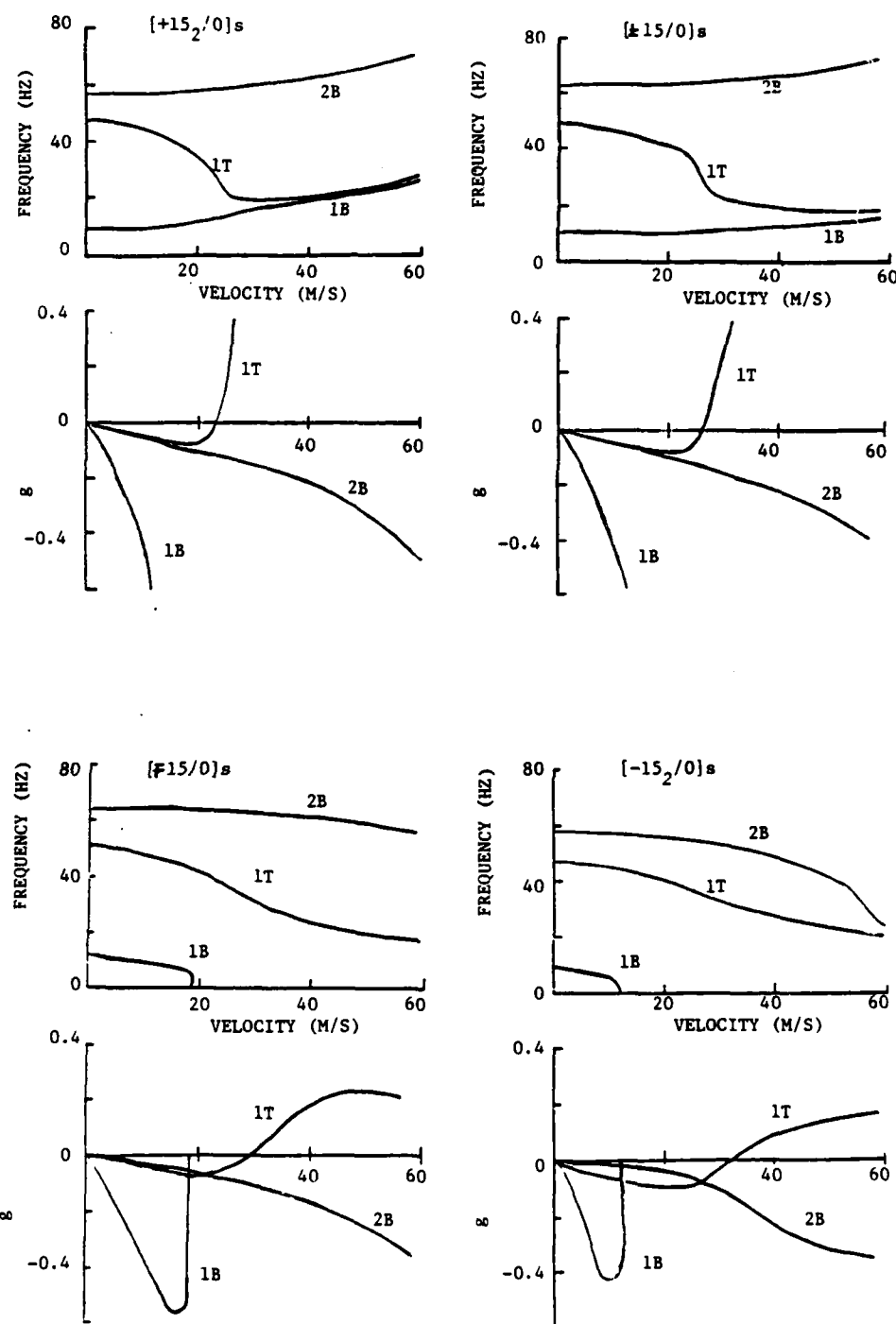


Figure 4.4 Flutter analysis diagrams for the four wings with a 15 degree ply fiber angle.

large variations in stiffness and bending-torsion coupling from the $[0_2/90]_s$ to the $[+45_2/0]_s$ layup wings, flutter speeds were all within 5 m/s for the four wings. A ply fiber angle of +30 degrees seems to give the highest flutter speed both theoretically and experimentally. For 30 degrees swept forward, due to the effect of bending on angle of attack, divergence dominates for all ply fiber angles except in the region of from about +5 to +30 degrees. In particular, we could not get the $[15_2/0]_s$ and $[+30_2/0]_s$ layup wings to flutter or diverge at low angle of attack in the available speed range of the wind tunnel. It is worthwhile to note that the limiting speed (either flutter or divergence) for 30 degrees swept forward is higher than for the unswept wing for fiber angles from -5 to +35 degrees according to the theoretical calculations and experimentally it was true for fiber angles of +15 and +30 degrees.

The $[0_2/90]_s$ layup wing went into torsional flutter with a large average bend at an airspeed below its calculated divergence speed. This was not predicted by the V-g analysis. Because of the large average bending deflection the wing was actually in a high angle of attack flutter despite the root angle of attack being only 1 degree. As we have seen previously, high angle of attack flutter for the $[0_2/90]_s$ layup wing is lower than when at low angle of attack. Also this type of flutter is not covered by our analysis. Looking back at the steady airload analysis we see that when a wing is close to, yet still below divergence speed, it has large deflection even at low angle of attack. In the swept forward case bending causes increases in angle of attack so we can see how when nearing divergence speed even with a low root angle of attack we can get a high tip angle of attack bringing with it the possibility of flutter.

Switching now to the balanced laminate wings, for the unswept case we have divergence for outer layer fiber angles below -10 degrees and flutter elsewhere. These wings had the highest predicted flutter speed at a outer ply fiber angle of +45 degrees. This speed was higher than the tunnel maximum speed so we could not determine its accuracy. Experimental data was reasonable except for the $[+15/0]_s$ layup wing which will be discussed in the next paragraph.

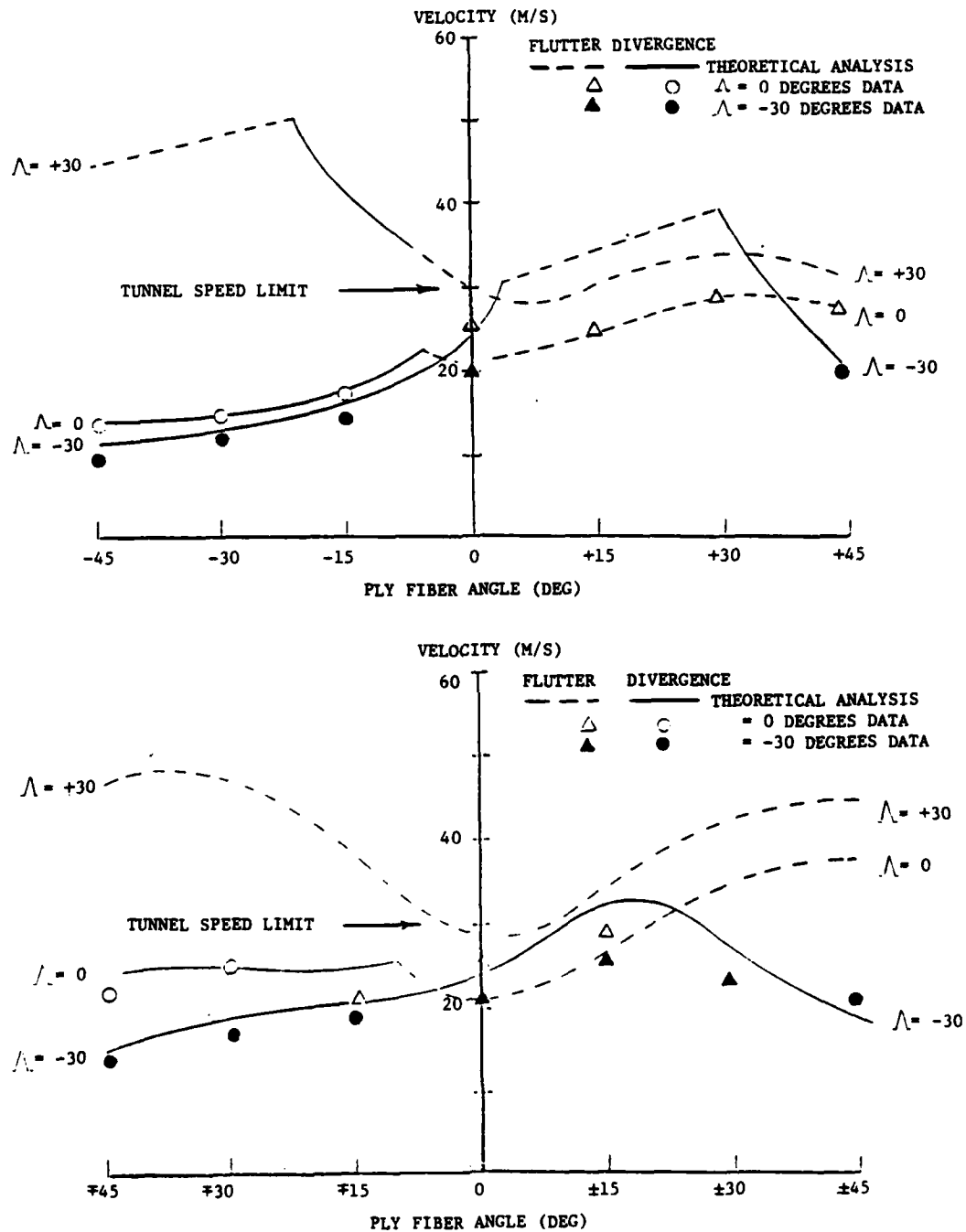


Figure 4.5 Effects of fiber ply angle on flutter and divergence speeds.

For 30 degrees forward sweep for the balanced laminate wings, divergence was the limiting instability throughout the fiber angle range. We see a calculated best outer fiber angle of about +20 degrees. Experimental data was close to calculated with the following exceptions; the $[0_2/90]_s$, $[\pm 15/0]_s$, $[\pm 30/0]_s$ at 30 degrees forward sweep and the $[\mp 15/0]_s$ layup wing from the unswept wing case. The $[0_2/90]_s$ layup wing was discussed previously and in fact what was said for the $[0_2/90]_s$ layup wing also applies to all these wings. Their cases are all torsional flutter characterized by high average bending and speeds below predicted divergence speed, suggesting a high angle of attack flutter at the wing tip. By checking the average bending deflection (w_{avg}) in table D.2 for the $[\pm 30/0]_s$ layup wing (19.8 cm), one could argue that in fact the wing has diverged and the calculated divergence speed is just too high. However I present the argument that before the wing diverged it bent enough to allow for high angle of attack flutter. Once the wing is fluttering, the increase in average force caused by flutter caused the wing to bend even more (see discussion section 4.2), thus the high average bend. Whatever your point of view, one thing for sure is that we have reached a stability limit and it is at a airspeed lower than the airspeed predicted by the theoretical analysis.

CHAPTER 5. CONCLUSIONS AND RECOMENDATIONS

Having now investigated some of the many varied and interesting properties demonstrated by the graphite/epoxy composite material wings I will finish by pointing out a few of the conclusions we can make and offer some recomendations for follow up work.

The wings showed very near linear bending and twisting behavior up to large deflections in the static tests. This gives a large useful range in which we can apply our linear theory. However, on lightly bending-torsion coupled wings small imperfections in the wings such as warp can cause large deviations from linear theory concerning the bending-torsion stiffness coupling reaction.

The steady airload analysis gave good results up to 20 degrees angle of attack as long as the wing did not flutter. Certainly the use of a realistic lift curve, rather than a linear one, contributed to the accuracy of the results. Once the wings did flutter they had an average deflection greater than the steady airload theory predicted. This limited the useful range of the steady airload analysis and suggests the usefulness of investigation into the resultant average forces present during flutter, both lift and drag.

The initial deflection frequency tests were a quick easy way to get approximate values for the natural frequencies.

The divergence and flutter investigation once again showed the large variation in wing aeroelastic properties caused by changes in ply fiber angle. Straight wings can be made divergence free, while by proper selection of fiber angle, even a swept forward wing can have a divergence speed higher than a similar wing without bending-torsion coupling at no sweep. By using three dimensional aerodynamics the divergence speeds of the wings were closely predicted for both straight and forward swept wings. The flutter calculations for the straight wings were resonably accurate. We were unable to check the accuracy of the flutter calculations for the forward swept wings because of the wind tunnel's low maximum speed. However, by extrapolating to low angles of attack the

experimental data we were able to obtain at high and moderate angles of attack, we can predict a flutter speed close to the theoretically calculated flutter speed. We did discover that the lightly coupled wings had a tendency to go into a torsional flutter, characterized by a high average bend and therefore a high angle of attack at the wing tip, when approaching but still below predicted divergence speed. This phenomenon deserves further investigation. A stall or high angle of attack flutter analysis might give some insight here.

Finally, a good follow on investigation would be to make and test some built-up wings versus the cantilevered plates used here. A built-up wing with a typical box-beam or honeycomb construction would smooth out any initial warp or twist in the laminate skin, thus eliminating one of the problems we had. That type wing would be closer to a practical airfoil and is the next logical step toward building a functional graphite/epoxy composite material wing.

REFERENCES AND BIBLIOGRAPHY

1. Hertz, T.J.; Ricketts, R.H. and Weisshaar, T.A., "On the Track of Practical Forward-Swept Wings", *Astronautics and Aeronautics Magazine*, January 1982.
2. Hollowell, S.J., "Aeroelastic Flutter and Divergence of Graphite/Epoxy Cantilevered Plates with Bending-Torsion Stiffness Coupling", M.S. Thesis, Department of Aeronautics and Astronautics, M.I.T., January 1981.
3. Jensen, D.W., "Natural Vibrations of Cantiliver Graphite/Epoxy Plates with Bending-Torsion Coupling", M.S. Thesis, Department of Aeronautics and Astronautics, M.I.T., August 1981.
4. Selby, H.P., "Aeroelastic Flutter and Divergence of Rectangular Wings with Bending-Torsion Coupling", M.S. Thesis, Department of Aeronautics and Astronautics, M.I.T., January 1982.
5. Hollowell, S.J. and Dugundji, J., "Aeroelastic Flutter and Divergence of Stiffness Coupled, Graphite/Epoxy, Cantilevered Plates", 23rd AIAA/ASME/ASCE/AHS Structures, Structural Dynamics and Materials Conference, New Orleans, La., May 10-12, 1982, AIAA Paper 82-0722.
6. Tsai, S.W. and Hahn, H.T., "Introduction to Composite Materials", Technomic Publishing Co. Inc. 1980.
7. Bisplinghoff, R.J.; Ashley, H. and Halfman, R.L. "Aeroelasticity", Addison-Wesley Publishing Co. 1955.
8. Bisplinghoff, R.J. and Ashley, H., "Principals of Aeroelasticity", Dover Publications, Inc. 1962.

9. Dowell, E.H., "A Modern Course in Aeroelasticity", Sijthoff and Noordhoff 1980.
10. Riegels, F.W. "Aerofoil Sections", Butterworths Publishing House, 1961.
11. DeYoung, J. and Harper, C.W., "Theoretical Symmetrical Span Loading at Subsonic Speeds for Wings Having Arbitrary Planforms", NACA Report 921, 1948.
12. Spielberg, I.N., "The Two-Dimensional Incompressible Aerodynamic Coefficients For Oscillatory Changes in Airfoil Camber", Journal of the Aeronautical Sciences, June 1953.
13. Weisshaar, T.A. "Divergence of Forward Swept Composite Wings", Journal of Aircraft, June 1980.
14. Rainey, A.G., "Preliminary Study of Some Factors Which Affect the Stall-Flutter Characteristics of Thin Wings", NACA TN 3622, March 1956.

APPENDIX A

MODE SHAPE INTEGRALS

AND

THEIR NUMERICAL VALUES

$$\left\{ \text{using } \phi_i' = \frac{d\phi_i}{dx} \quad \text{and} \quad \phi_i'' = \frac{d^2\phi_i}{dx^2} \right\}$$

$$I_1 = \frac{1}{l} \int_0^l (\phi_1)^2 dx = 1.000$$

$$I_2 = \frac{1}{l} \int_0^l (\phi_2)^2 dx = 1.000$$

$$I_3 = \frac{1}{l} \int_0^l (\phi_3)^2 dx = 0.500$$

$$I_4 = \frac{1}{l} \int_0^l (\phi_4)^2 dx = 0.500$$

$$I_5 = \frac{1}{l} \int_0^l (\phi_5)^2 dx = .03333$$

$$I_6 = l^3 \int_0^l (\phi_1'')^2 dx = 12.36$$

$$I_7 = l^2 \int_0^l \phi_1'' \phi_3' dx = 3.744$$

$$I_8 = l^2 \int_0^l \phi_1'' \phi_4' dx = 3.249$$

$$I_9 = l \int_0^l \phi_1'' \phi_5 dx = 0.4340$$

$$I_{10} = l^3 \int_0^l (\phi_2'')^2 dx = 485.7$$

$$I_{11} = l^2 \int_0^l \phi_2'' \phi_3' dx = -6.698$$

$$I_{12} = l^2 \int_0^l \phi_2'' \phi_4' dx = 63.55$$

$$I_{13} = l \int_0^l \phi_2'' \phi_5 dx = -2.868$$

$$I_{14} = l^3 \int_0^l (\phi_3'')^2 dx = 3.044$$

$$I_{15} = l \int_0^l (\phi_3')^2 dx = 1.234$$

$$I_{16} = l^2 \int_0^l \phi_3'' \phi_5' dx = 0.4293$$

$$I_{17} = \int_0^l \phi_3' \phi_5 dx = 0.1739$$

$$I_{18} = l^3 \int_0^l (\phi_4'')^2 dx = 246.6$$

$$I_{19} = l \int_0^l (\phi_4')^2 dx = 11.10$$

$$I_{20} = l^2 \int_0^l \phi_4'' \phi_5' dx = -6.712$$

$$I_{21} = \int_0^l \phi_4' \phi dx = -0.3023$$

$$I_{22} = l^3 \int_0^l (\phi_5'')^2 dx = 4.000$$

$$I_{23} = l \int_0^l (\phi_5')^2 dx = 0.3334$$

$$I_{24} = \int_0^l \phi_1' \phi_1 dx = 2.000$$

$$I_{25} = \int_0^l (\phi_1')^2 dx = 4.6478$$

$$I_{26} = \int_0^l \phi_1 \phi_2' dx = -4.7594$$

$$I_{27} = \int_0^l \phi_1' \phi_2 dx = 0.7595$$

$$I_{28} = \int_0^l \phi_1' \phi_2' dx = -7.3797$$

$$I_{29} = \frac{1}{l} \int_0^l \phi_1 \phi_3 dx = 0.67786$$

$$I_{30} = \int_0^l \phi_1' \phi_3 dx = 1.5173$$

$$I_{31} = \frac{1}{l} \int_0^l \phi_1 \phi_4 dx = -0.19609$$

$$I_{32} = \int_0^l \phi_1' \phi_4 dx = 0.146305$$

$$I_{33} = \frac{1}{l} \int_0^l \phi_1 \phi_5 dx = 0.12344$$

AD-A127 014 AEROELASTIC PROPERTIES OF STRAIGHT AND FORWARD SWEPT
GRAPHITE/EPOXY WINGS(U) AIR FORCE INST OF TECH
WRIGHT-PATTERSON AFB OH R J LANDSBERGER FEB 83

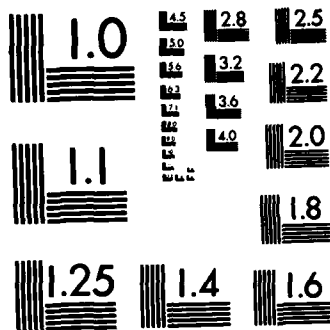
2/2

UNCLASSIFIED WRIGHT-PATTERSON
AFIT/CI/NR-83-11T

F/G 28/4

NL

END



MICROCOPY RESOLUTION TEST CHART
NATIONAL BUREAU OF STANDARDS-1963-A

$$I_{34} = \int_0^l \phi_1' \phi_5 \, dx = 0.35466$$

$$I_{35} = \int_0^l \phi_2' \phi_2 \, dx = 2.000$$

$$I_{36} = l \int_0^l (\phi_2)^2 \, dx = 32.4163$$

$$I_{37} = \frac{1}{l} \int_0^l \phi_2 \phi_3 \, dx = 0.1936$$

$$I_{38} = \int_0^l \phi_2' \phi_3 \, dx = -2.7155$$

$$I_{39} = \frac{1}{l} \int_0^l \phi_2 \phi_4 \, dx = 0.61191$$

$$I_{40} = \int_0^l \phi_2' \phi_4 \, dx = 2.8612$$

$$I_{41} = \frac{1}{l} \int_0^l \phi_2 \phi_5 \, dx = 0.13016$$

$$I_{42} = \int_0^l \phi_2' \phi_5 \, dx = -0.2524$$

$$I_{43} = \frac{1}{l} \int_0^l \phi_3 \phi_5 \, dx = 0.11074$$

$$I_{44} = \frac{1}{l} \int_0^l \phi_4 \phi_5 \, dx = 0.06414$$

APPENDIX B

STATIC DEFLECTION

INVESTIGATION RESULTS

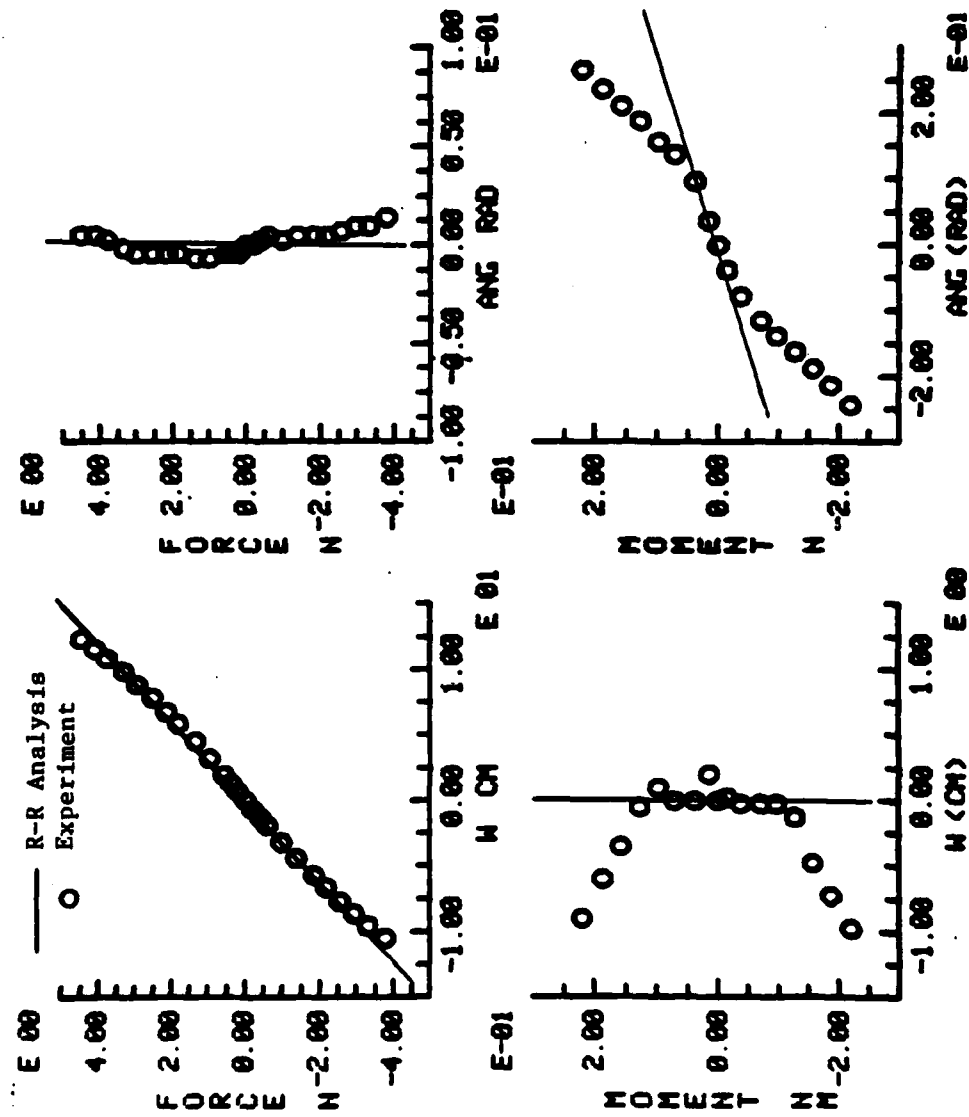


Figure B.1 $[0_2/90]_s$ layup wing, static deflection.

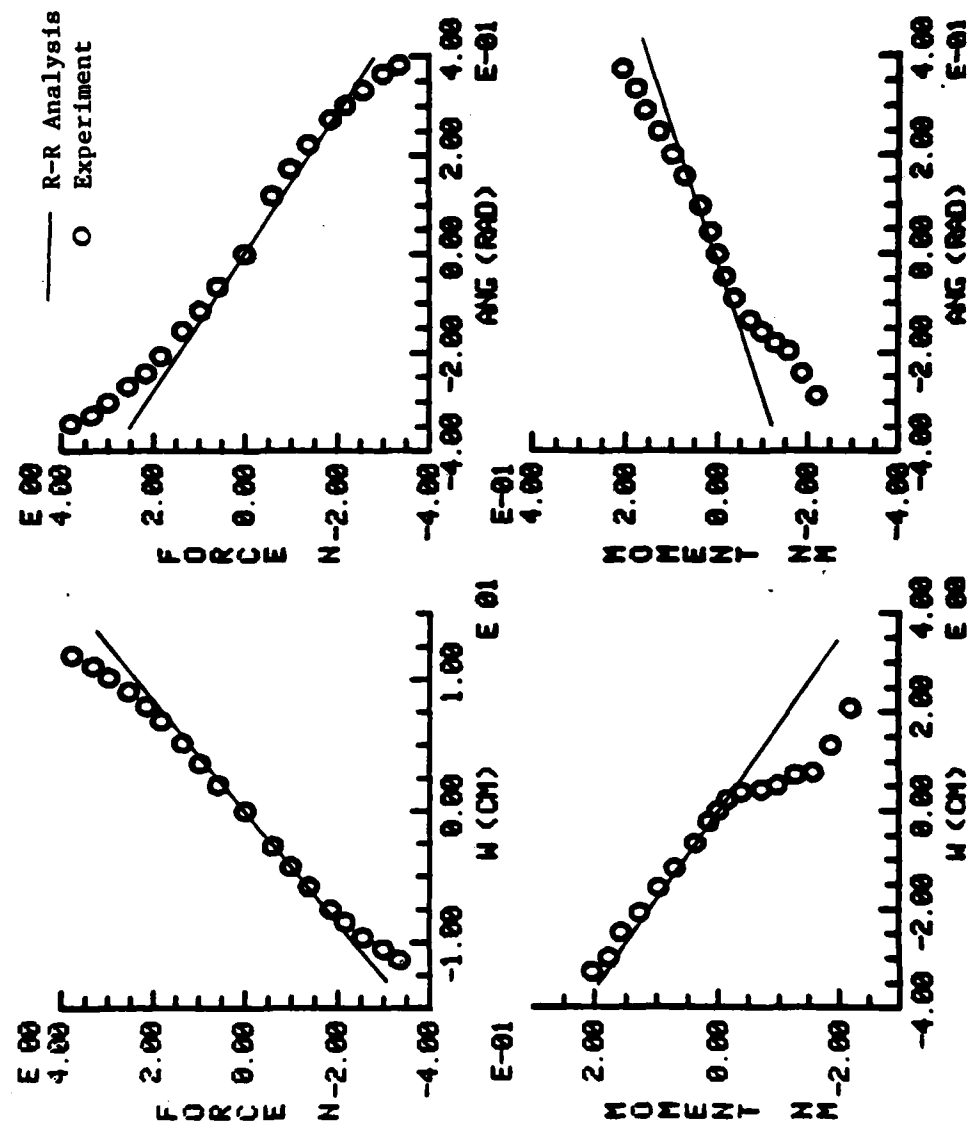


Figure B.2 [+15₂/0₂s] layup wing, static deflection.

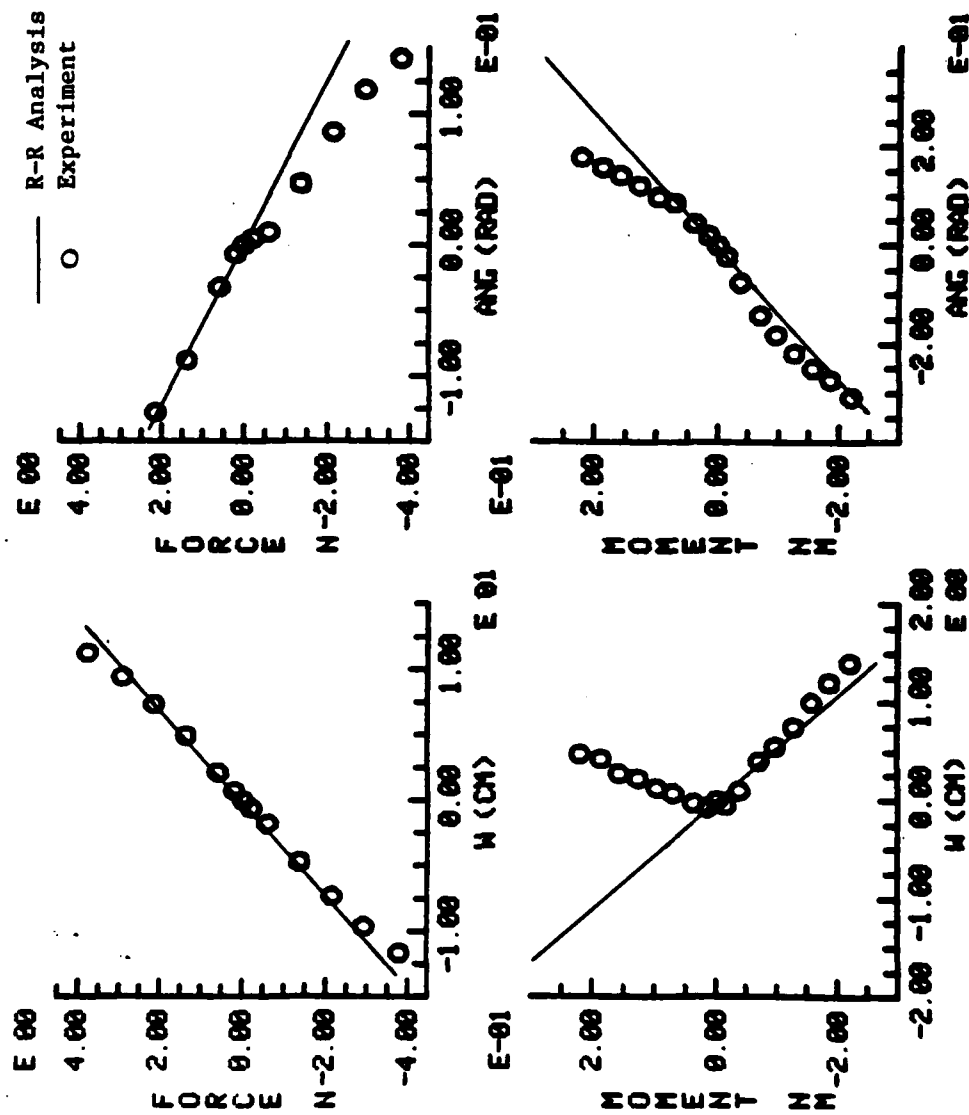


Figure B.3 $[\pm 15/0]_s$ layup wing, static deflection.

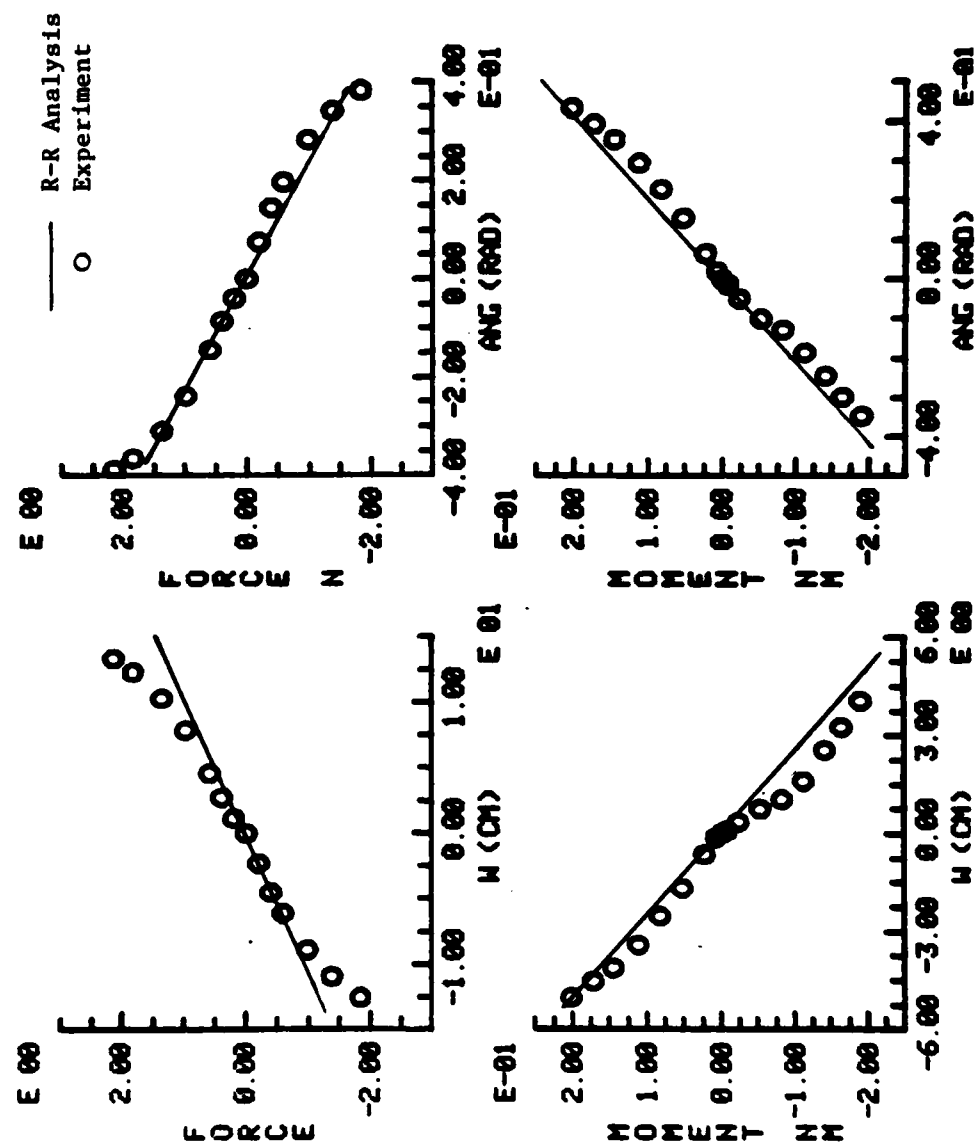


Figure B.4 $[+30_2/0]_s$ layup wing, static deflection.

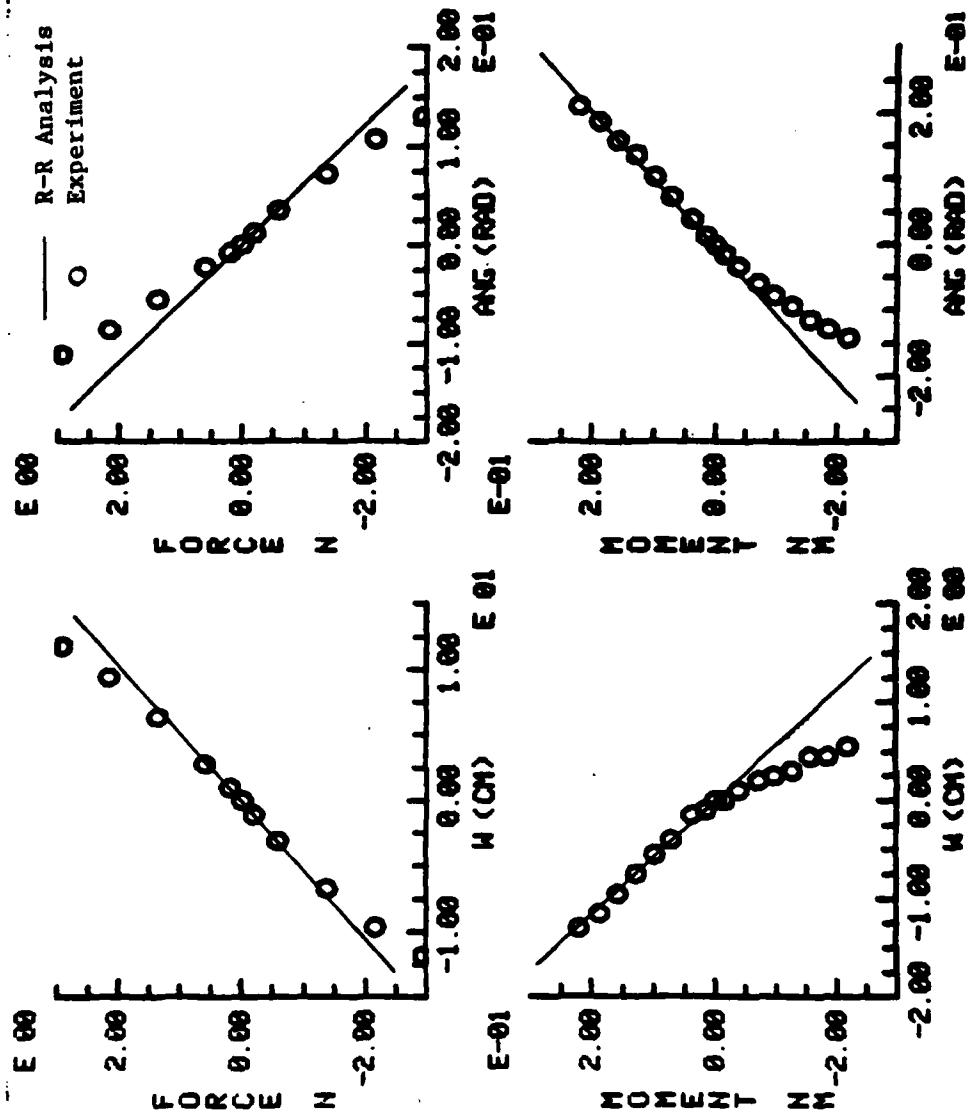


Figure B.5 [$\pm 30/0$]s layup wing, static deflection.

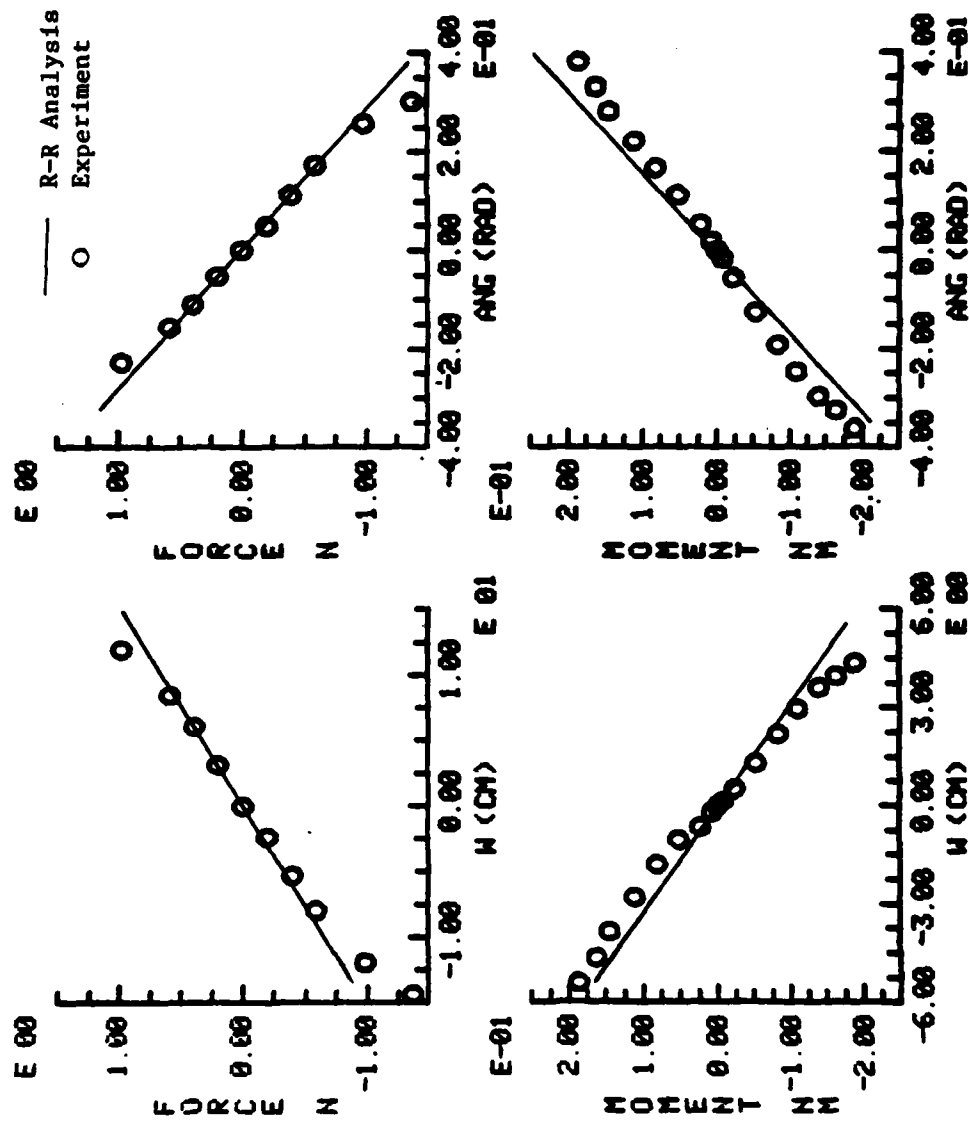


Figure B.6 [+45₂/0]s layup wing, static deflection.

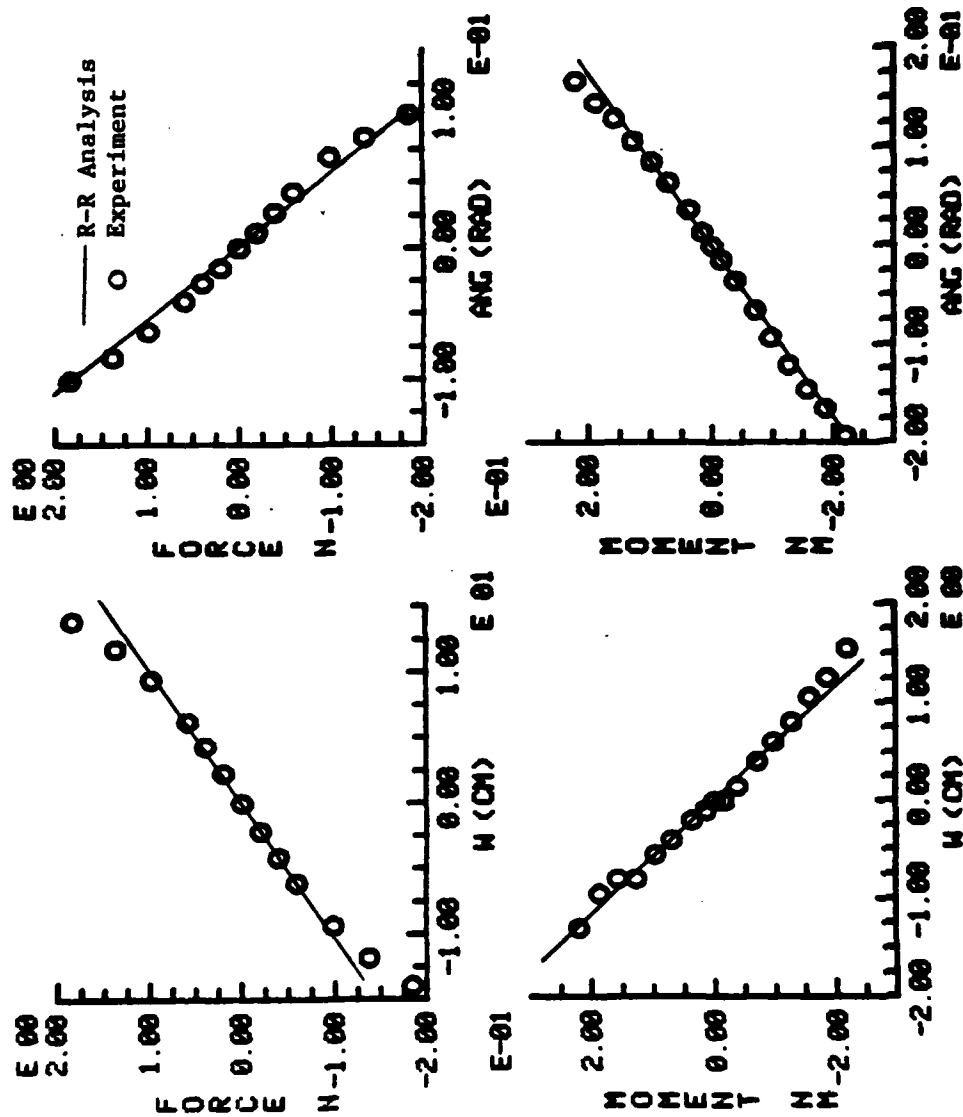


Figure B.7 $[\pm 45/0]_s$ layup wing, static deflection.

APPENDIX C

STEADY AIRLOAD

INVESTIGATION RESULTS

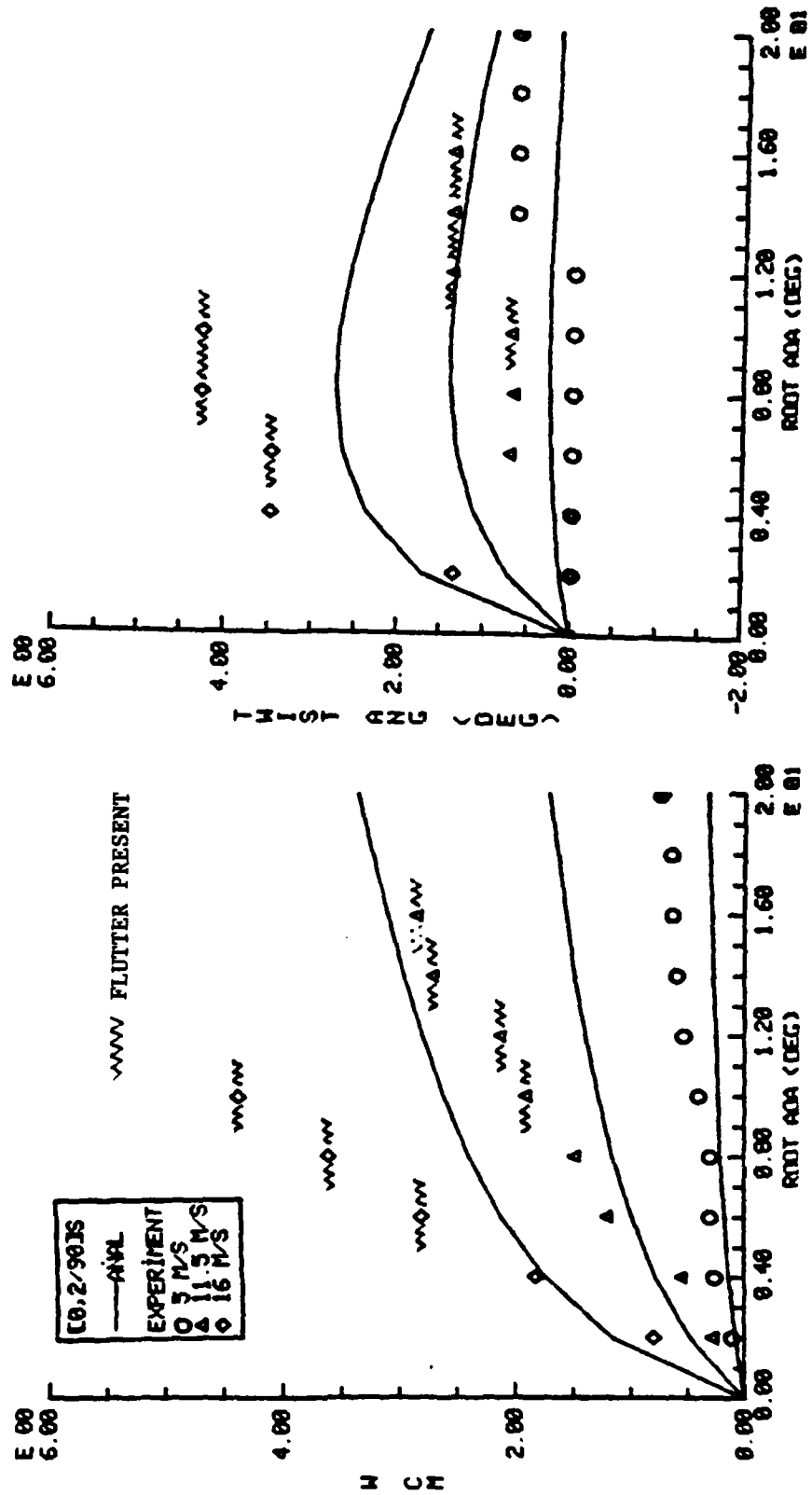


Figure C.1 [0₂/90]_s layup wing, steady airload deflection.

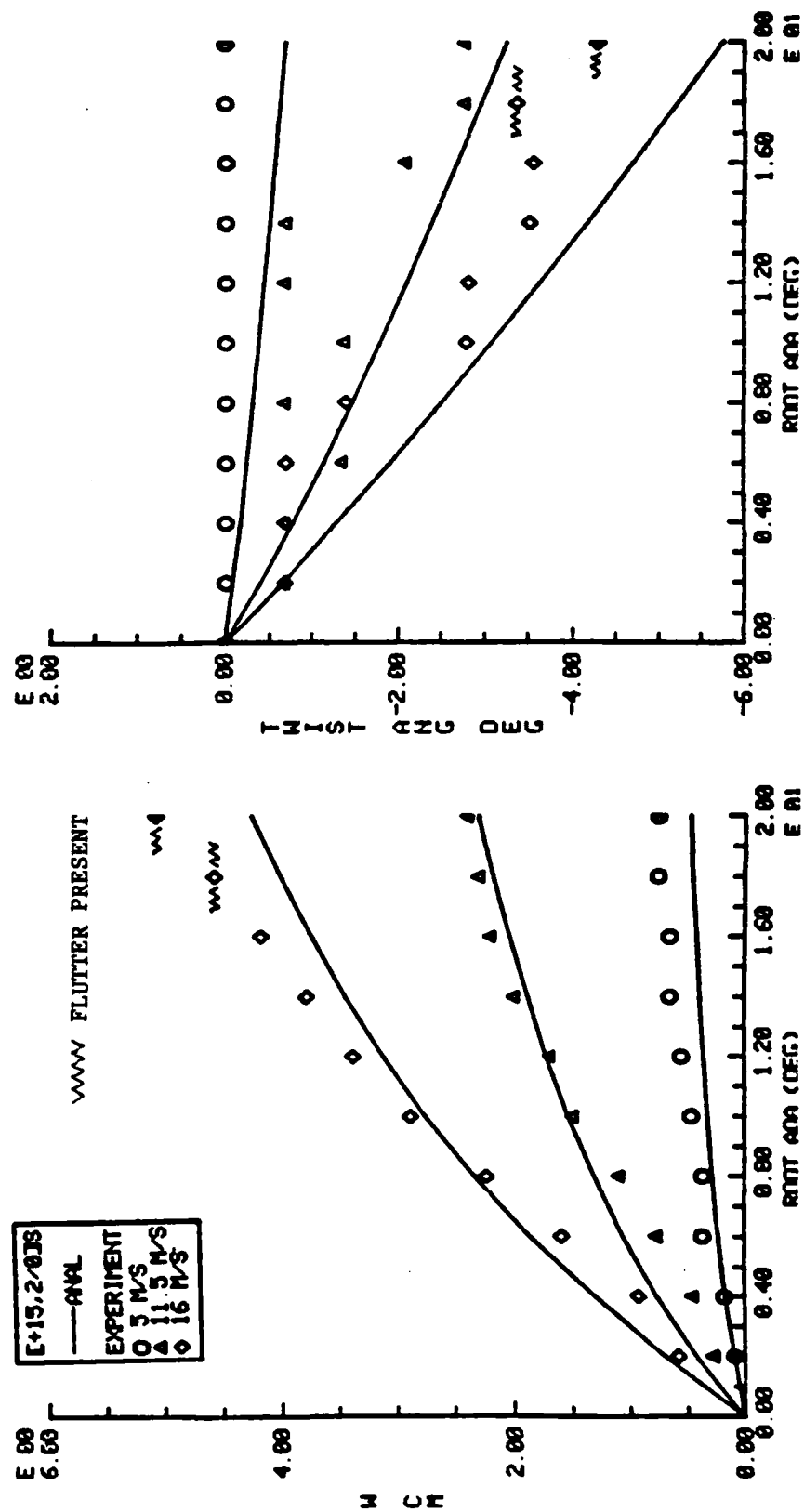


Figure C.2 [+15₂/0]s layup wing, steady airload deflection.

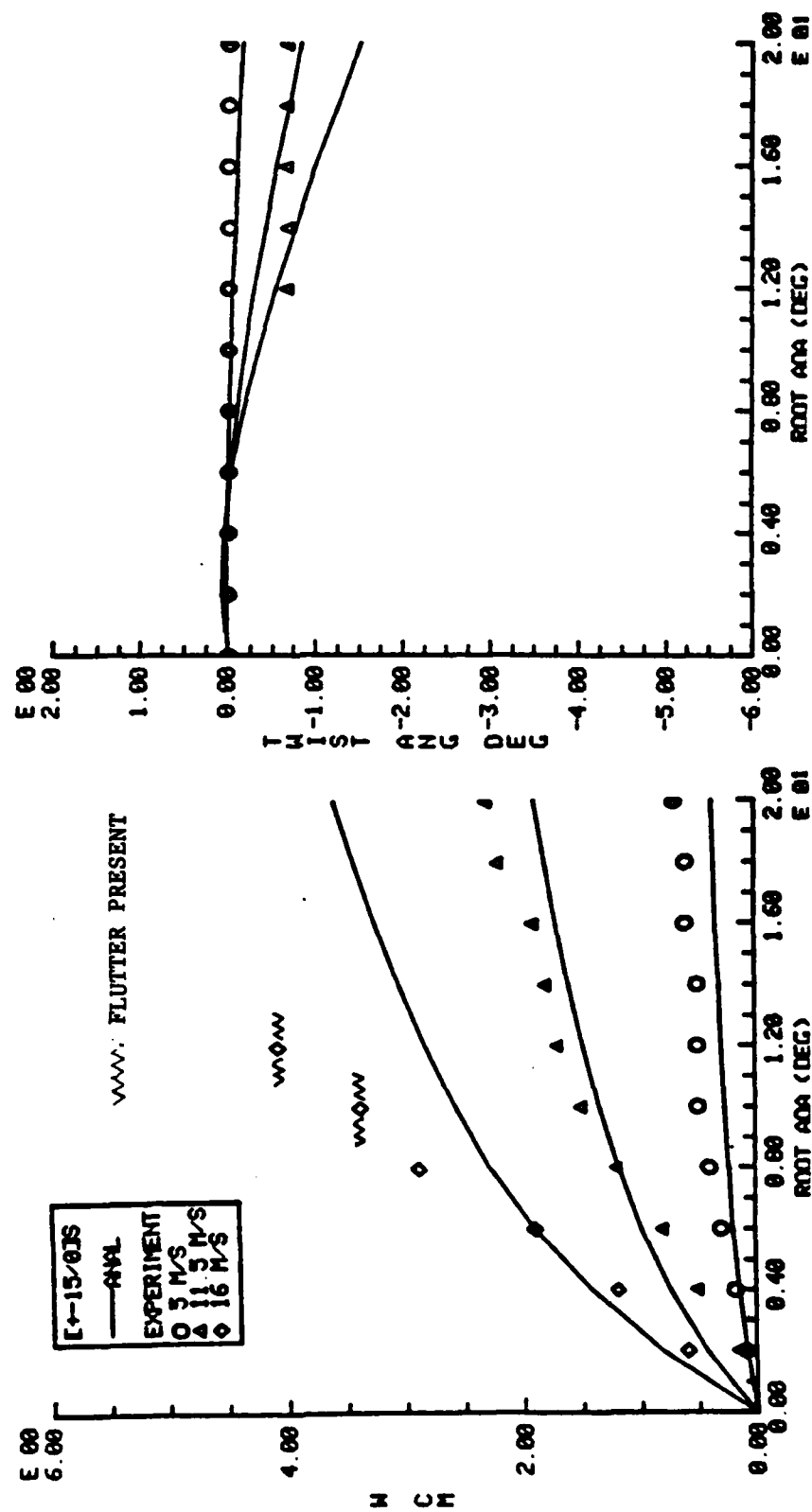


Figure C.3 [$\pm 15/0$]_s layup wing, steady airload deflection.

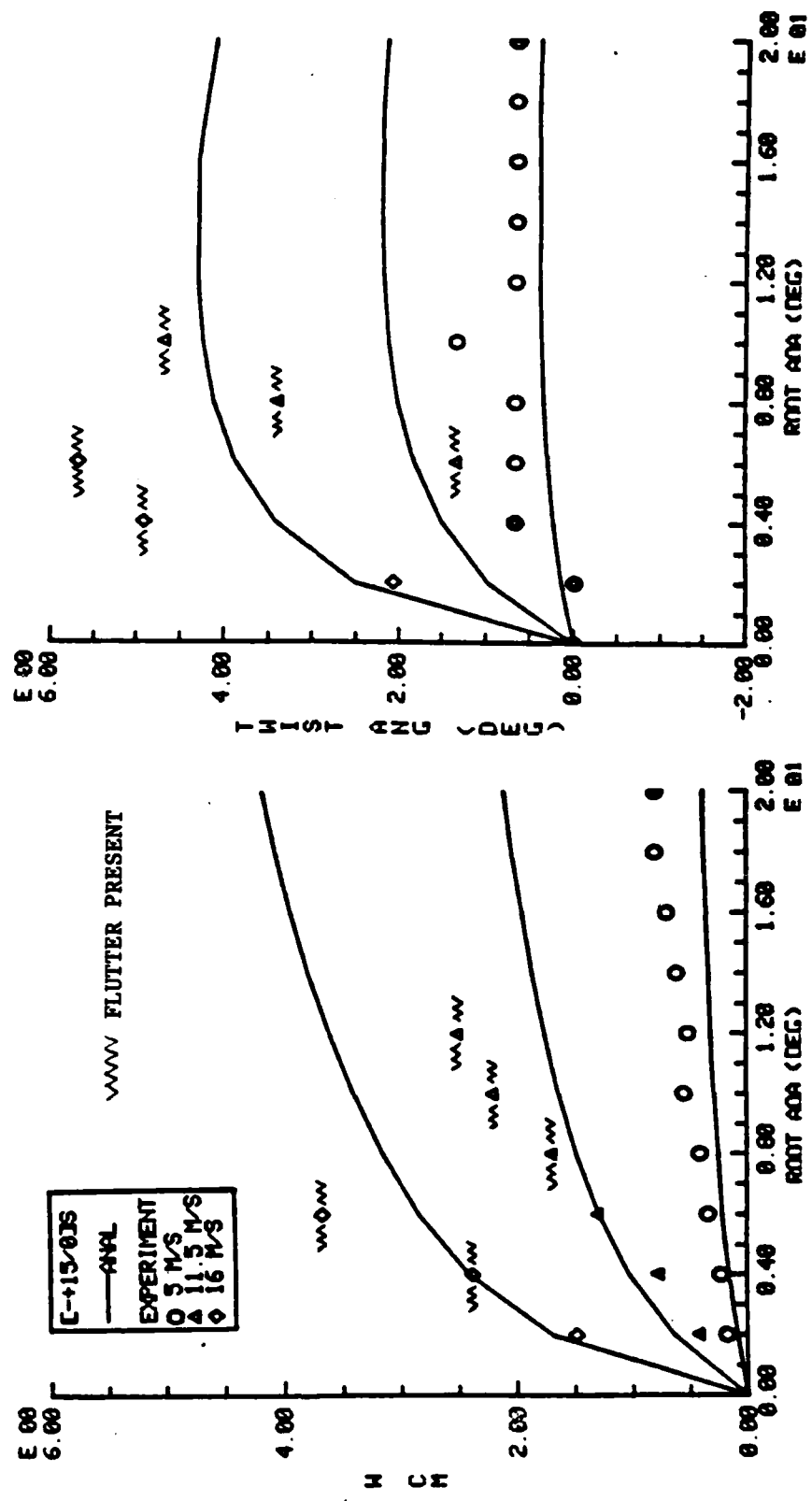


Figure C.4 [F15/O]s layout wing, steady airload deflection.

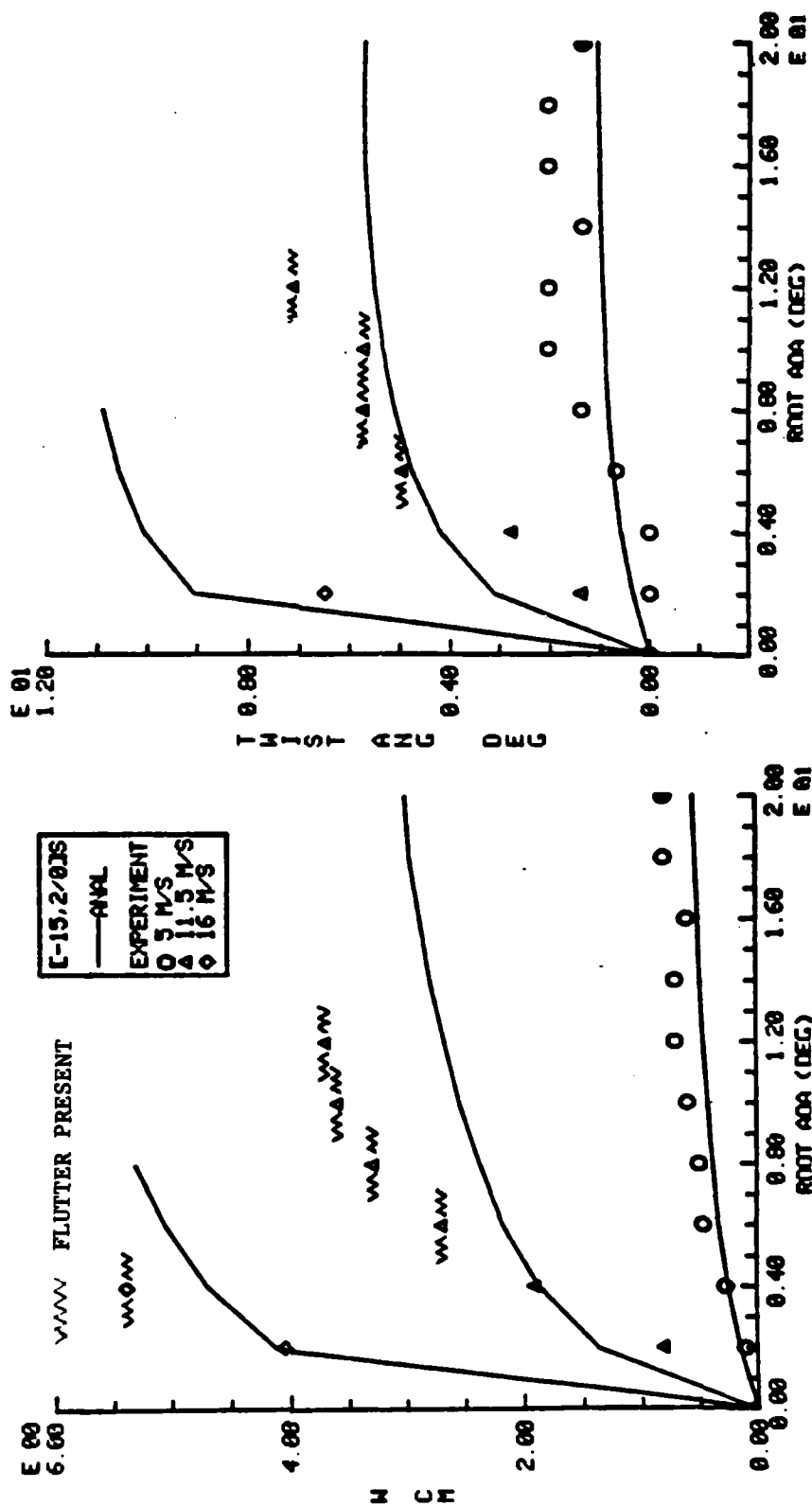


Figure C.5 [-15₂/0]s layout wing, steady airload deflection.

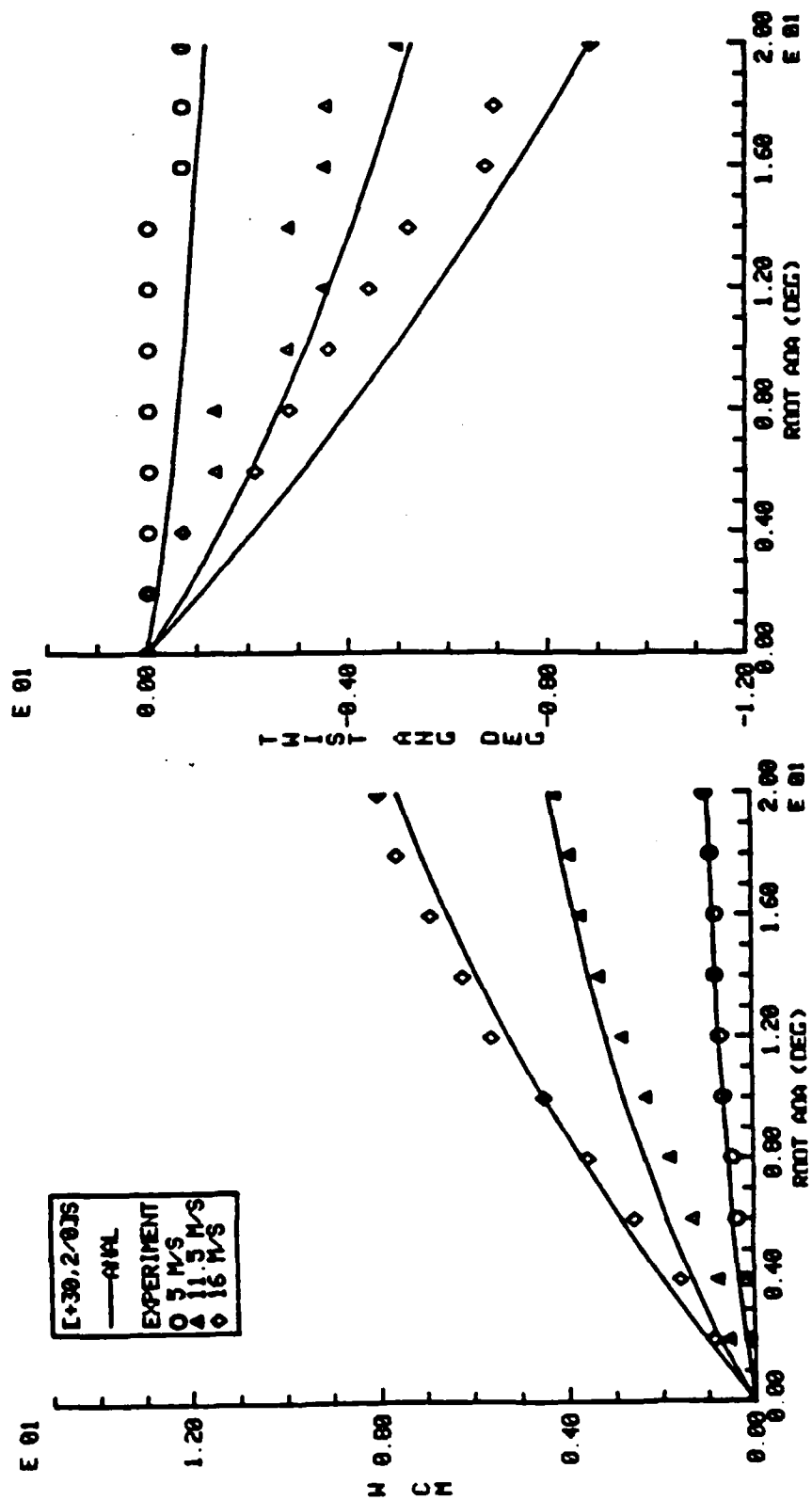


Figure C.6 [+30₂/0]s layup wing, steady airload deflection.

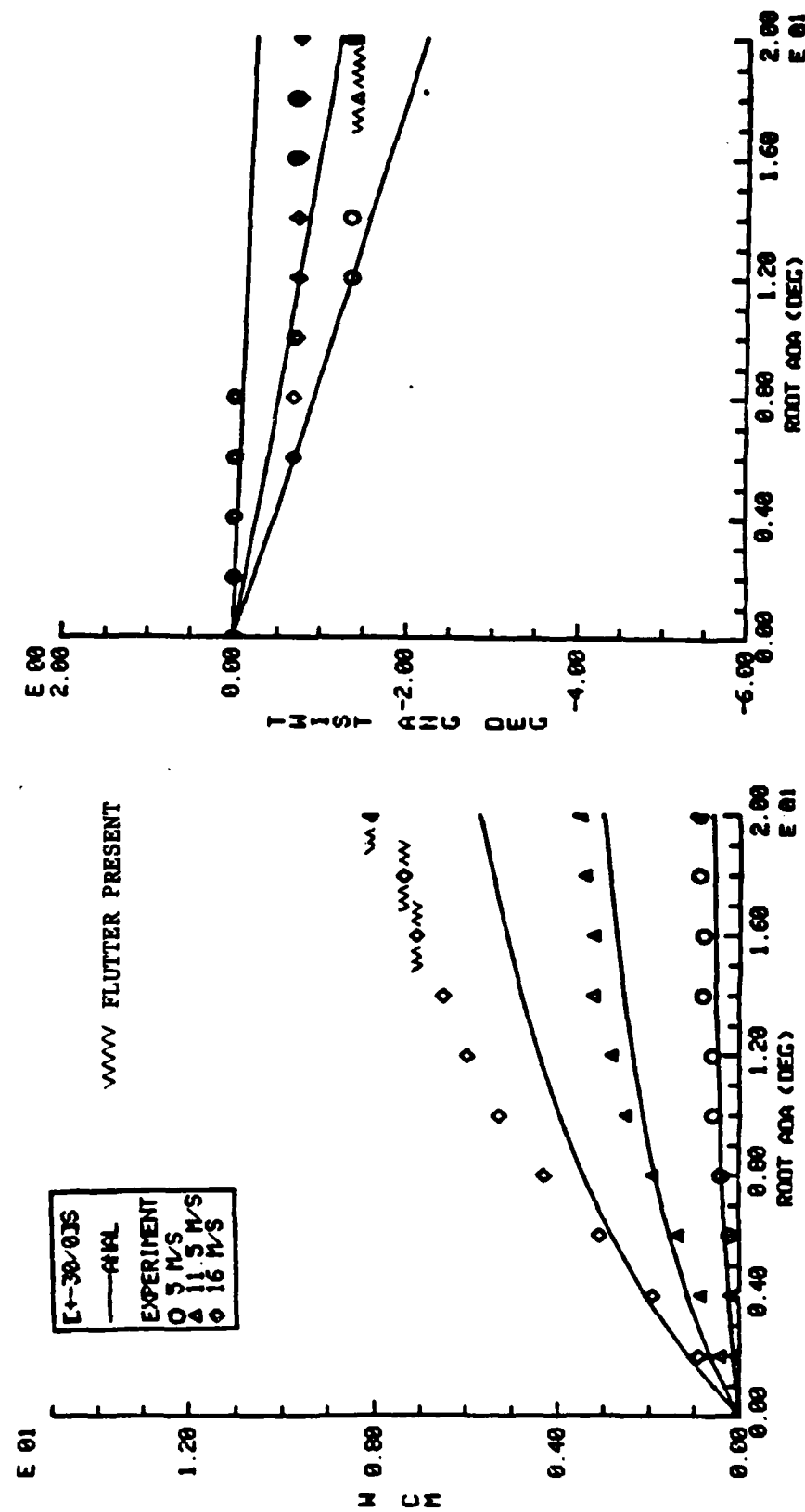


Figure C.7 $\pm 30/0^\circ$ s layout wing, steady airload deflection.

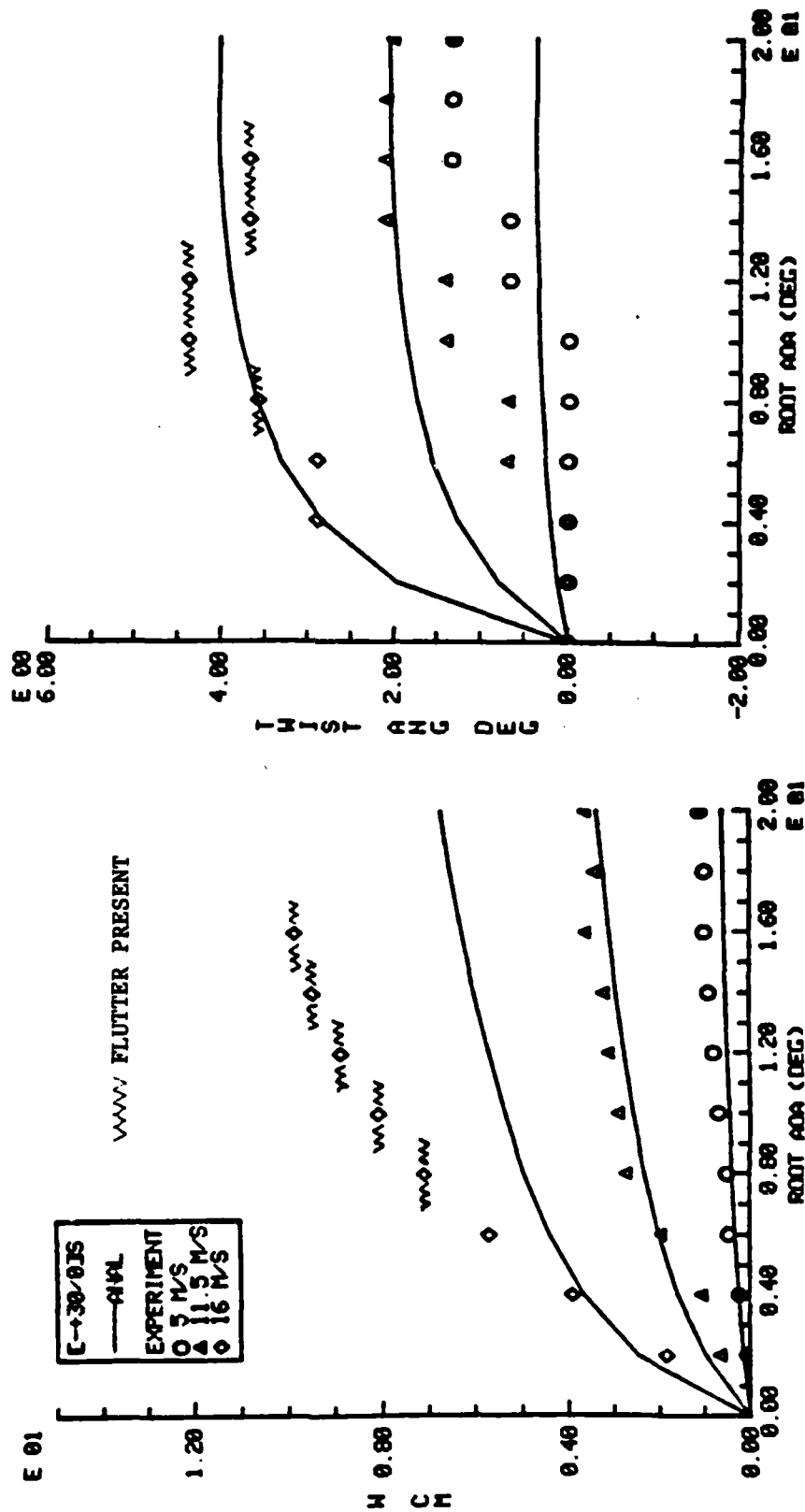


Figure C.8 [F30/O]s layout wing, steady airload deflection.

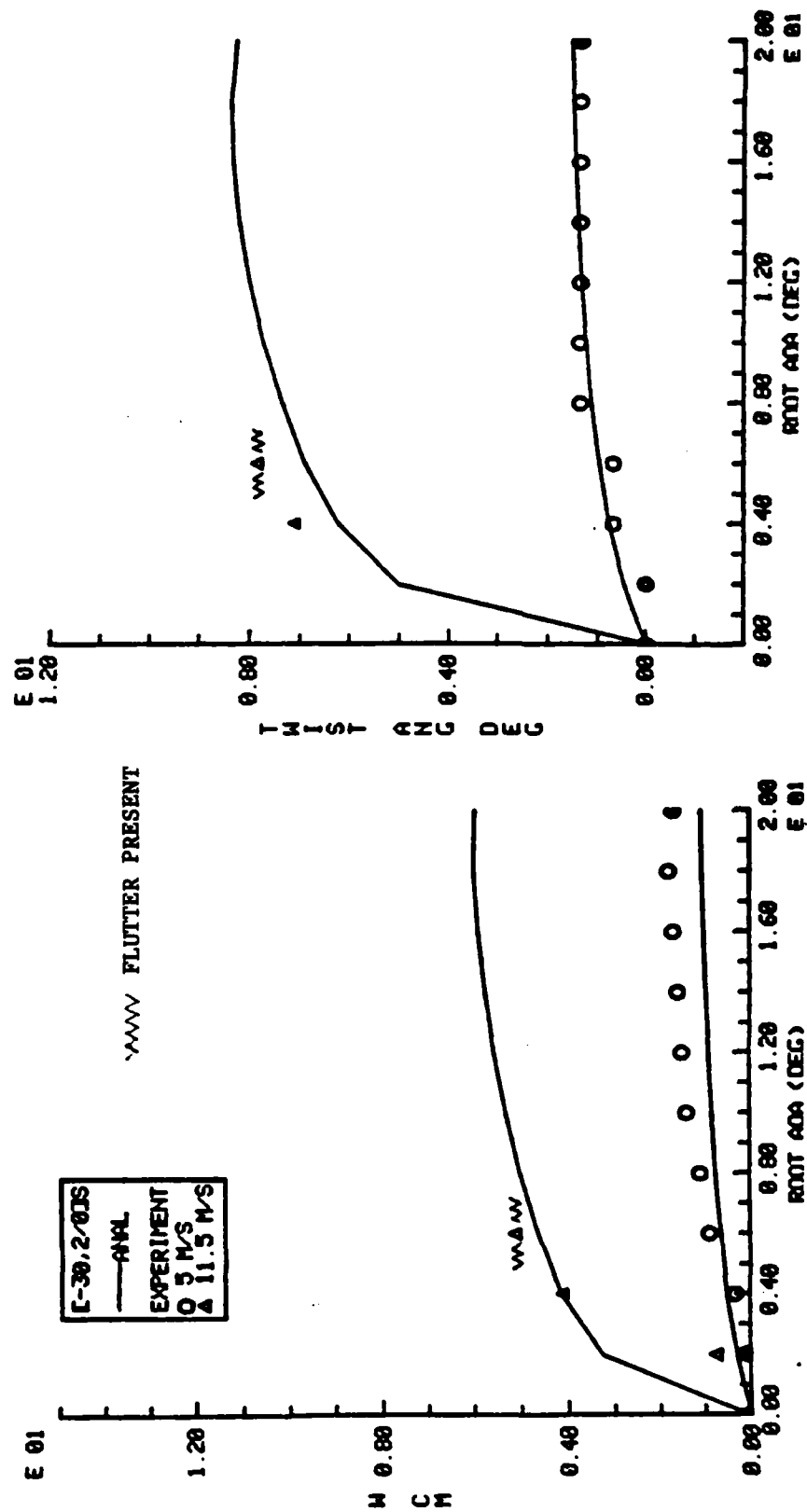


Figure C.9 [-30₂/0]s layout wing, steady airload deflection.

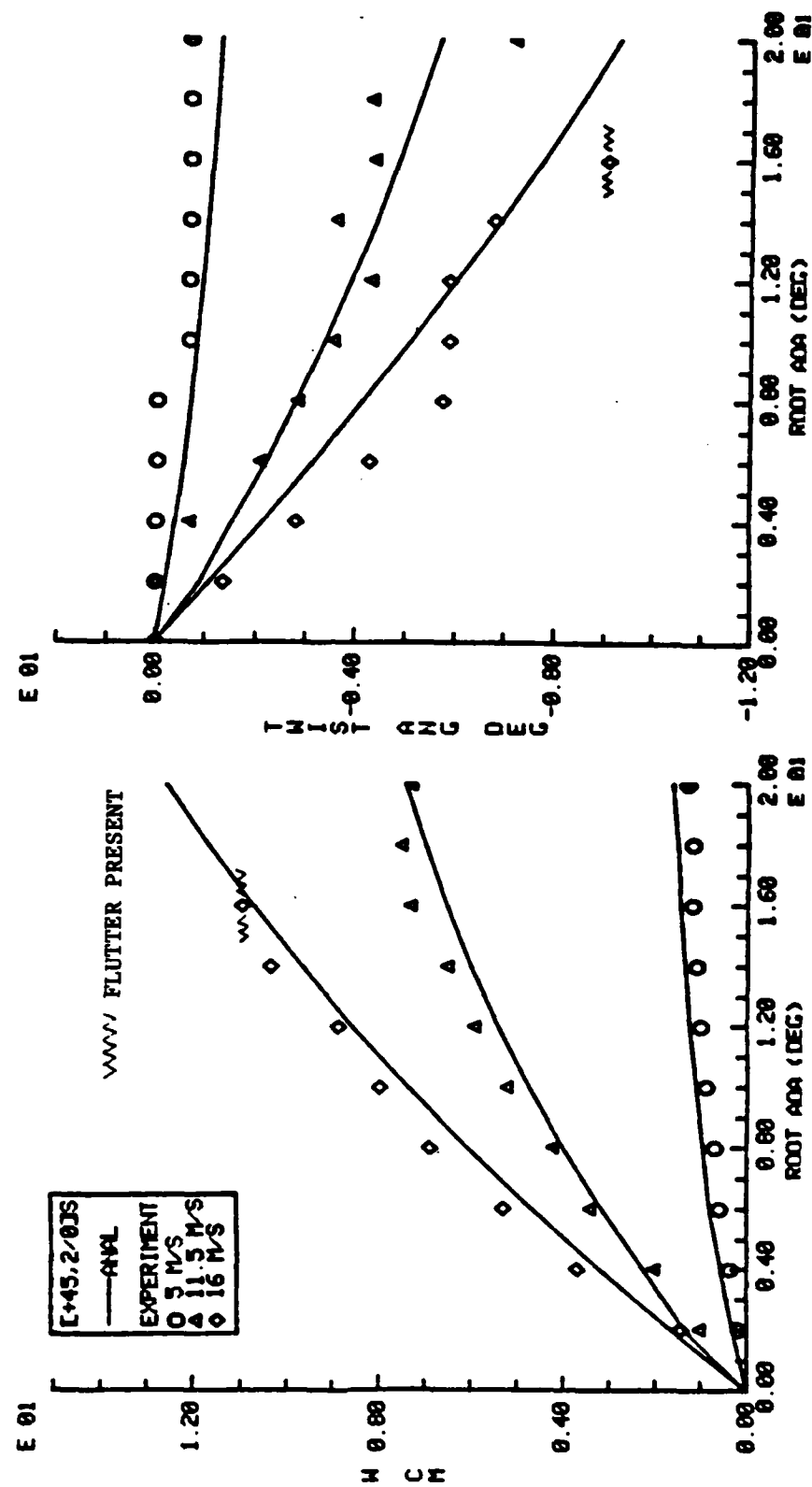


Figure C.10 [+45₂/0]_s layup wing, steady airload deflection.

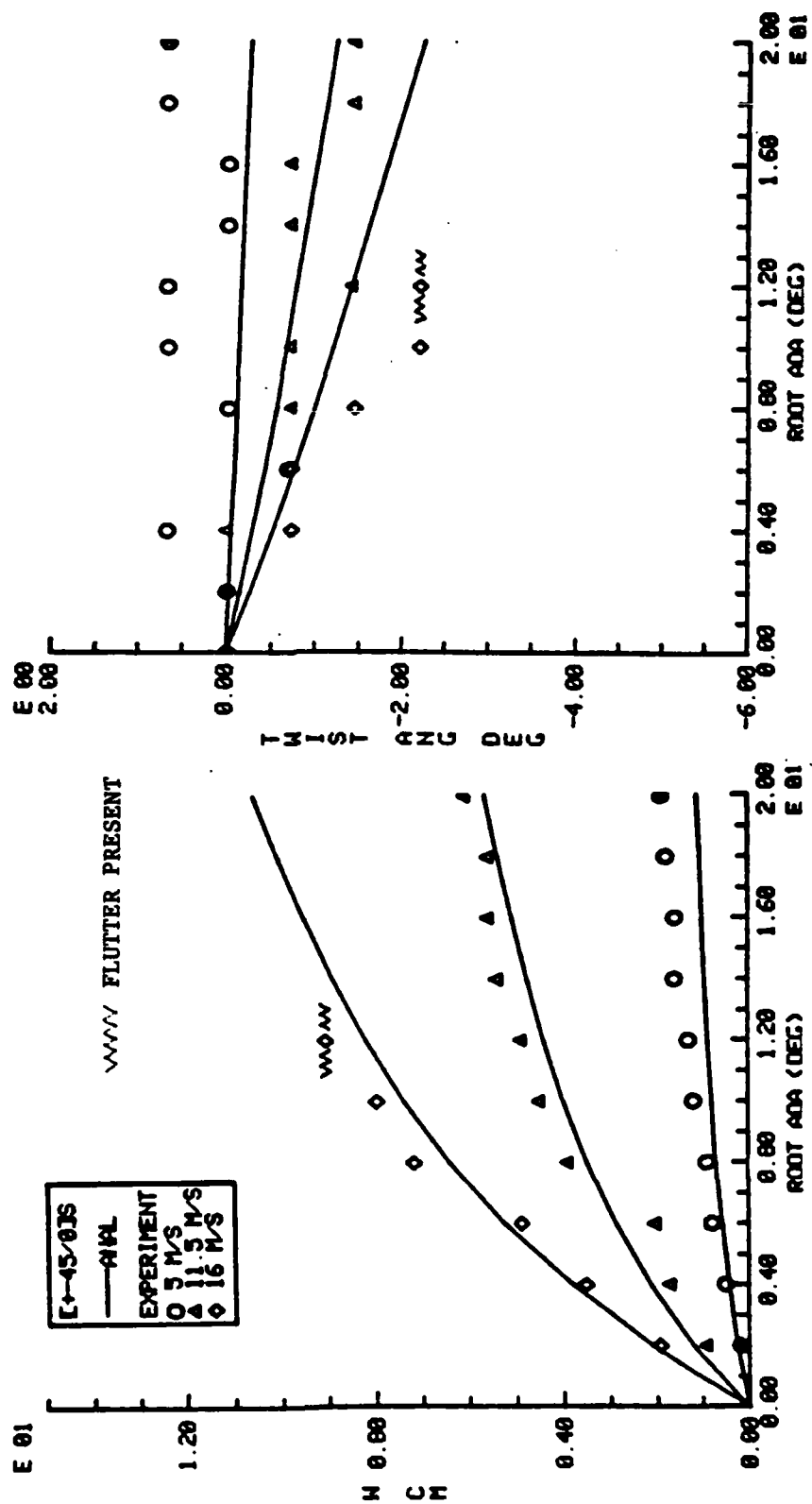


Figure C.11 [±45/0]s layup wing, steady airload deflection.

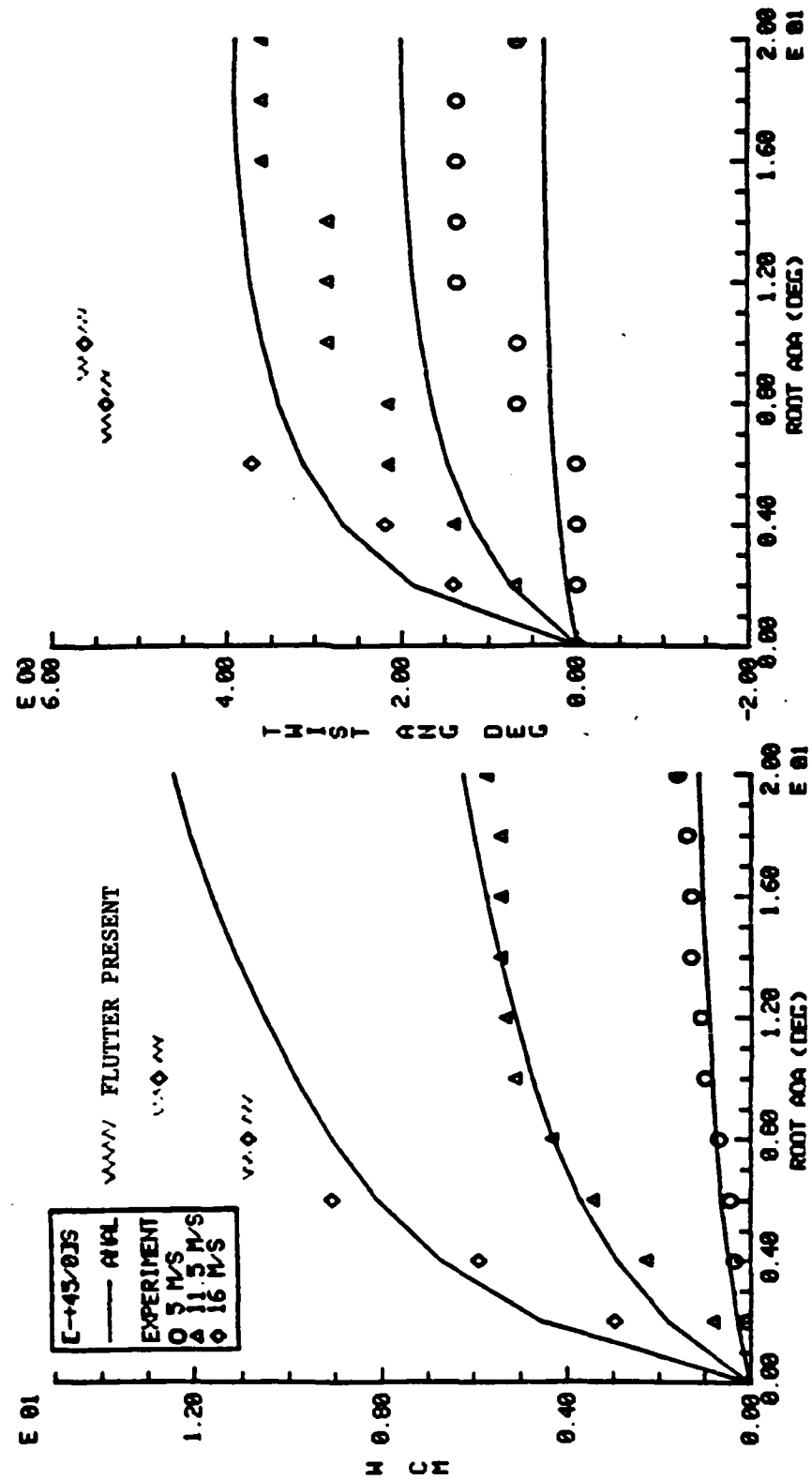


Figure C.12 [745/0]s layout wing, steady airload deflection.

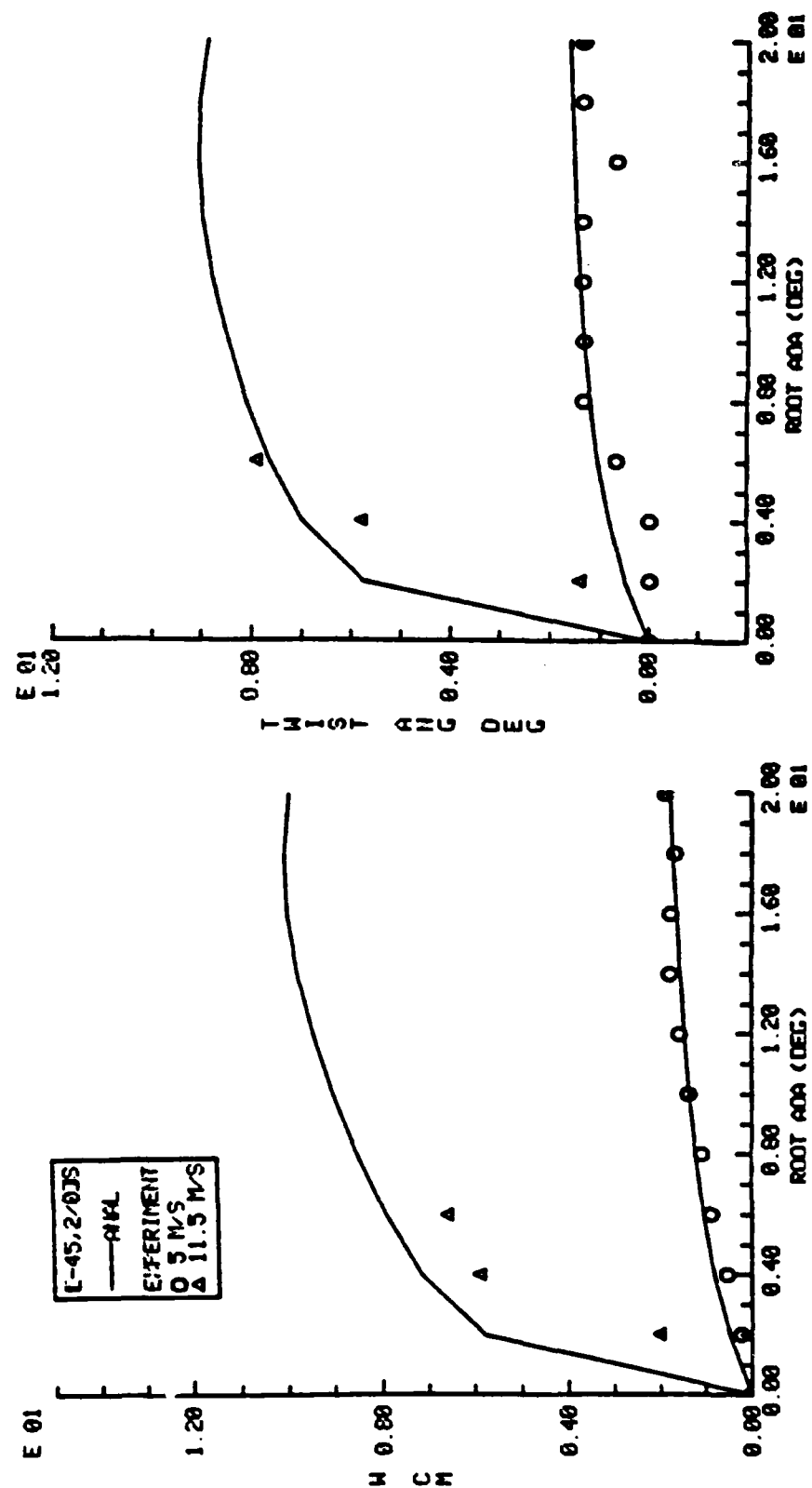


Figure C.13 [-45₂/0]s layout wing, steady airload deflection.

APPENDIX D

FLUTTER

INVESTIGATION RESULTS

Table D.1

FLUTTER DATA UNSWEPT WING ($\Lambda = 0$) (w and θ are at the wing tip)

WING	V (m/s)	α_r (deg)	w_{avg} (cm)	Δw (cm)	θ_{avg} (deg)	$\Delta \theta$ (deg)	ω (hz)
[02/90]s	26	1	0.5	0.7	1.0	10.3	33
	13	10	2.4	0	3.5	9.8	40
[+15 ₂ /0]s	25	1	0.2	0.2	0.7	8.1	32
	24	10	5.1	0.2	-4.0	19.3	37
[±15/0]s	28	3	4.0	0.8	-0.7	8.5	37
	16	10	3.8	0	0.4	5.0	49
[∓15/0]s	21	1	4.3	0.5	4.8	14	43
	10	10	2.2	0.1	2.8	7.0	43
[-15 ₂ /0]s	18	1	4.7	9.4	10.1	17.4	5.8
	13	10	3.3	11.7	7.9	28.4	7.6
[+30 ₂ /0]s	29	0	-0.6	1.7	2.4	12	60
	28	12	7.9	4.0	-4.8	35	61
[±30/0]s	27	10	11.7	1.2	-3.7	12	46
[∓30/0]s	24	1	13.5	1.3	13.5	8.8	40
	15	10	8.4	0.2	5.6	6.7	52

Table D.1 (continued)

FLUTTER DATA UNSWEPT WING ($\Lambda = 0$) (w and θ are at the wing tip)

WING	V	α_r	w_{avg}	Δw	θ_{avg}	$\Delta \theta$	ω
	(m/s)	(deg)	(cm)	(cm)	(deg)	(deg)	(hz)
[-30 ₂ /0]s	15	1	5.1	17.2	3.9	16	2.6
	8	10	3.0	4.5	4.9	5.8	4.9
[+45 ₂ /0]s	27	1	2.1	3.6	2.2	23	25
	23	10	9.9	2.7	-2.7	20	26
[±45/0]s	25	8	13.1	0.4	-2.4	3.2	44
	18	10	10.8	0.6	-4.2	6.8	49
[745/0]s	22	1	16.0	0.9	9.0	1.5	40
	14	10	12.2	0.1	6.3	6.3	55
[-45 ₂ /0]s	14	1	10.9	12	10	14	3.5
	9	10	5.2	10.3	5.2	9.1	4.2

Table D.2

FLUTTER DATA FORWARD SWEPT WING ($\Lambda = -30$) (w and θ are at the wing tip)

WING	V (m/s)	α_r (deg)	w_{avg} (cm)	Δw (cm)	θ_{avg} (deg)	$\Delta \theta$ (deg)	ω (hz)
[0 ₂ /90]s	20	1	8.8	0	6.1	1.5	40
	18	10	8.3	11.0	1.5	3.0	8
[+15 ₂ /0]s	21	10	12.2	1.1	-10.7	16.7	40
[±15/0]s	25	1	7.8	0	-1.6	27	44
	18	10	8	0	-0.4	14.3	50
[∓15/0]s	19	1	6.2	11.9	4.8	9.5	4.7
	15	10	5.2	12.8	4.7	9.3	7.5
[-15 ₂ /0]s	15	1	3.2	15	8.3	23.4	4.0
	12	10	3.9	12.9	7.7	18.1	6.8
[+30 ₂ /0]s	21	10	14.5	0.8	-18	12	59
[±30/0]s	22	1	19.8	0.7	-6	44	33
	20	10	21.5	1	-7	42	31
[∓30/0]s	17	1	6.9	19.7	4.0	12	3
	13	10	7.5	9.5	2.5	5	5.6

Table D.2 (continued)

FLUTTER DATA FORWARD SWEPT WING ($\Lambda = -30$) (w and θ are at the wing tip)

WING	V (m/s)	α_r (deg)	w avg (cm)	Δw (cm)	θ avg (deg)	$\Delta \theta$ (deg)	ω (hz)
[-30/0]s	11	1	4.1	18.1	7.0	22	2.7
	8	10	3.7	10.9	3.5	17	4.6
[+45 ₂ /0]s	20	1	16.9	0.2	6.9	25	42
	15	10	16.9	0.7	14.5	19.1	44
[±45/0]s	20	1	19.5	3.0	-10.5	11	5.7
	14	10	12.9	6.3	3.5	21	4.8
[∓45/0]s	14	2	9.5	19	5.5	11	2.8
	11	10	9	14	1.5	1	4.3
[-45 ₂ /0]s	10	1	7.1	8.6	8.4	14.7	2
	8	10	6.9	11.6	7.5	15	3.5

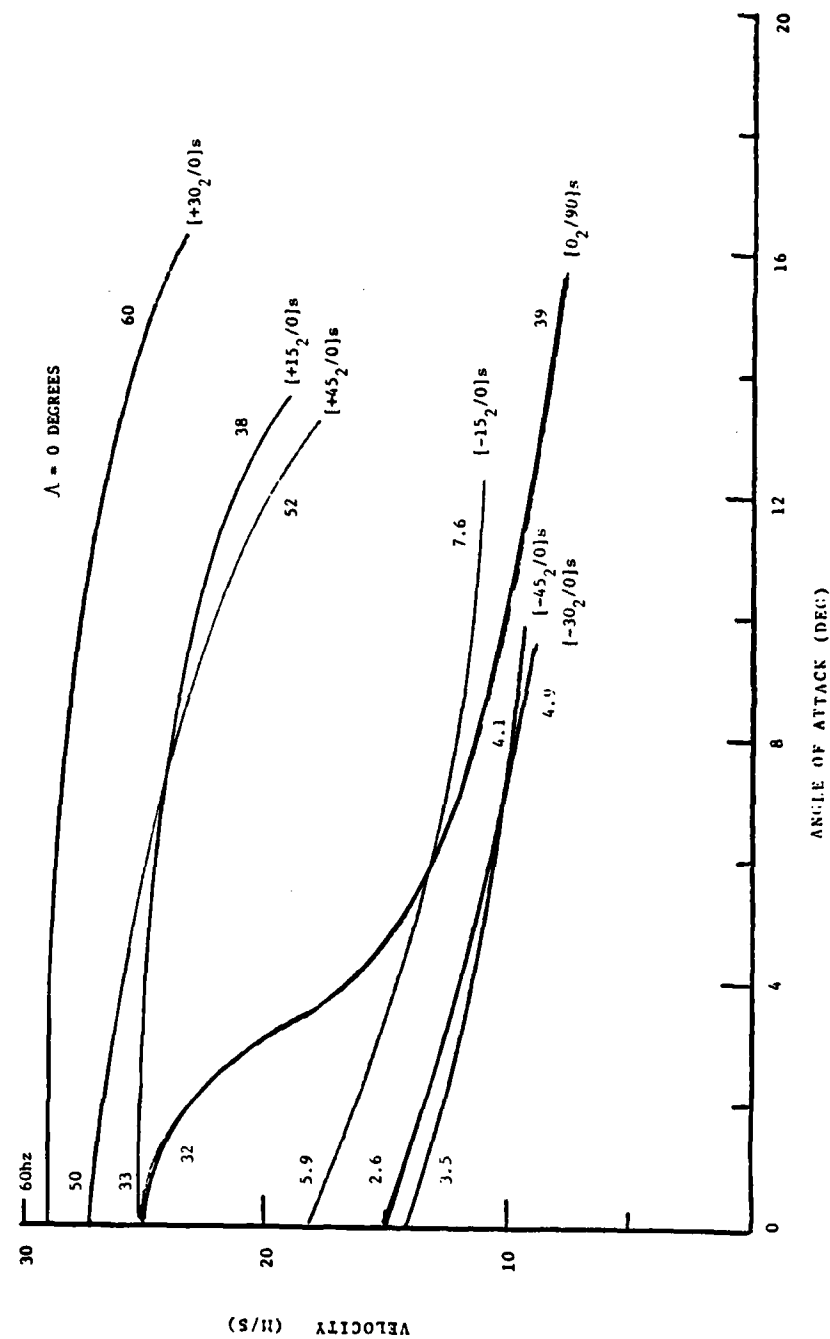


Figure D.1 $\Lambda=0$, crosssection of test wings, flutter boundary curves.

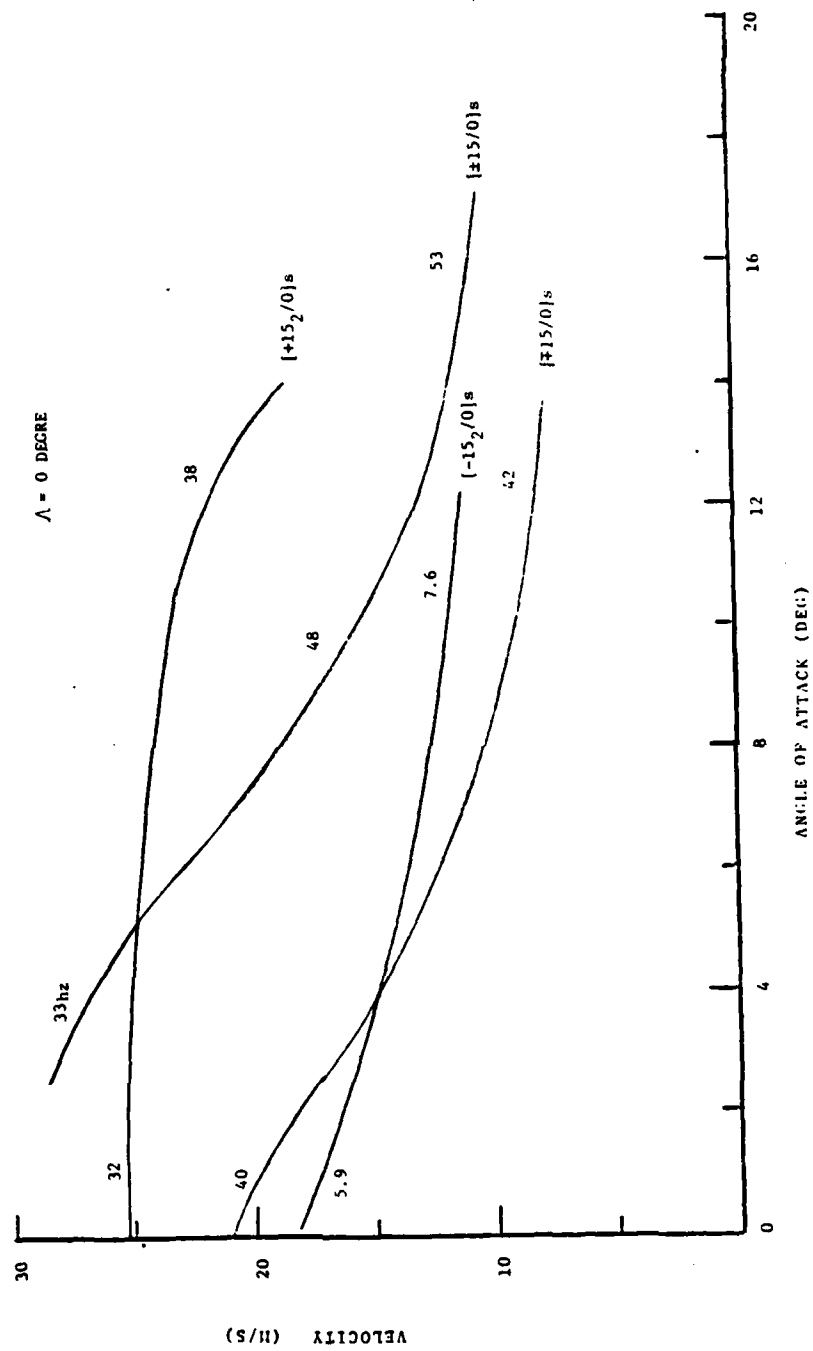


Figure D.2 $\Lambda=0$, 15 degree ply fiber angle layup wings, flutter boundary curves.

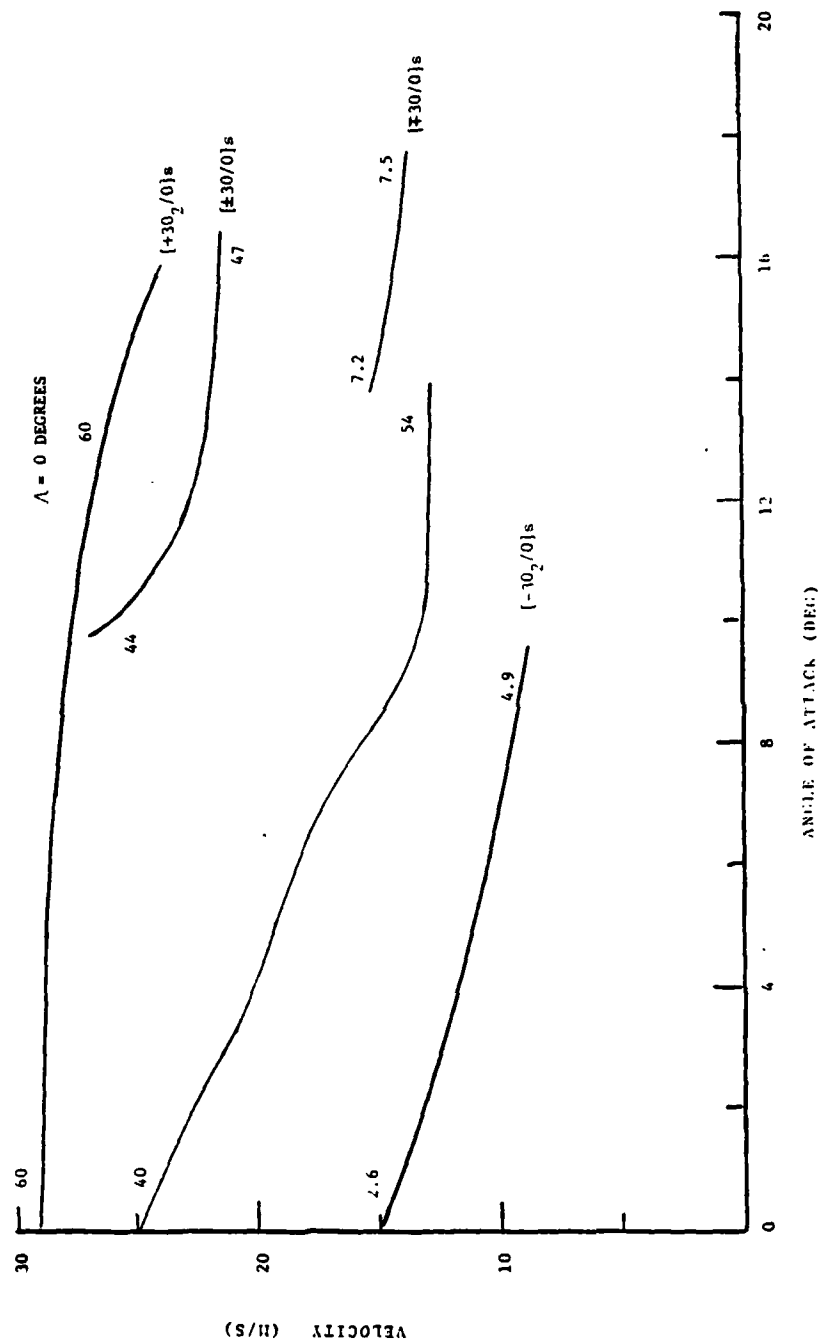


Figure D.3 $\Lambda=0$, 30 degree ply fiber angle layup wings, flutter boundary curves.

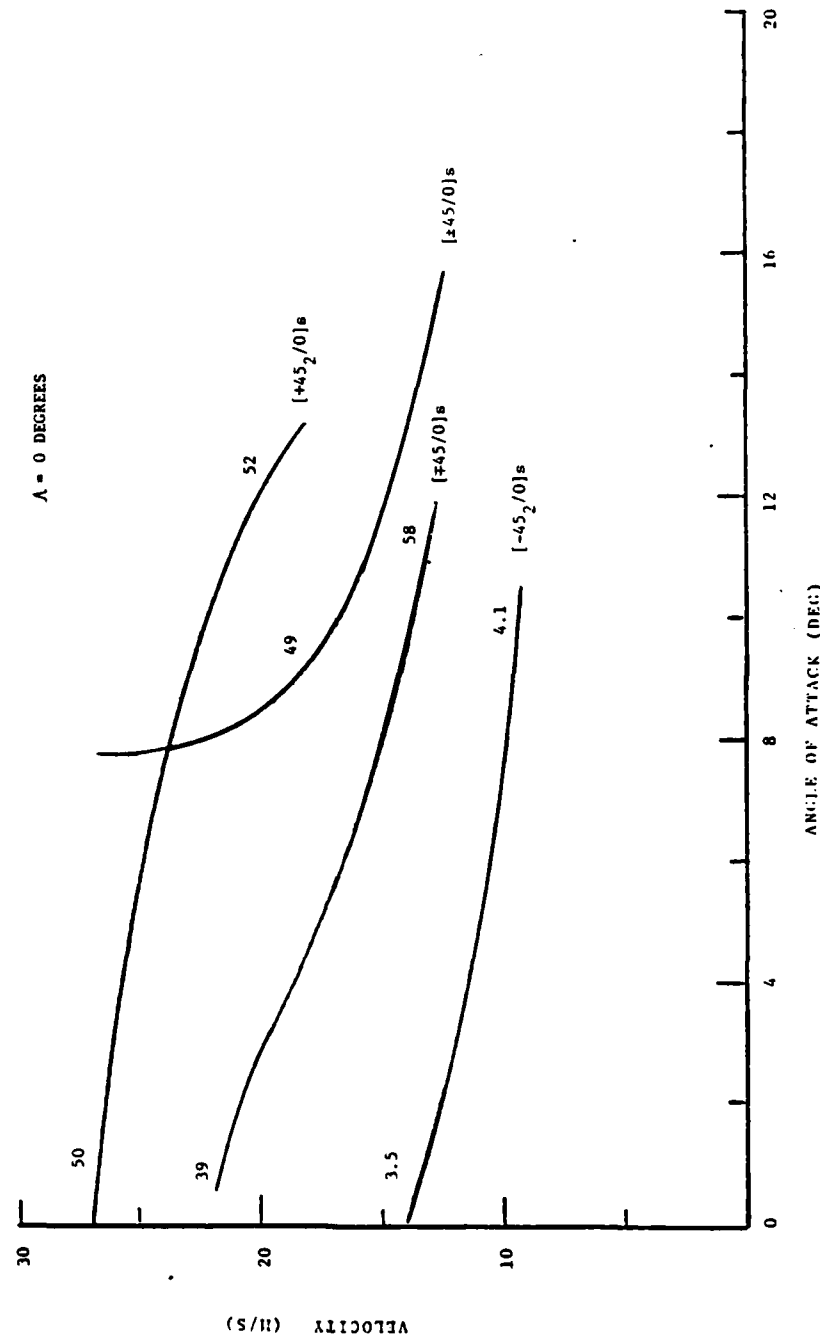


Figure D.4 $\Lambda=0$, 45 degree ply fiber angle layup wings, flutter boundary curves.

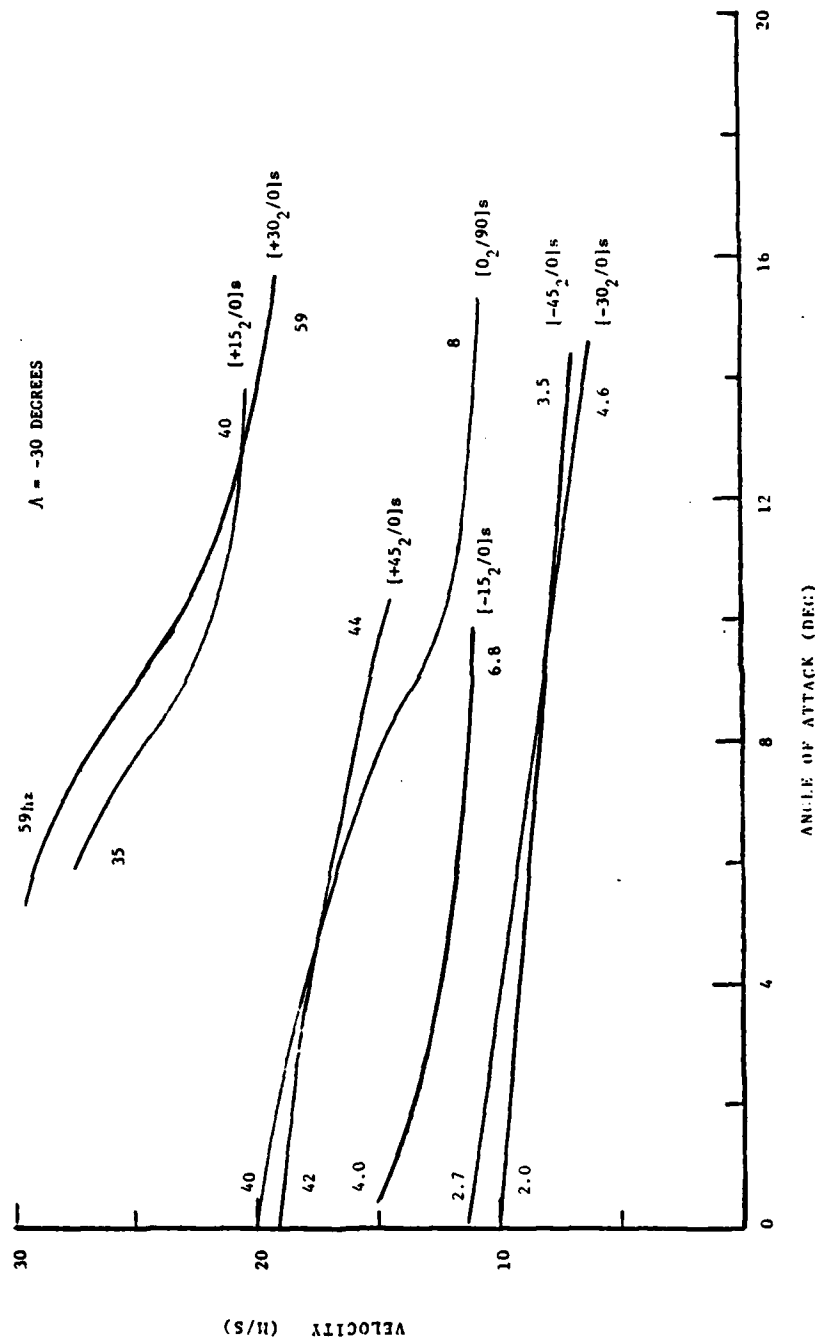


Figure D.5 $\Lambda = -30$, crosssection of test wings, flutter boundary curves.

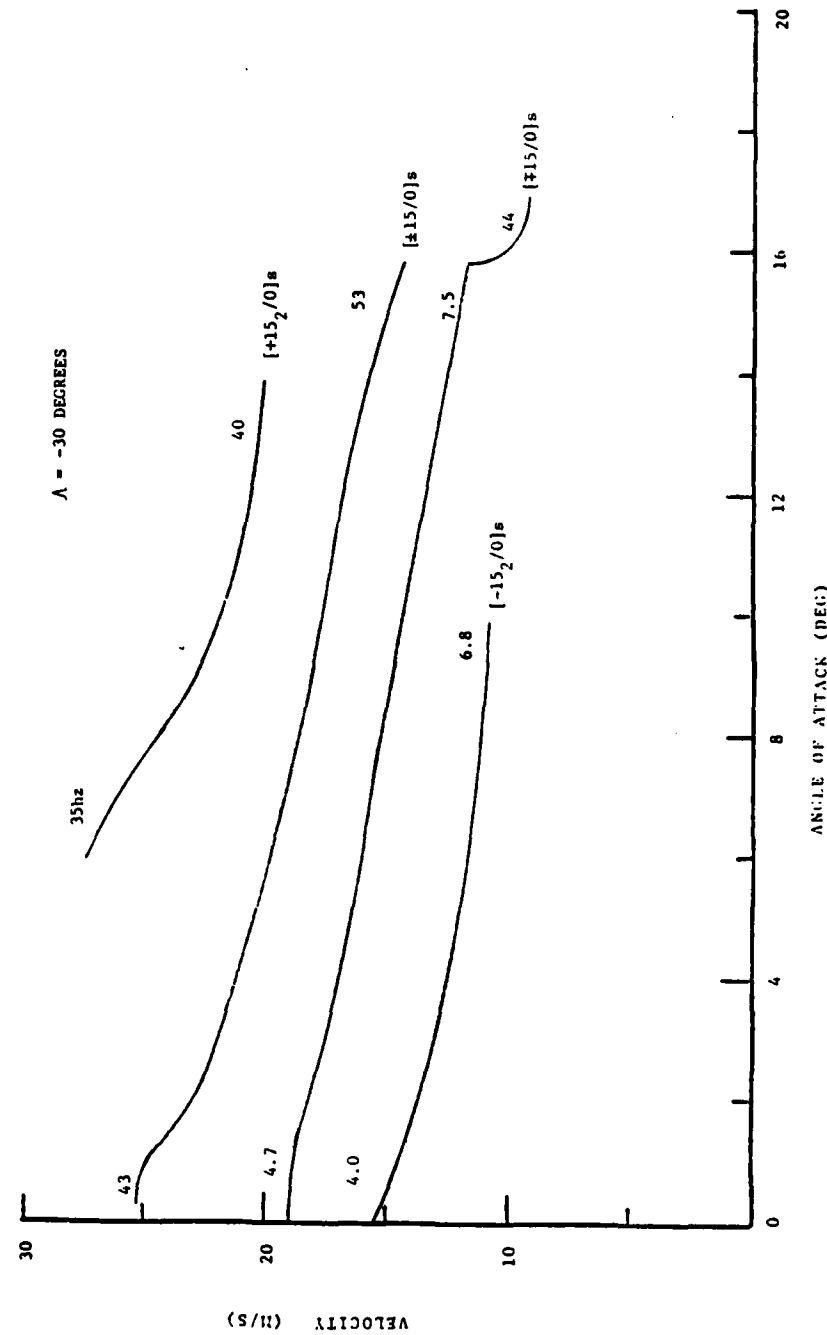


Figure D.6 $\Lambda = -30$, 15 degree ply fiber angle layup wings, flutter boundary curves.

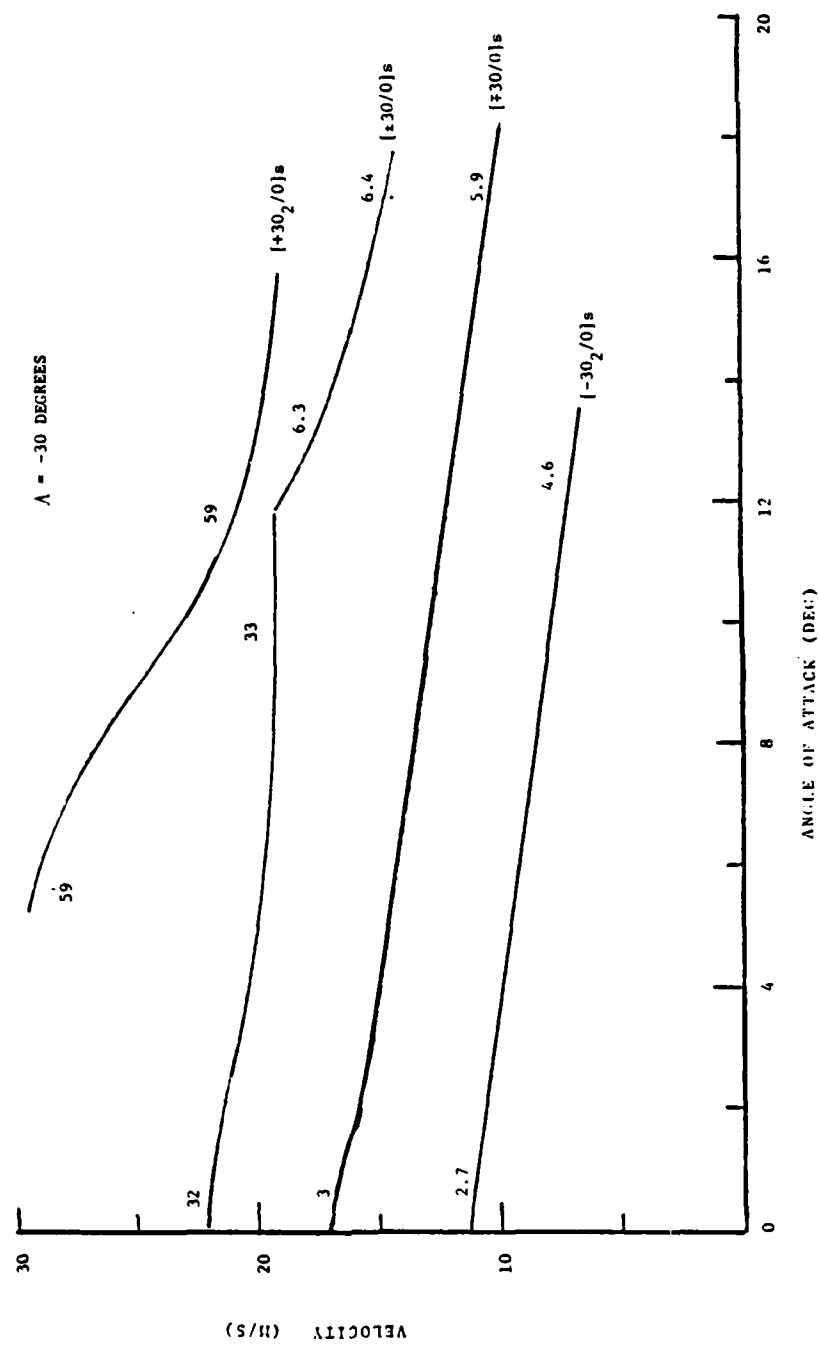


Figure D.7 $\Lambda = -30$, 30 degree ply fiber angle layup wings, flutter boundary curves.

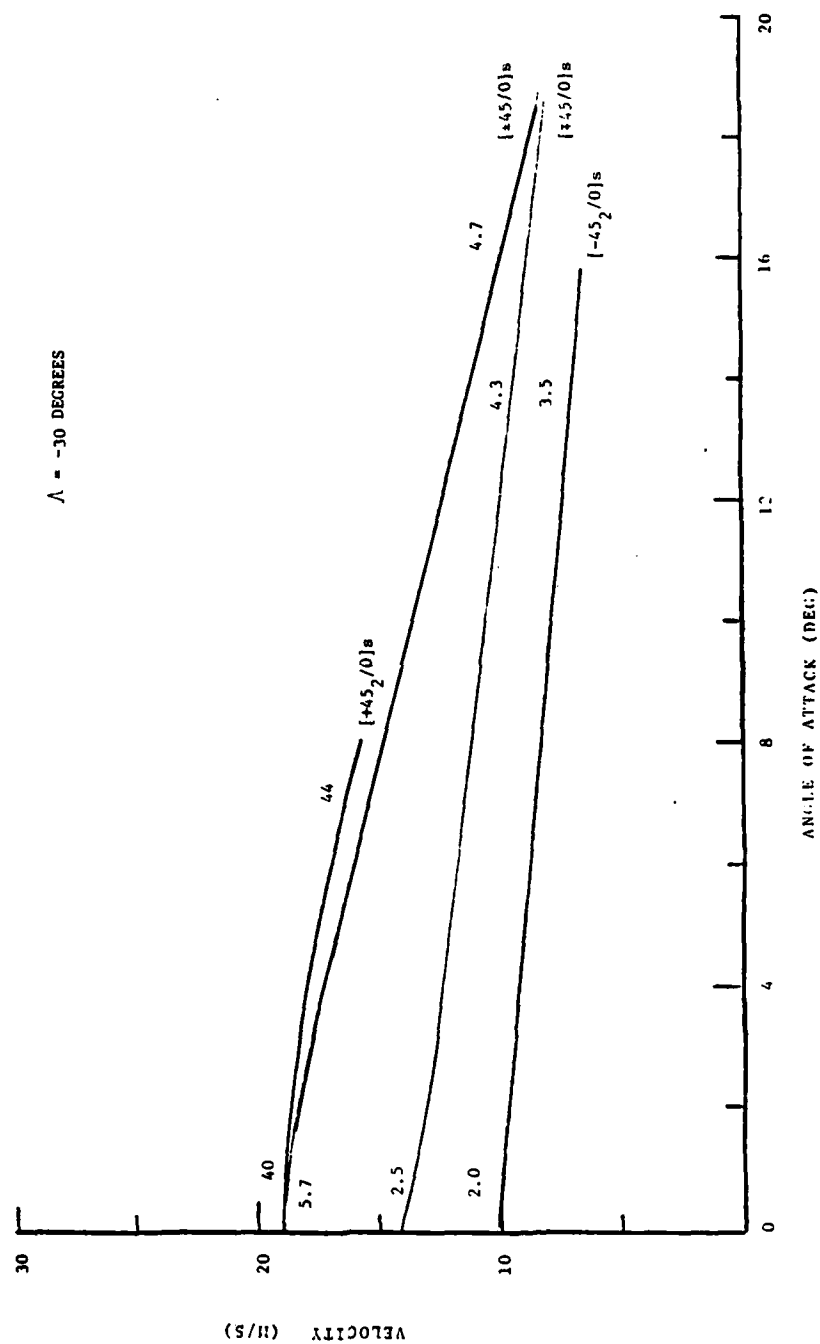


Figure D.8 $\Lambda = -30$, 45 degree ply fiber angle layup wings, flutter boundary curves.

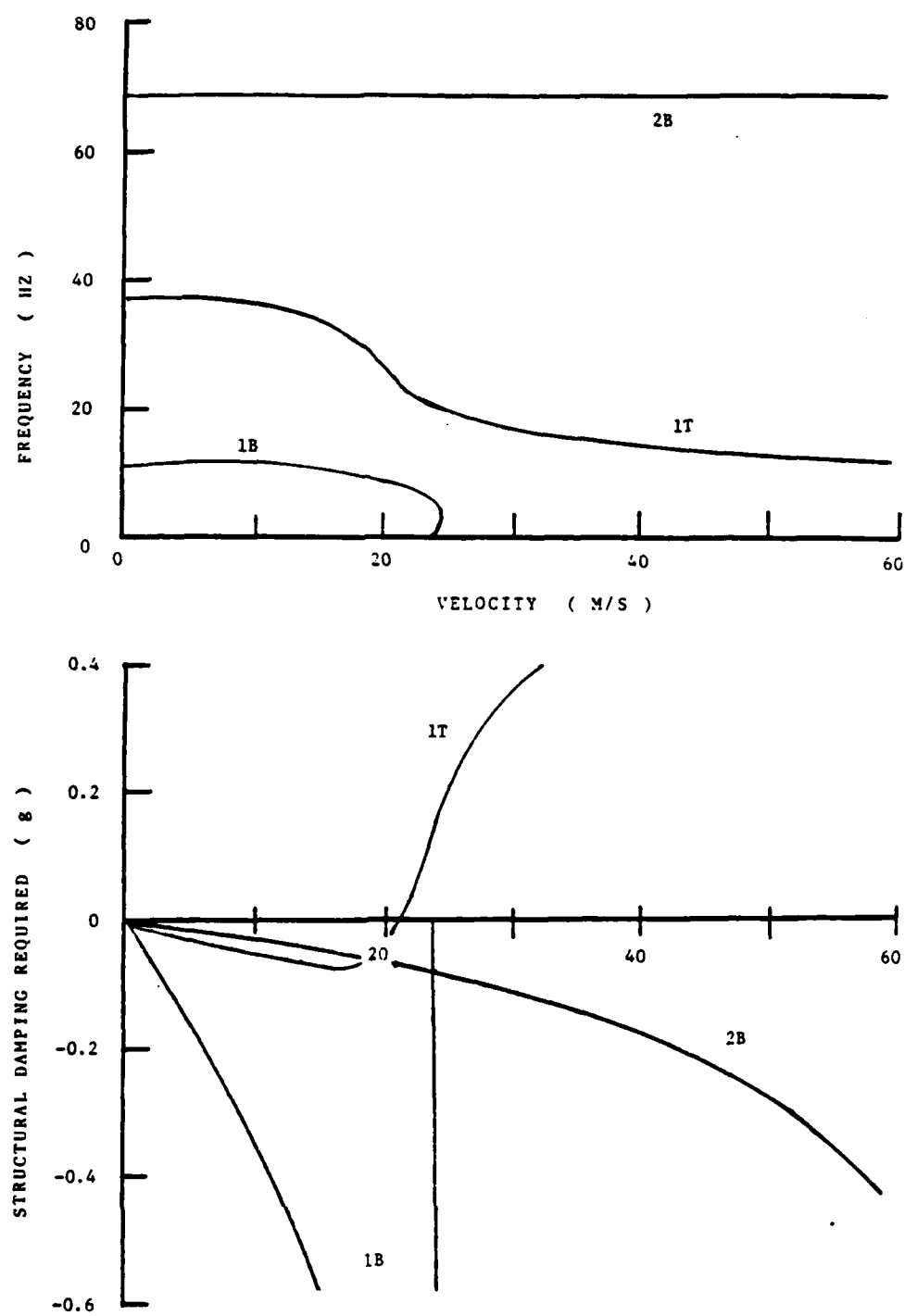


Figure D.9 $\Lambda = 0$, $[0_2/90]_s$ layup wing, V-g diagram.

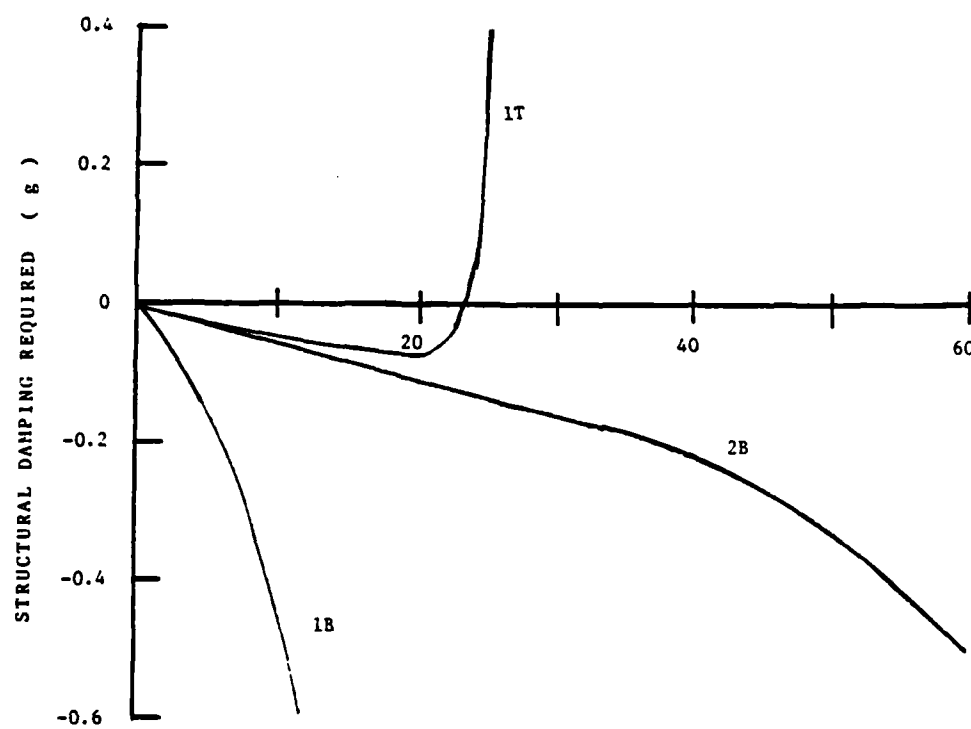
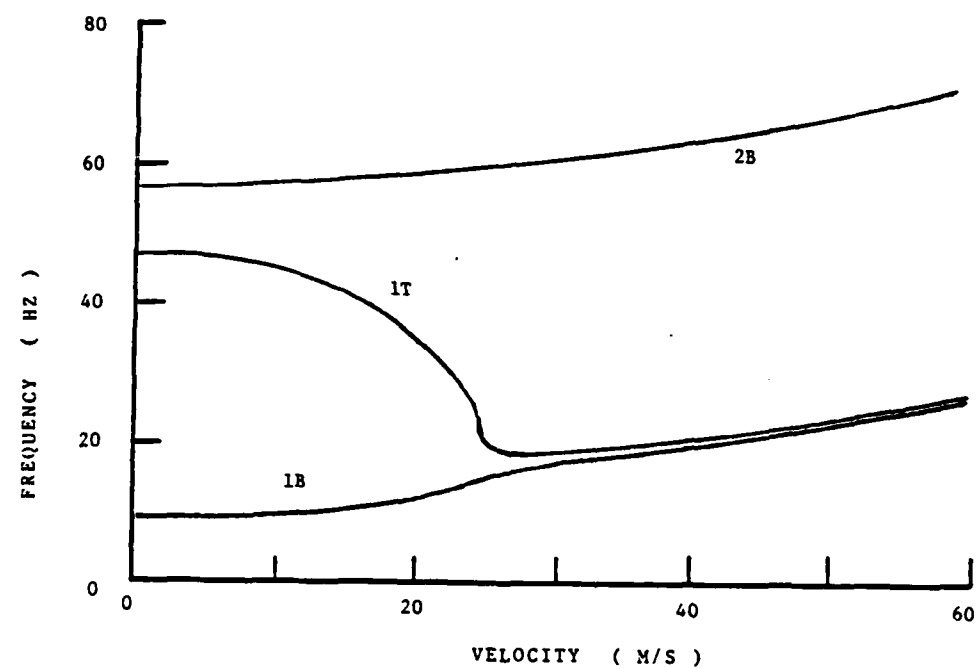


Figure D.10 $\Lambda = 0$, $[+15_2/0]$ s layup wing, V-g diagram.

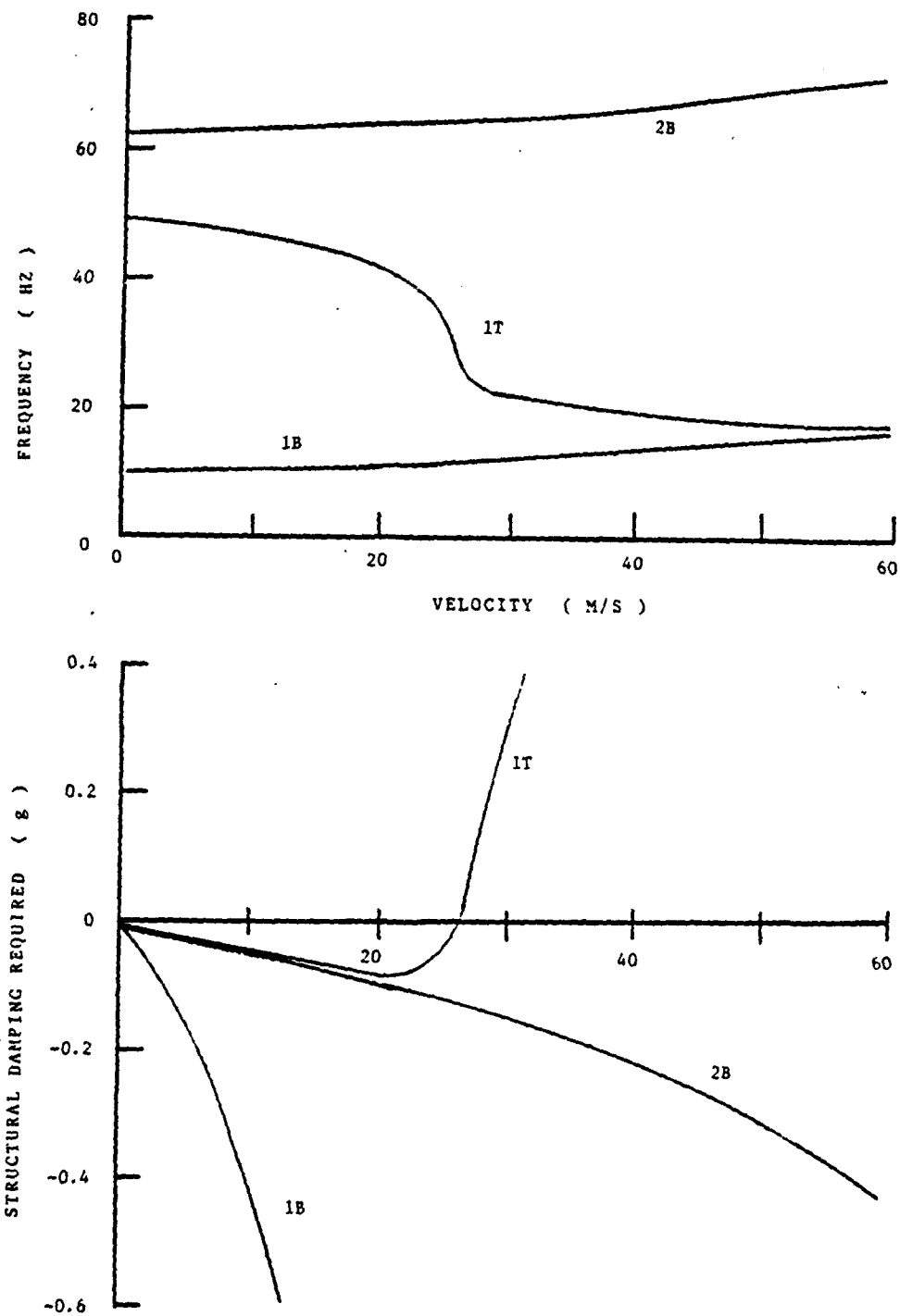


Figure D.11 $\Lambda = 0$, $[\pm 15/0]_s$ layup wing, V-g diagram.

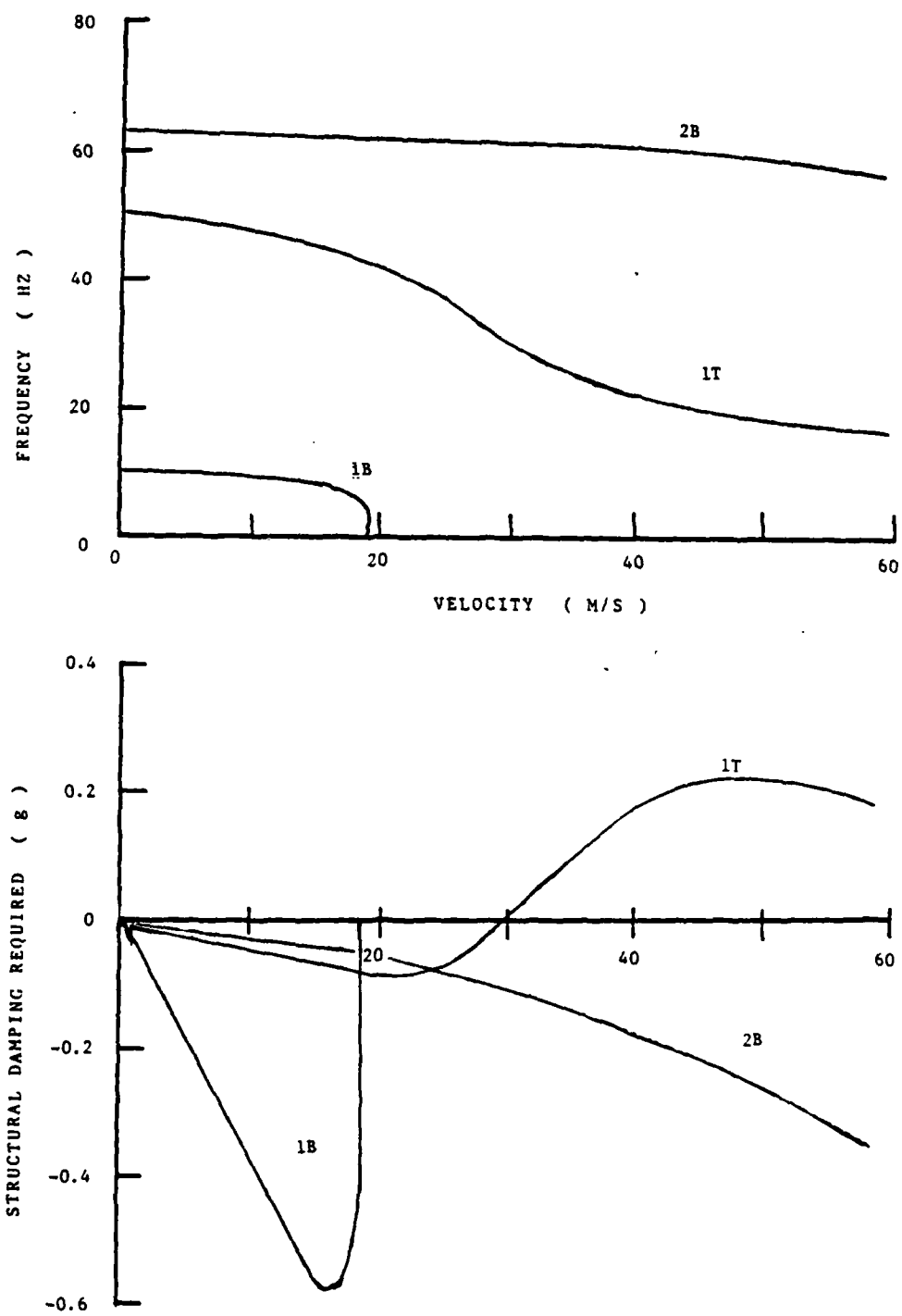


Figure D.12 $\Lambda = 0$, $[\mp 15/0]_s$ layup wing, V-g diagram.

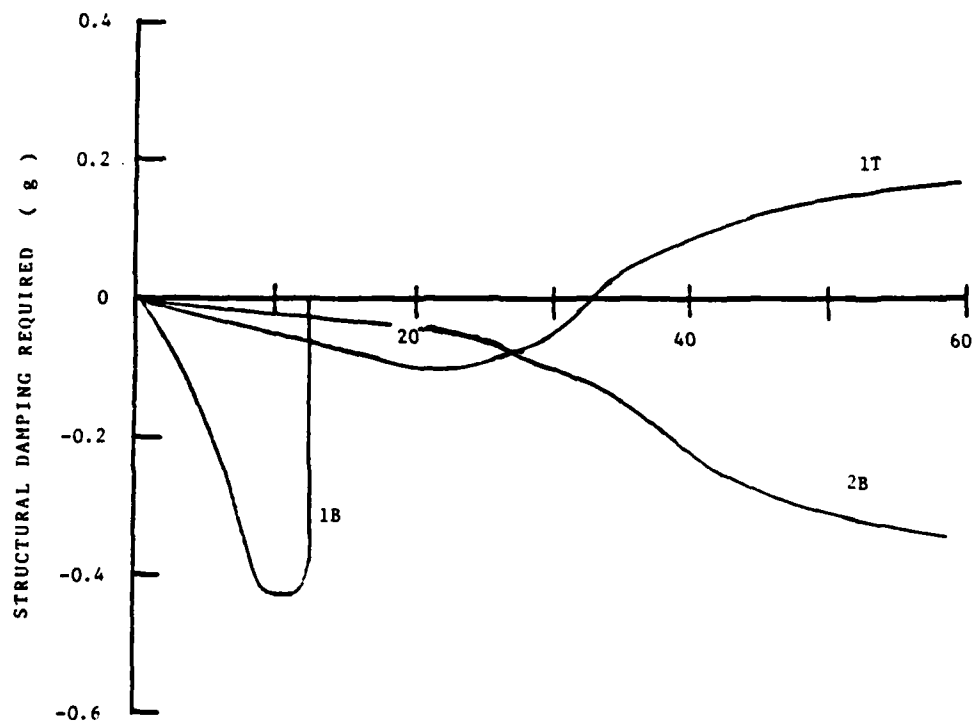
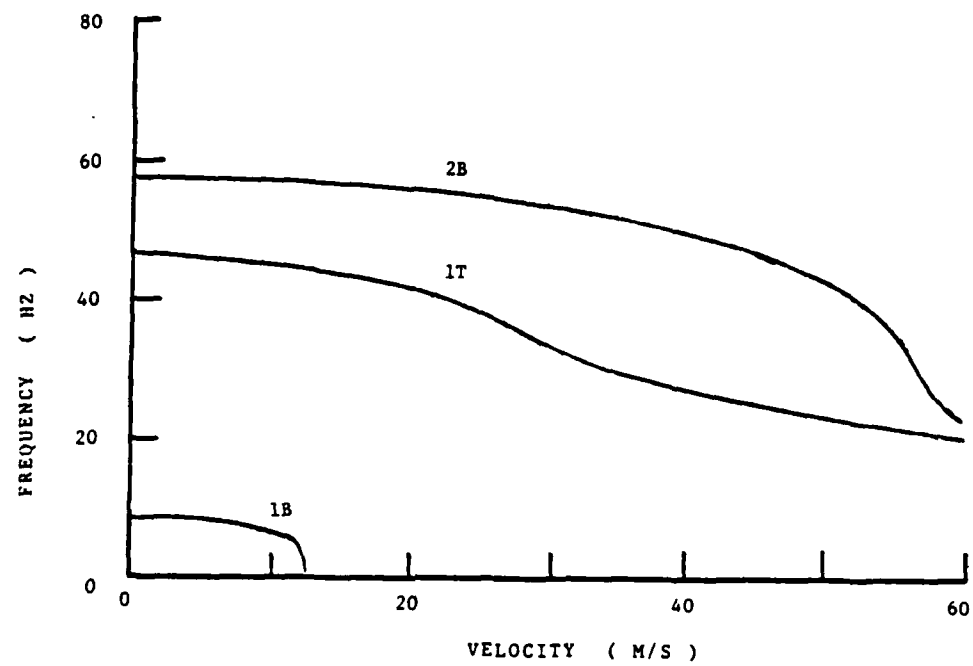


Figure D.13 $\Lambda = 0$, $[-15_2/0]$ s layup wing, V-g diagram.

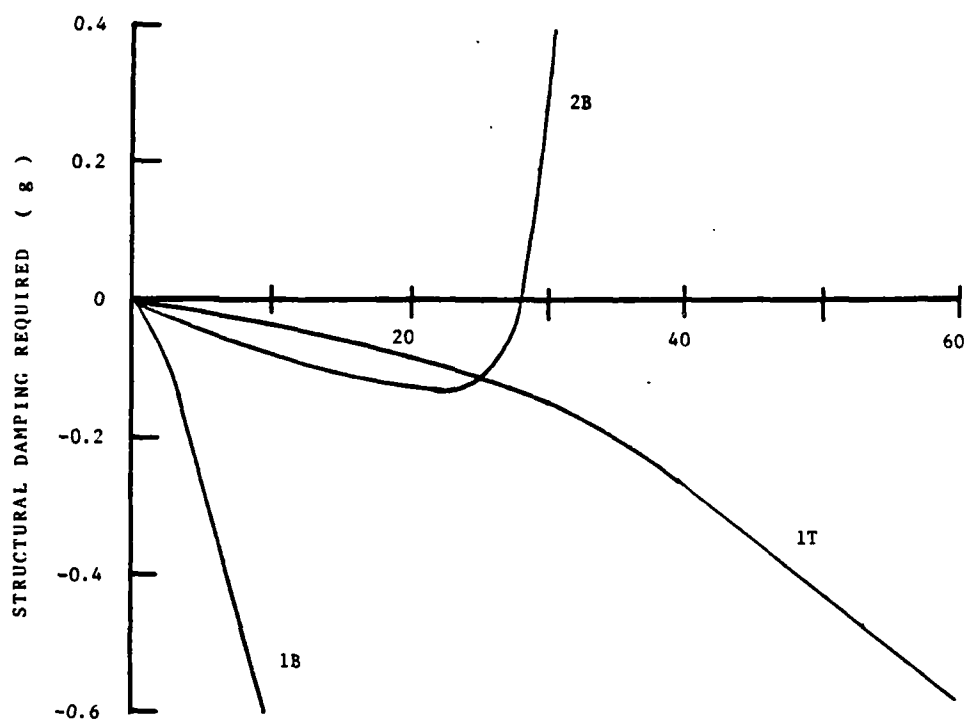
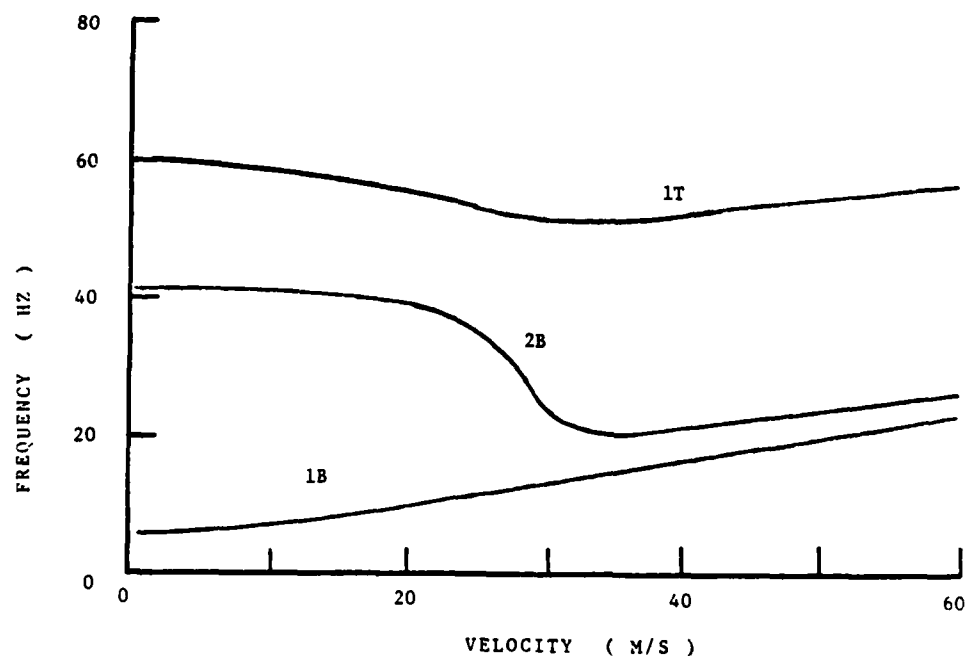


Figure D.14 $\Lambda = 0$, $[+30_2/0]_s$ layup wing, V-g diagram.

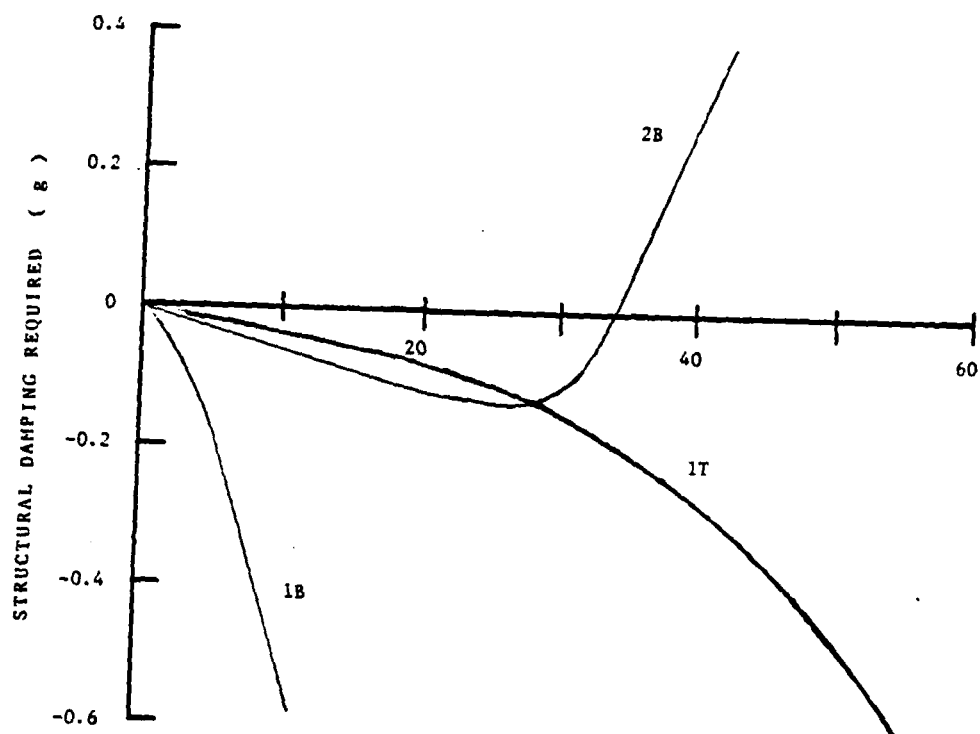
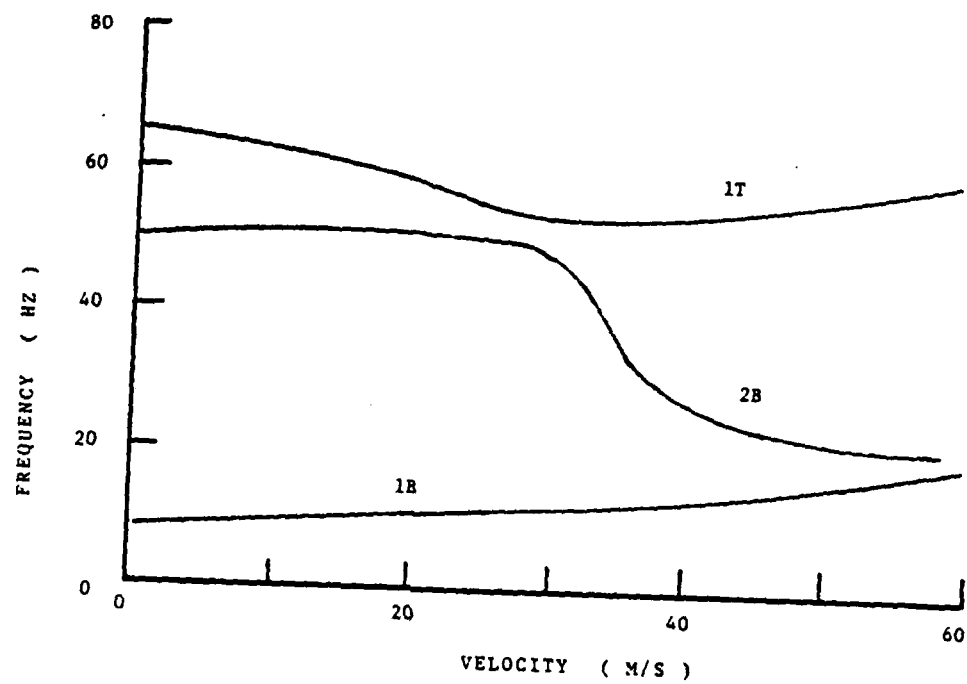


Figure D.15 $\Lambda = 0$, $[\pm 30/0]_s$ layup wing, V-g diagram.

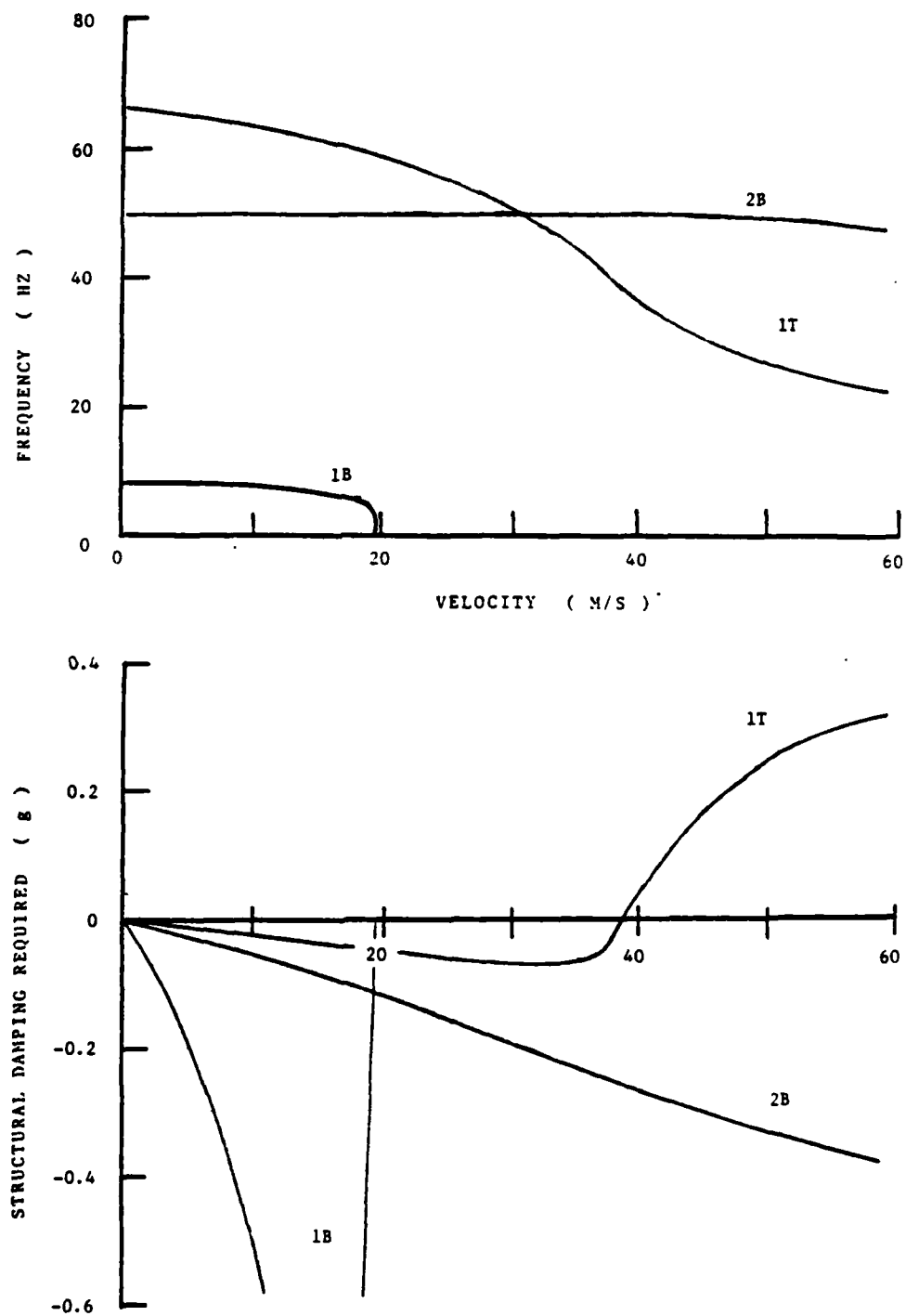


Figure D.16 $\Lambda = 0$, $[\mp 30/0]_s$ layup wing, V-g diagram.

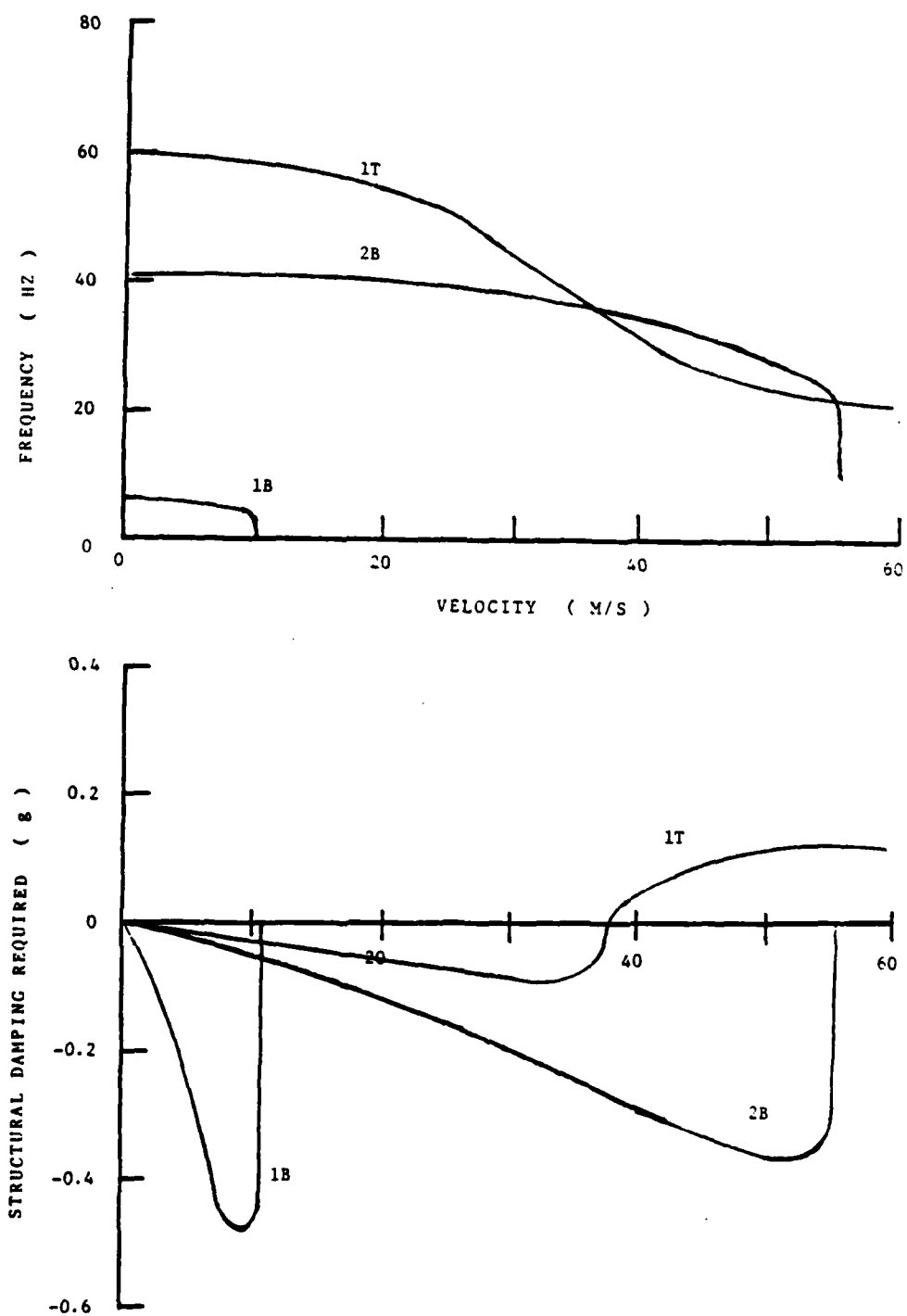


Figure D.17 $\Lambda = 0$, $[-30_2/0]_s$ layup wing, V-g diagram.

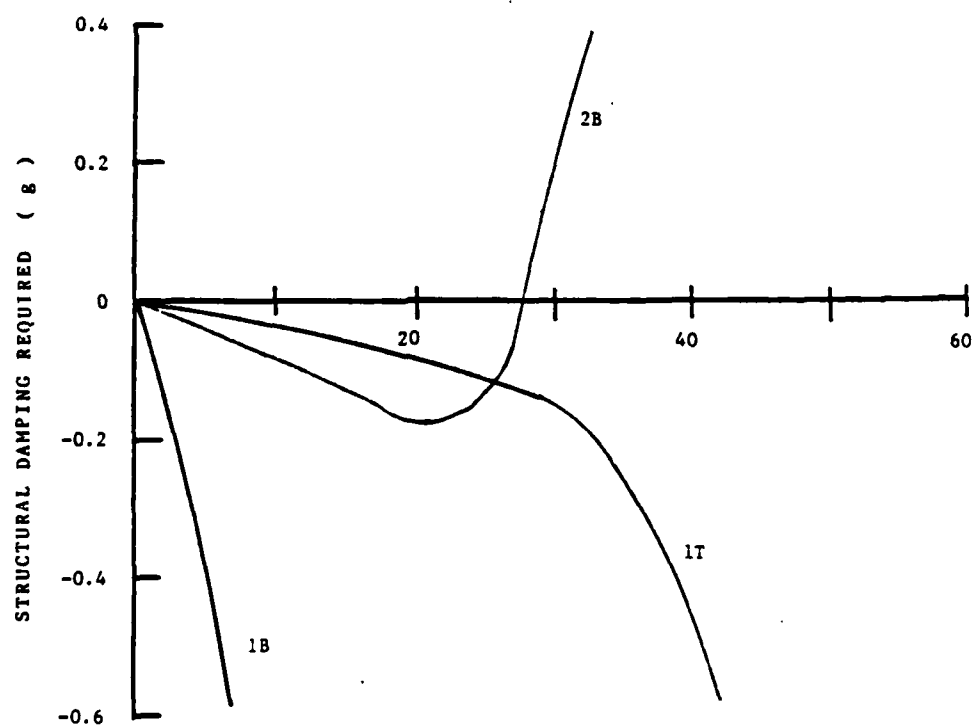
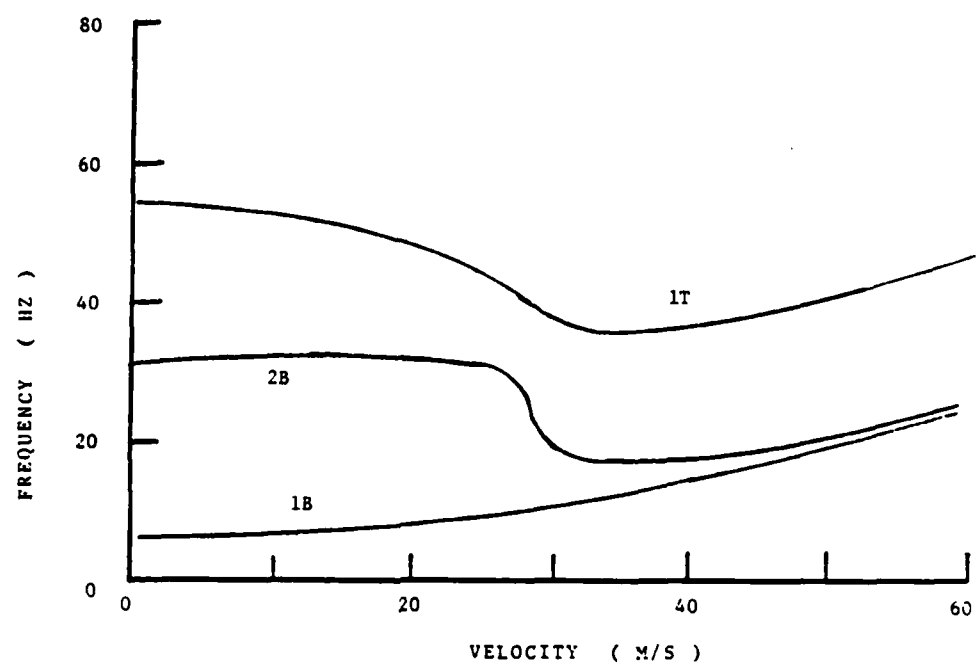


Figure D.18 $\Lambda = 0$, $[+45_2/0]_s$ layup wing, V-g diagram.

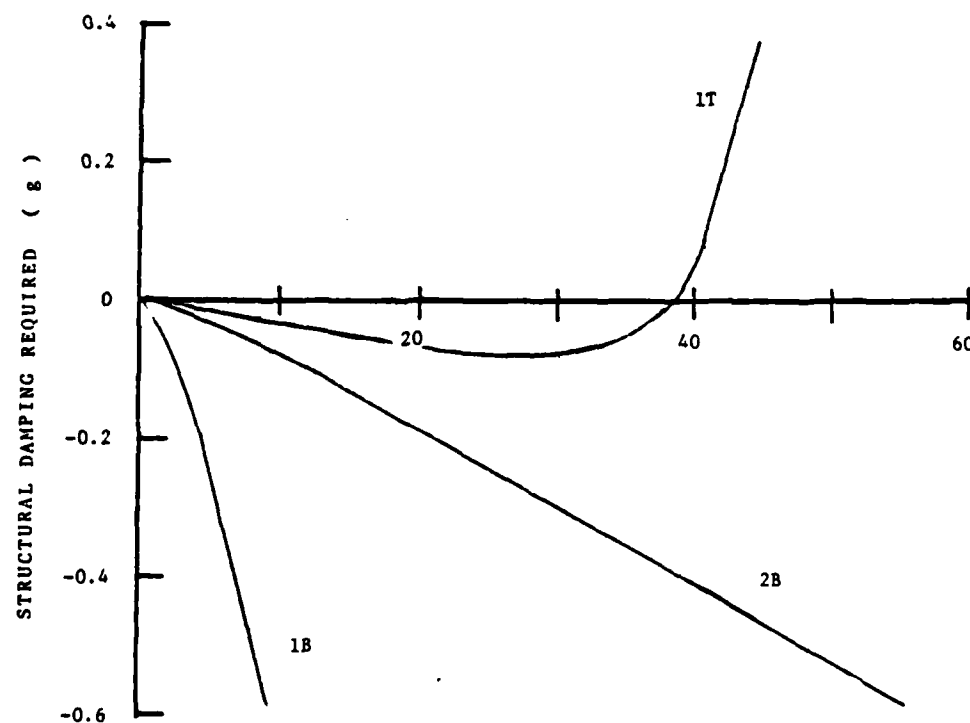
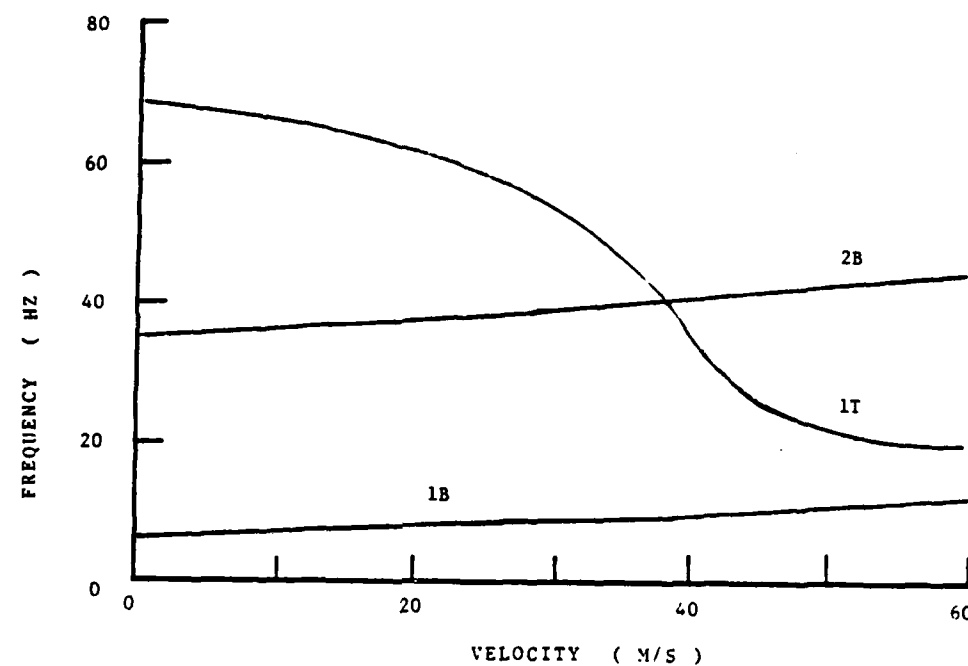


Figure D.19 $\Lambda = 0$, $[\pm 45/0]_s$ layup wing, V-g diagram.

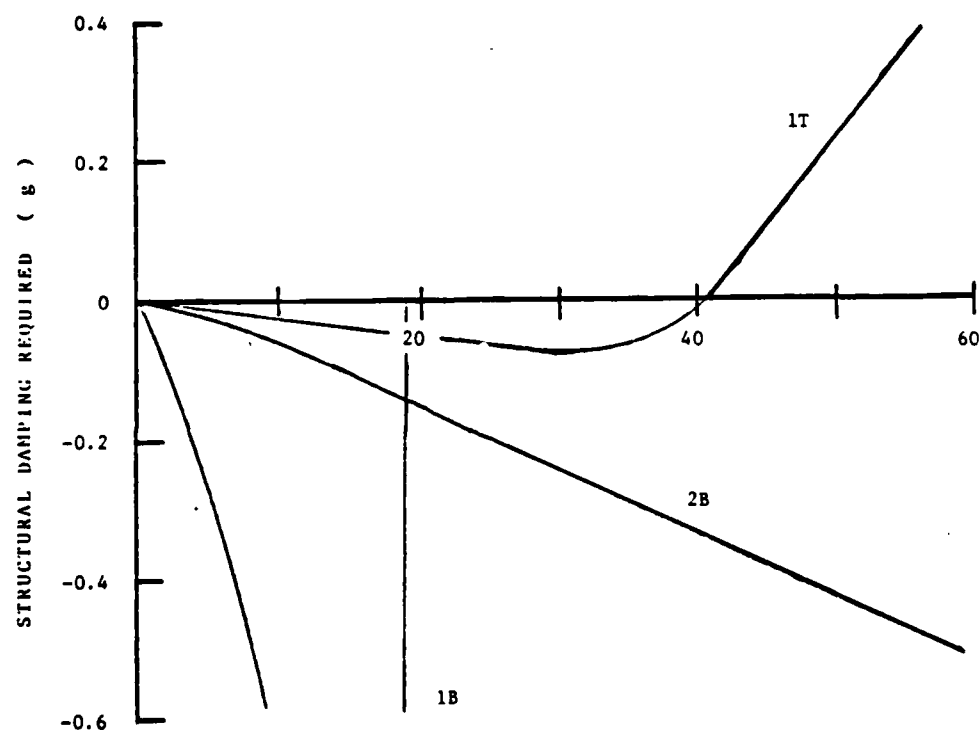
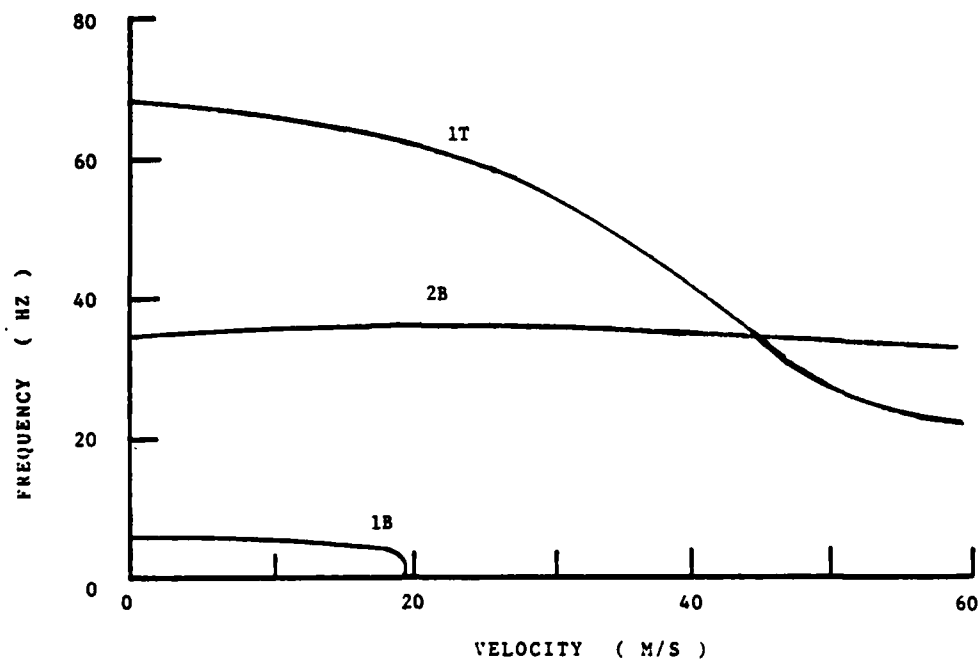


Figure D.20 $\Lambda = 0$, $[\mp 45/0]_s$ layup wing, V-g diagram.

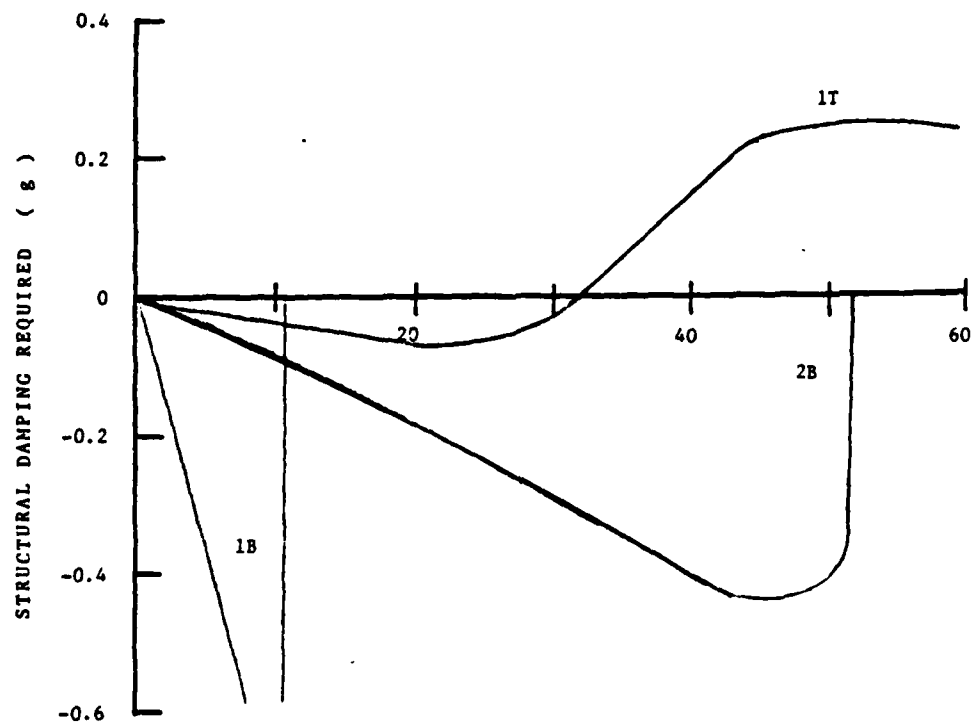
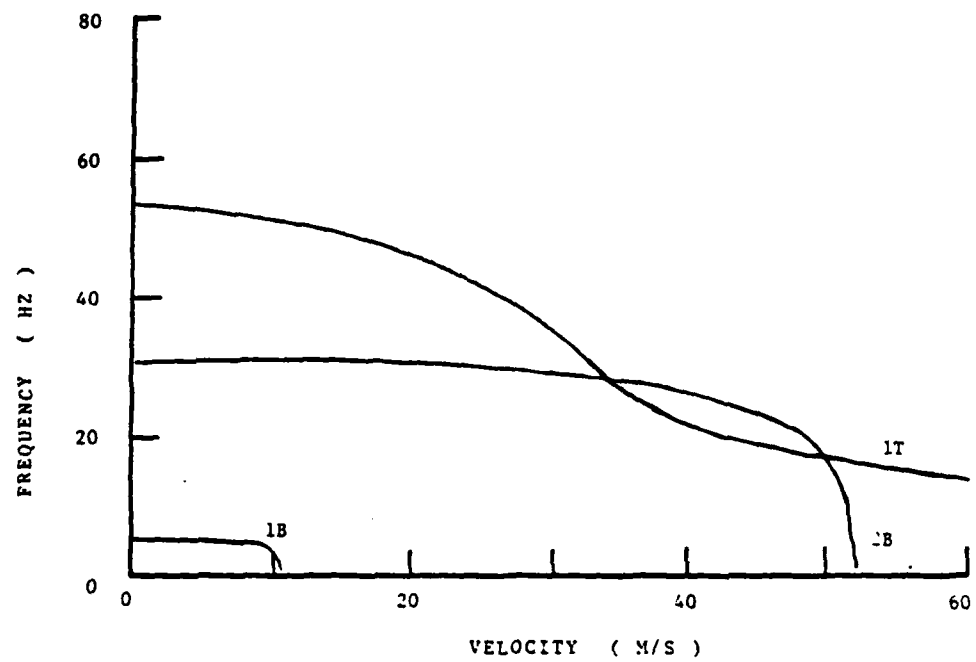


Figure D.21 $\Lambda = 0$, $[-45_2/0]_s$ layup wing, V-g diagram.

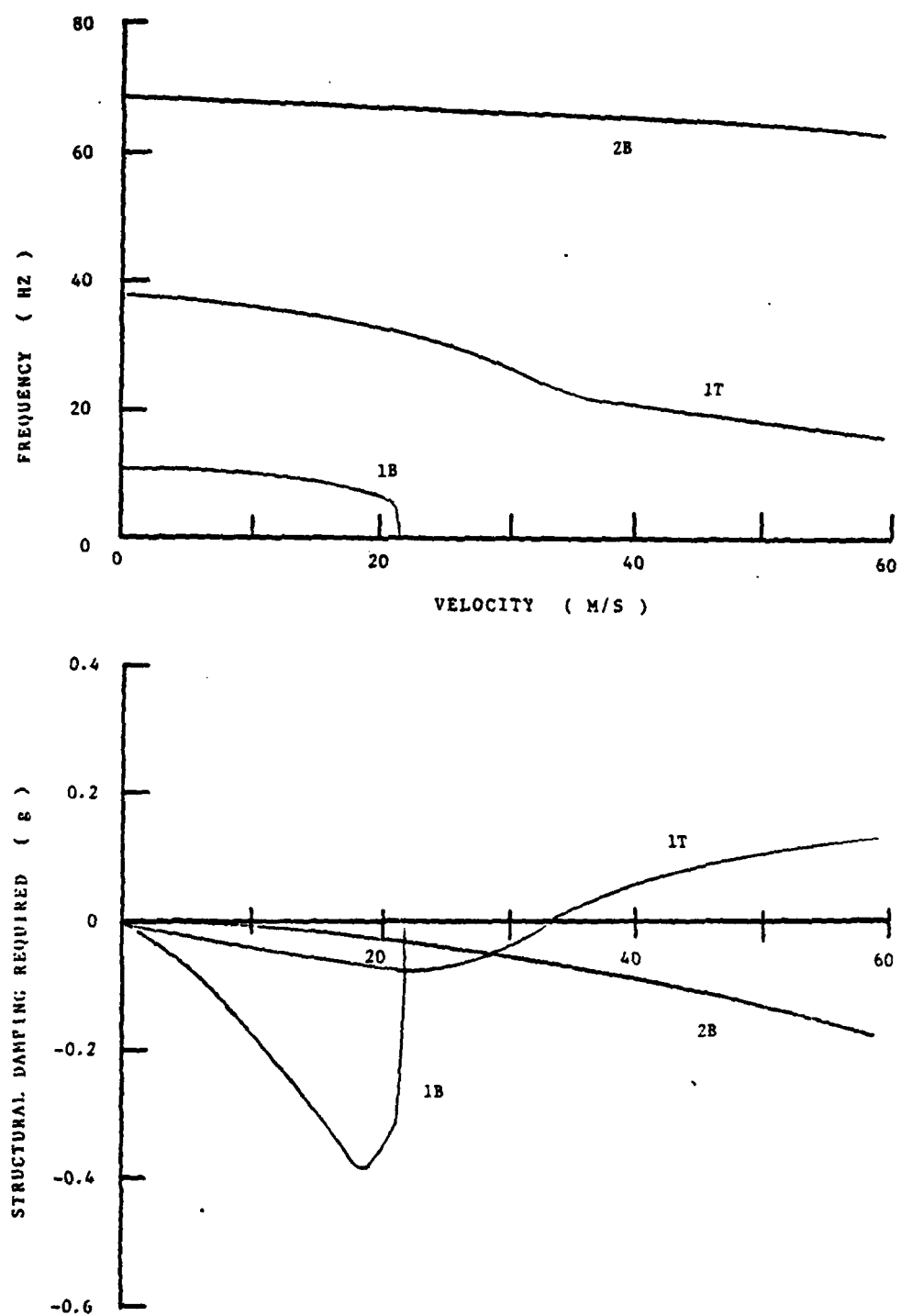


Figure D.22 $\Lambda = -30$, $[0_2/90]_s$ layup wing, V-g diagram.

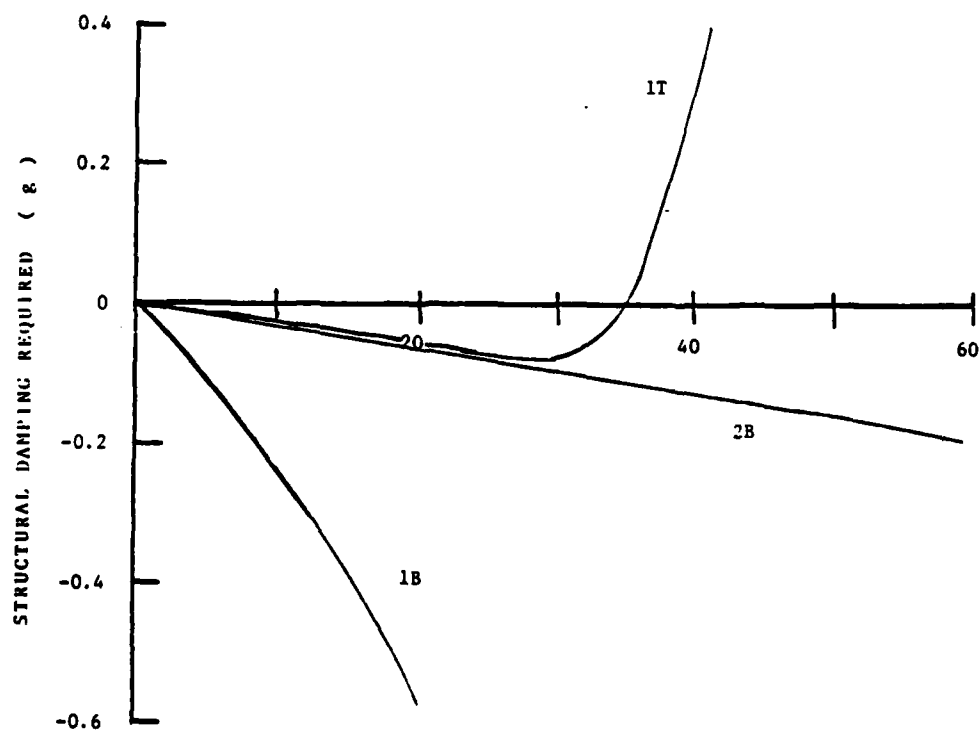
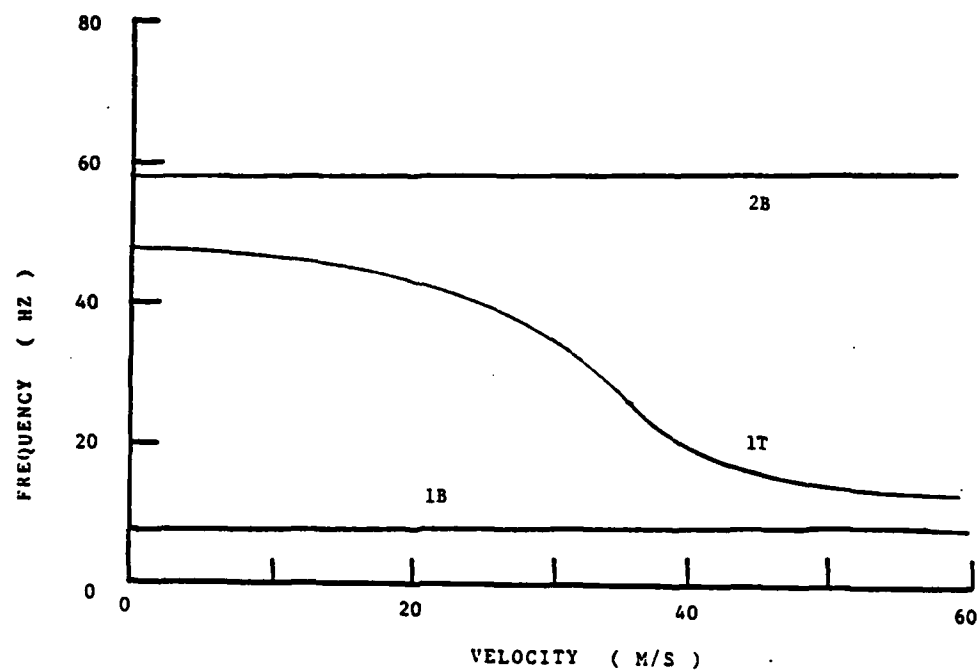


Figure D.23 $\Lambda = -30$, $[+15_2/0]$ s layup wing, V-g diagram.

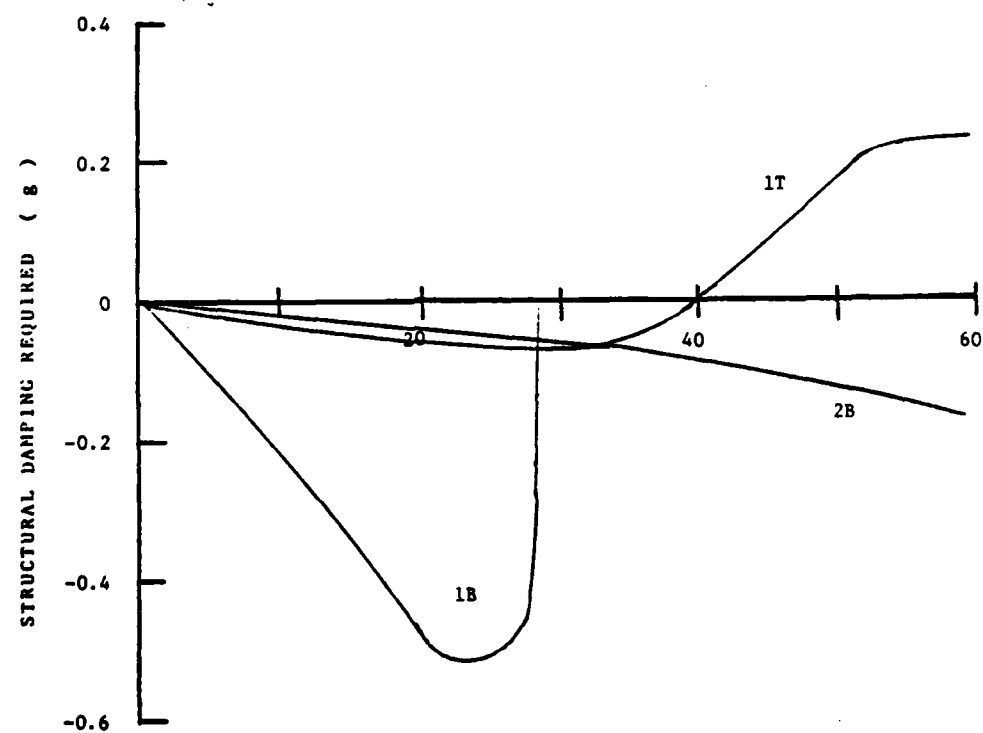
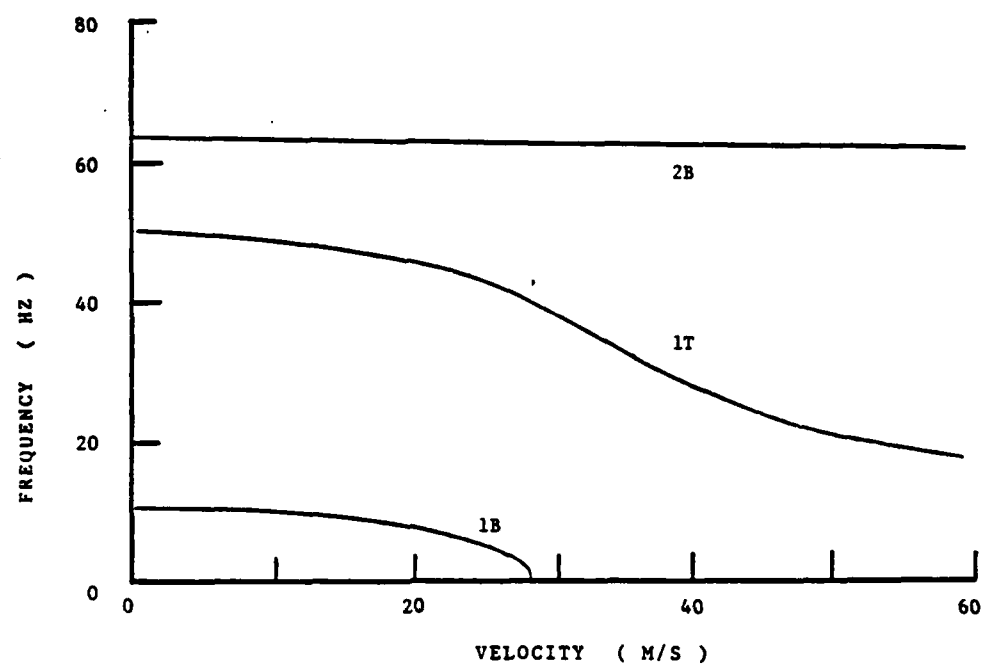


Figure D.24 $\Lambda = -30$, $[\pm 15/0]_s$ layup wing, V-g diagram.

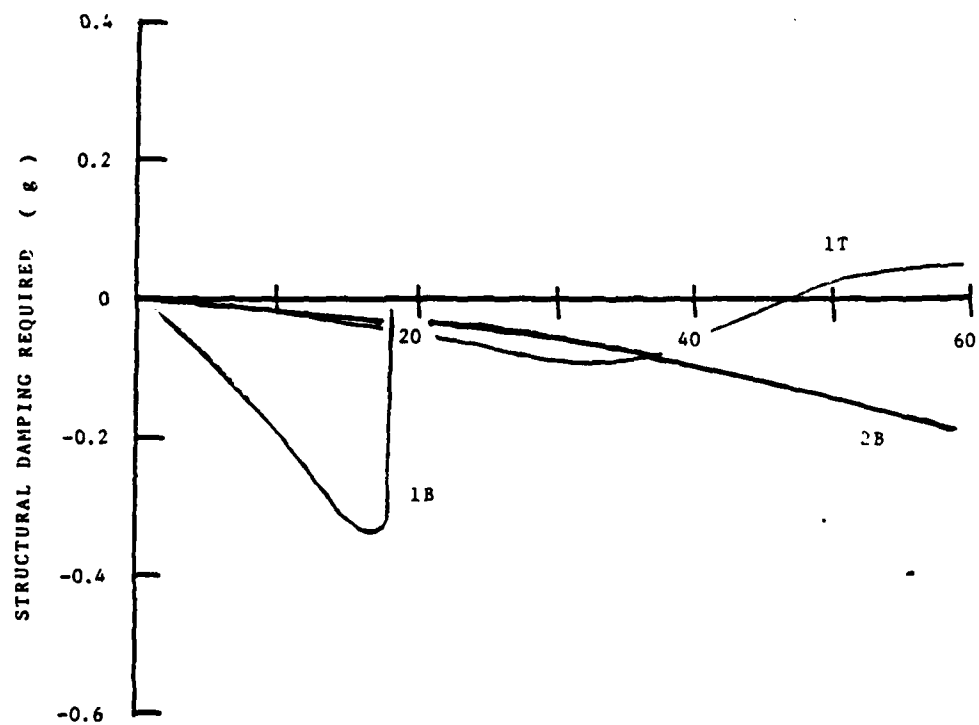
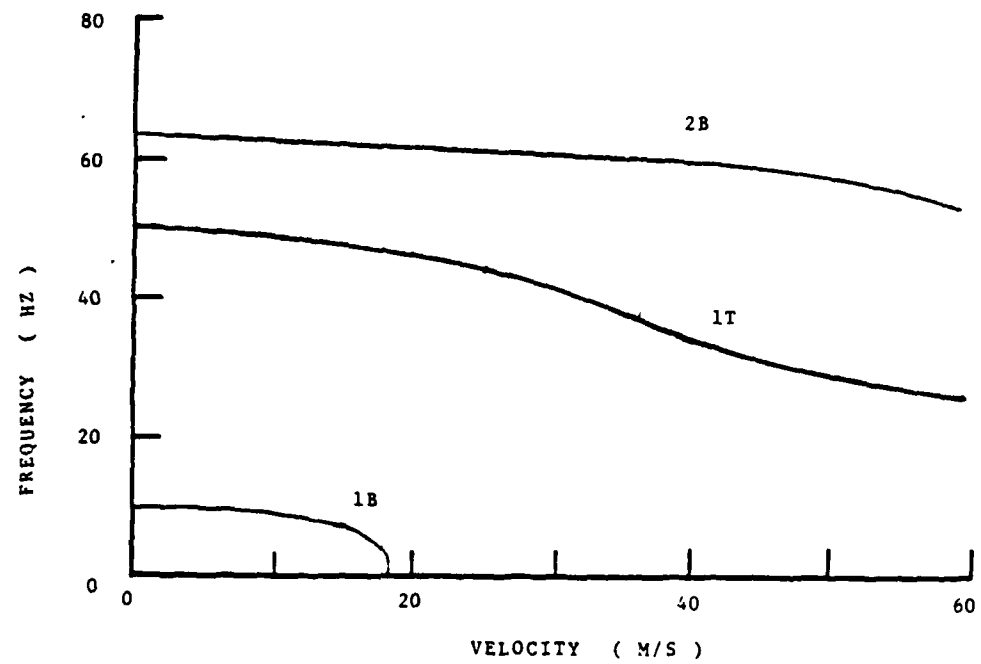


Figure D.25 $\Lambda = -30$, $[\mp 15/0]_s$ layup wing, V-g diagram.

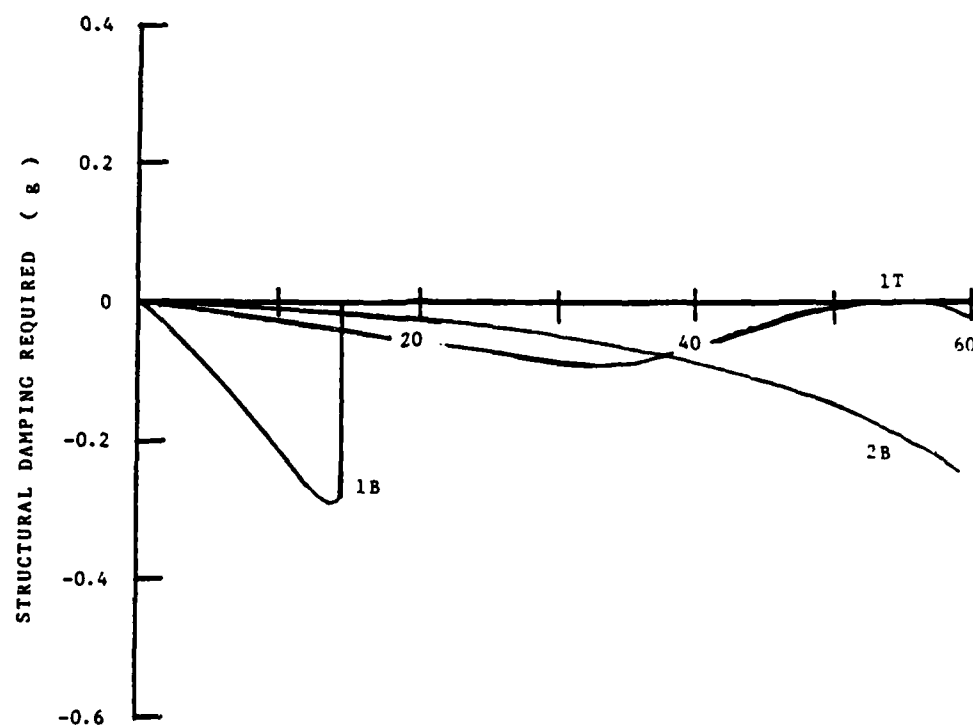
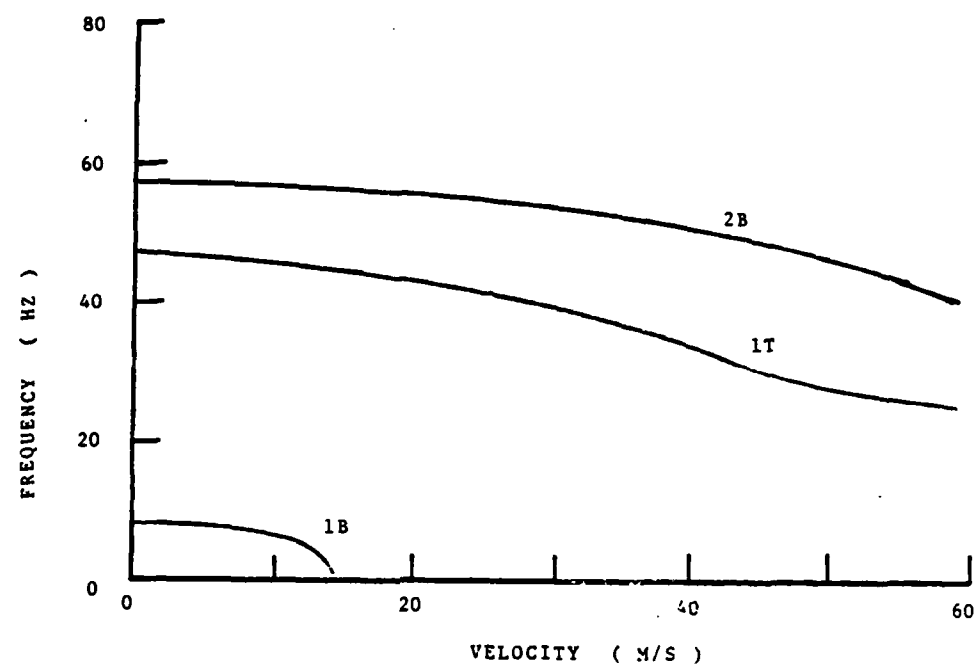


Figure D.26 $\Lambda = -30$, $[-15_2/0]$ s layup wing, V-g diagram.

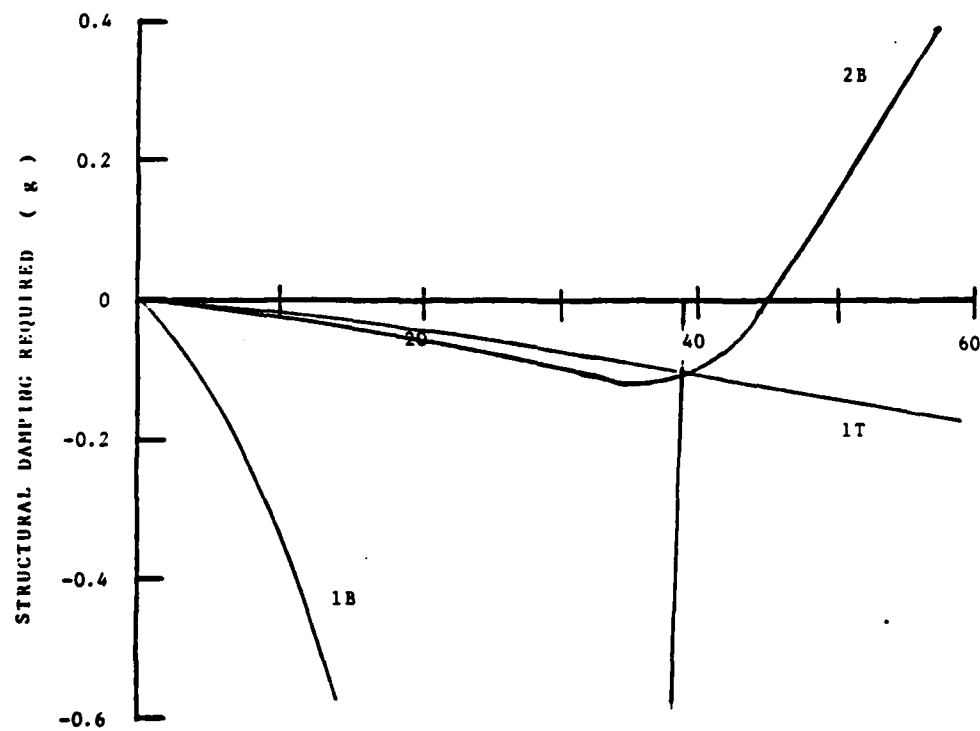
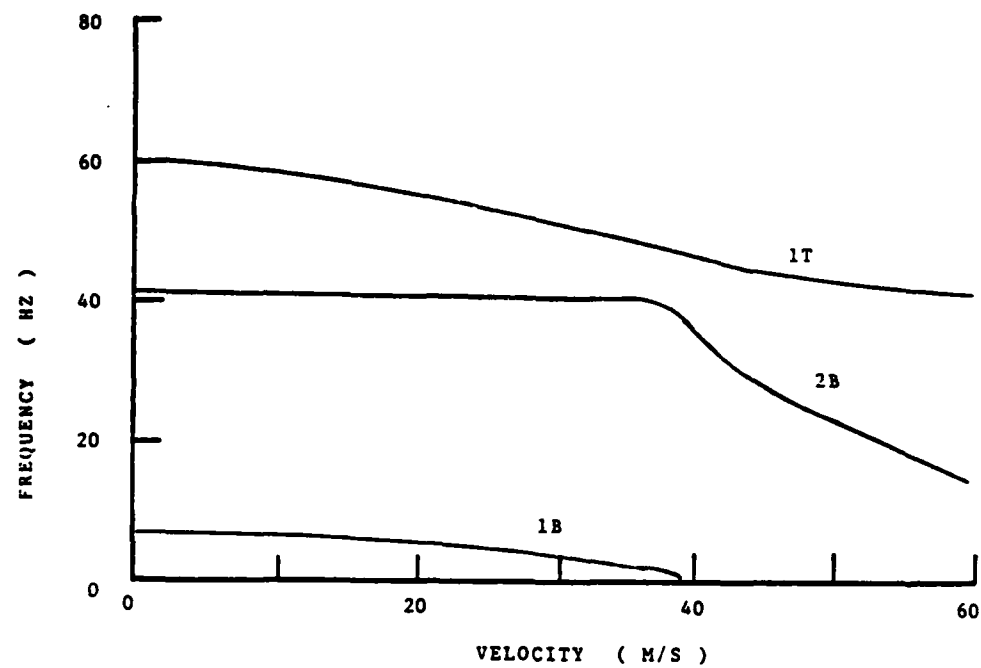


Figure D.27 $\Lambda = -30$, $[+30_2/0]$ s layup wing, V-g diagram.

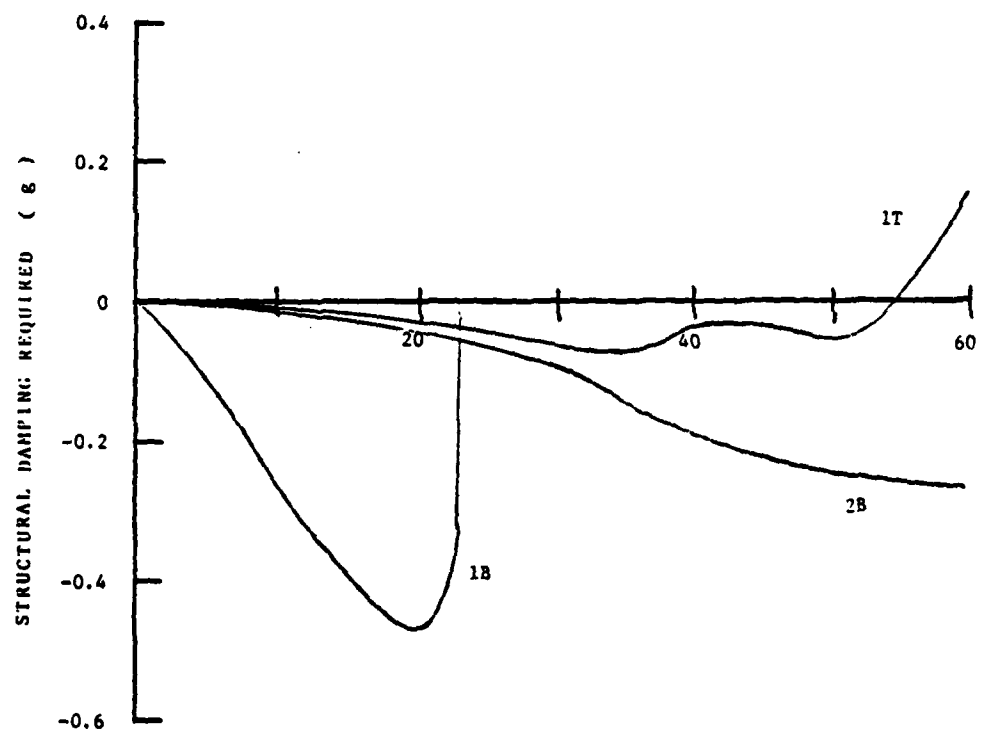
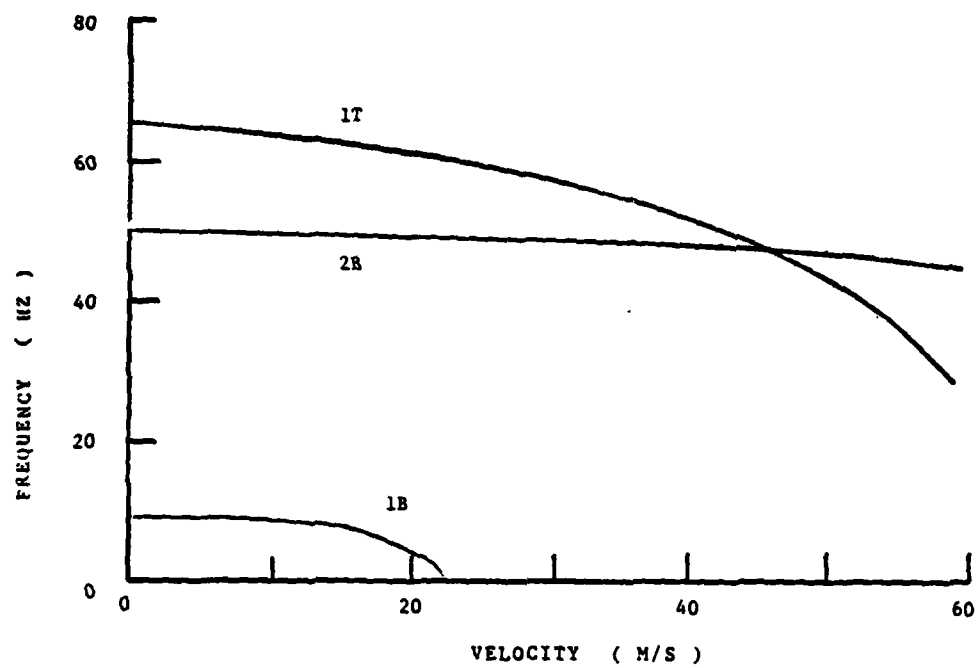


Figure D.28 $\Lambda = -30$, $[\pm 30/0]_s$ layup wing, V-g diagram.

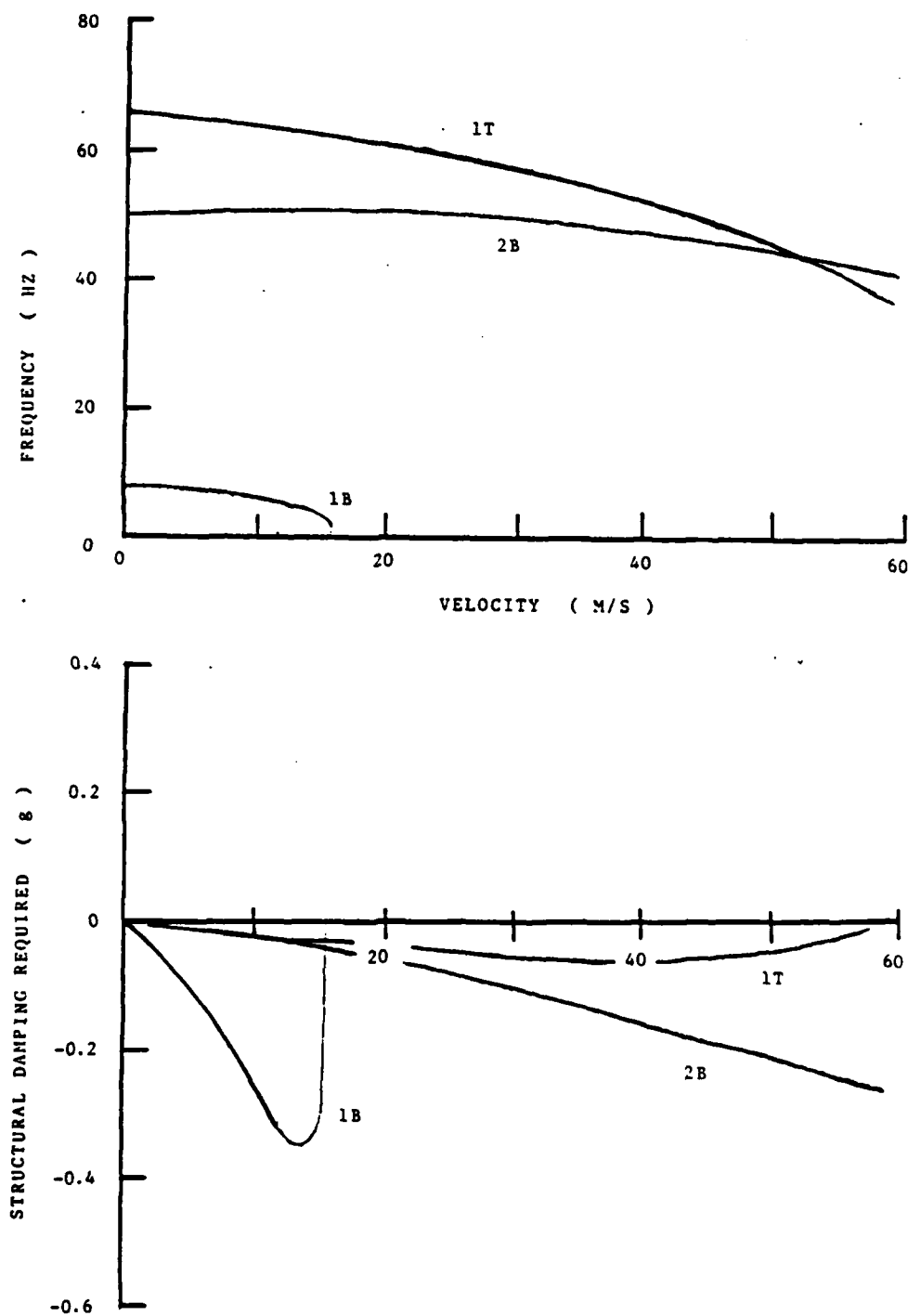


Figure D.29 $\Lambda = -30$, $[\mp 30/0]_s$ layup wing, V-g diagram.

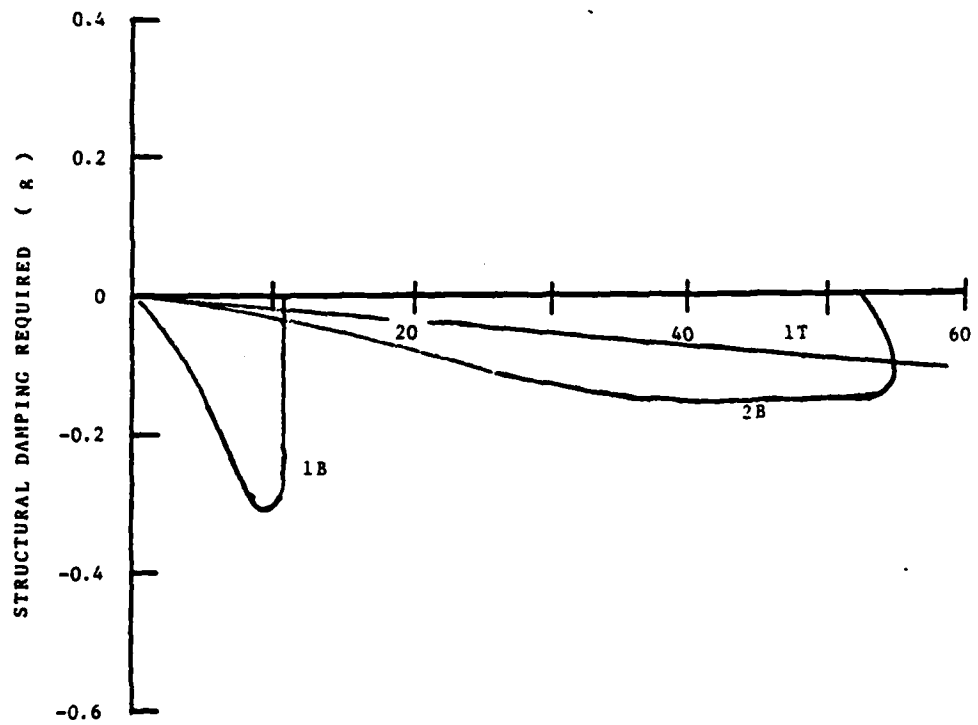
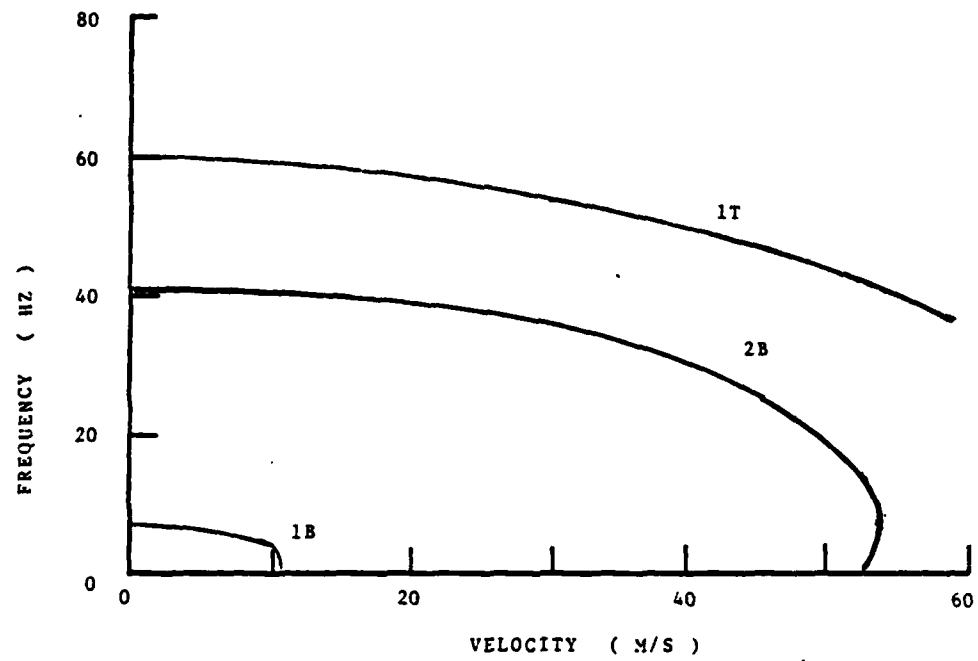


Figure D.30 $\Lambda = -30$, $[-30_2/0]_s$ layup wing, V-g diagram.

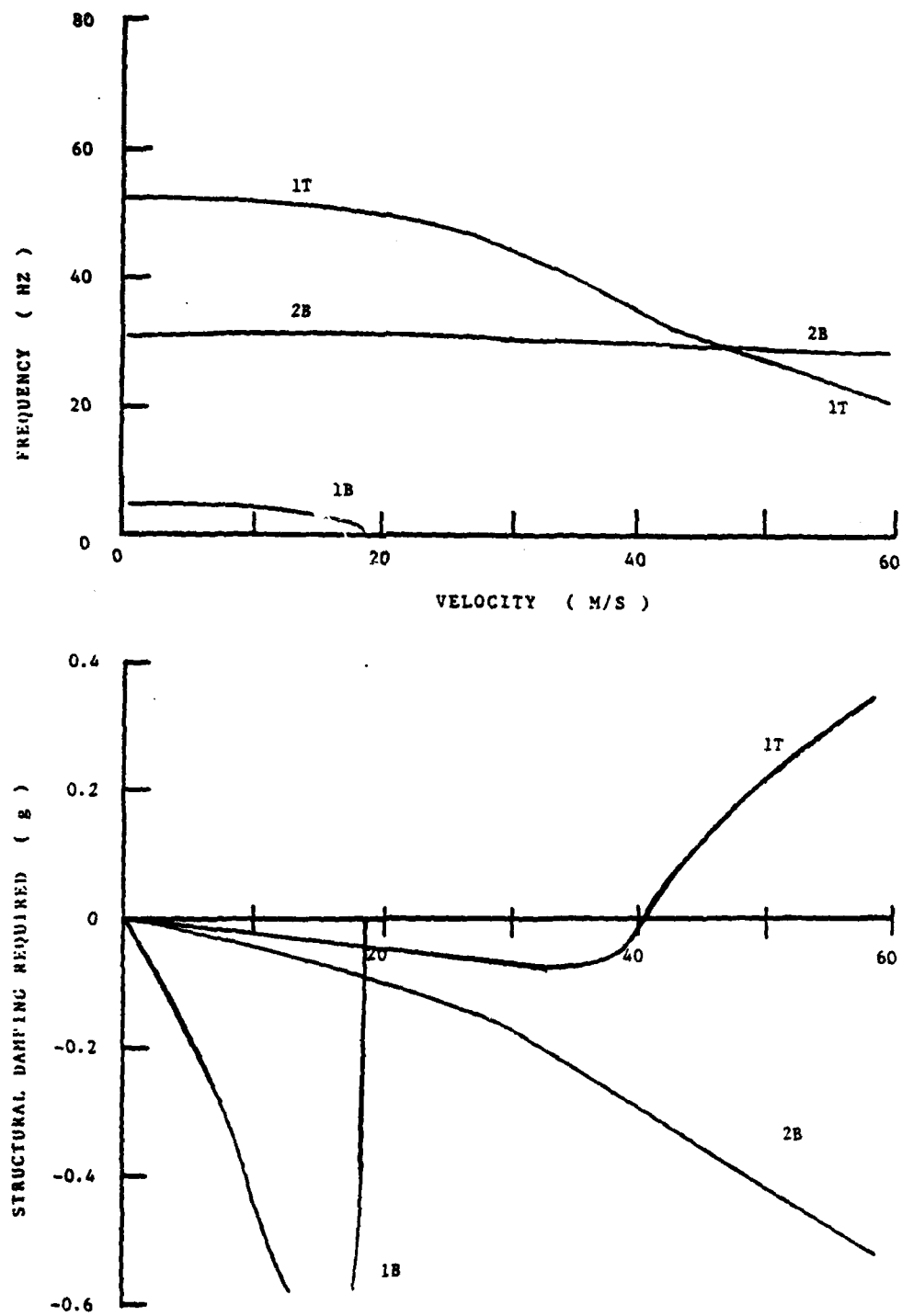


Figure D.31 $\Lambda = -30$, $[+45_2/0]$ s layup wing, V-g diagram.

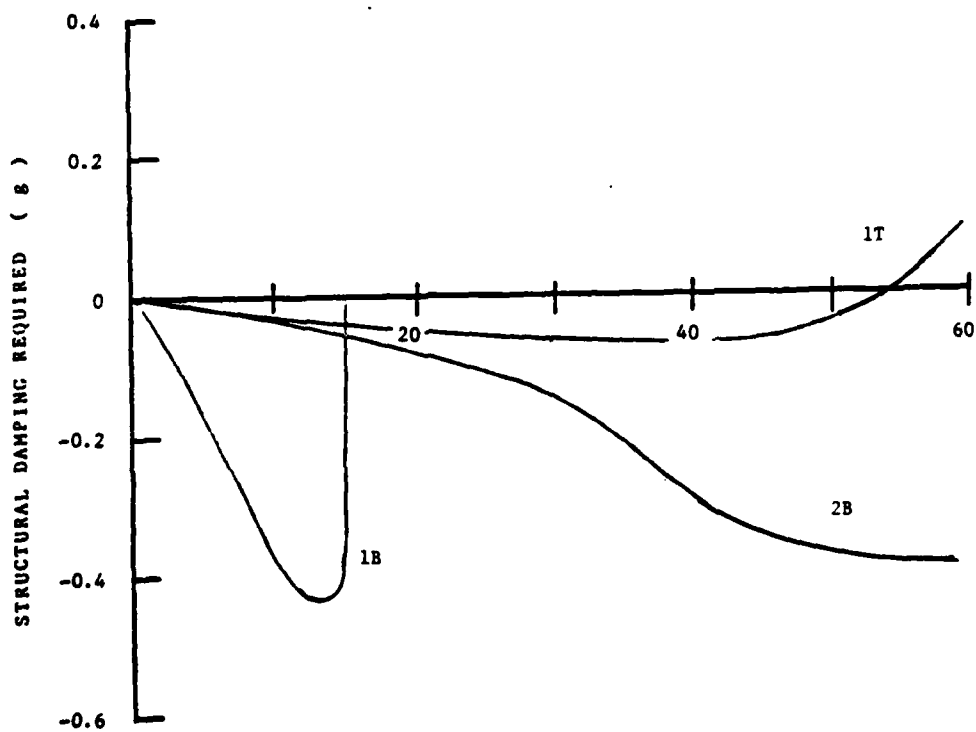
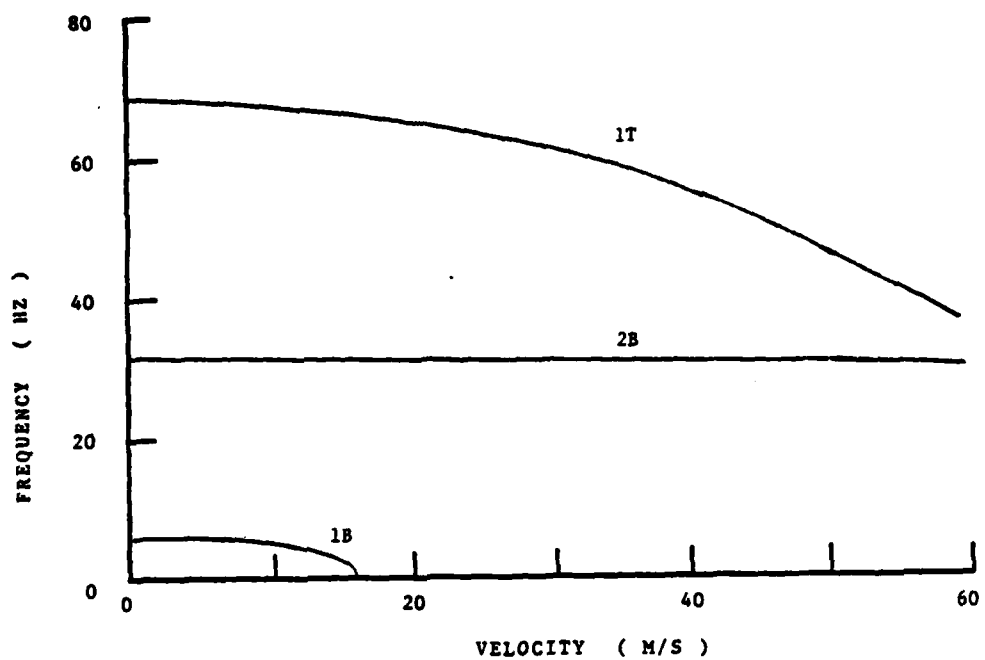


Figure D.32 $\Lambda = -30$, $[\pm 45/0]_s$ layup wing, V-g diagram.

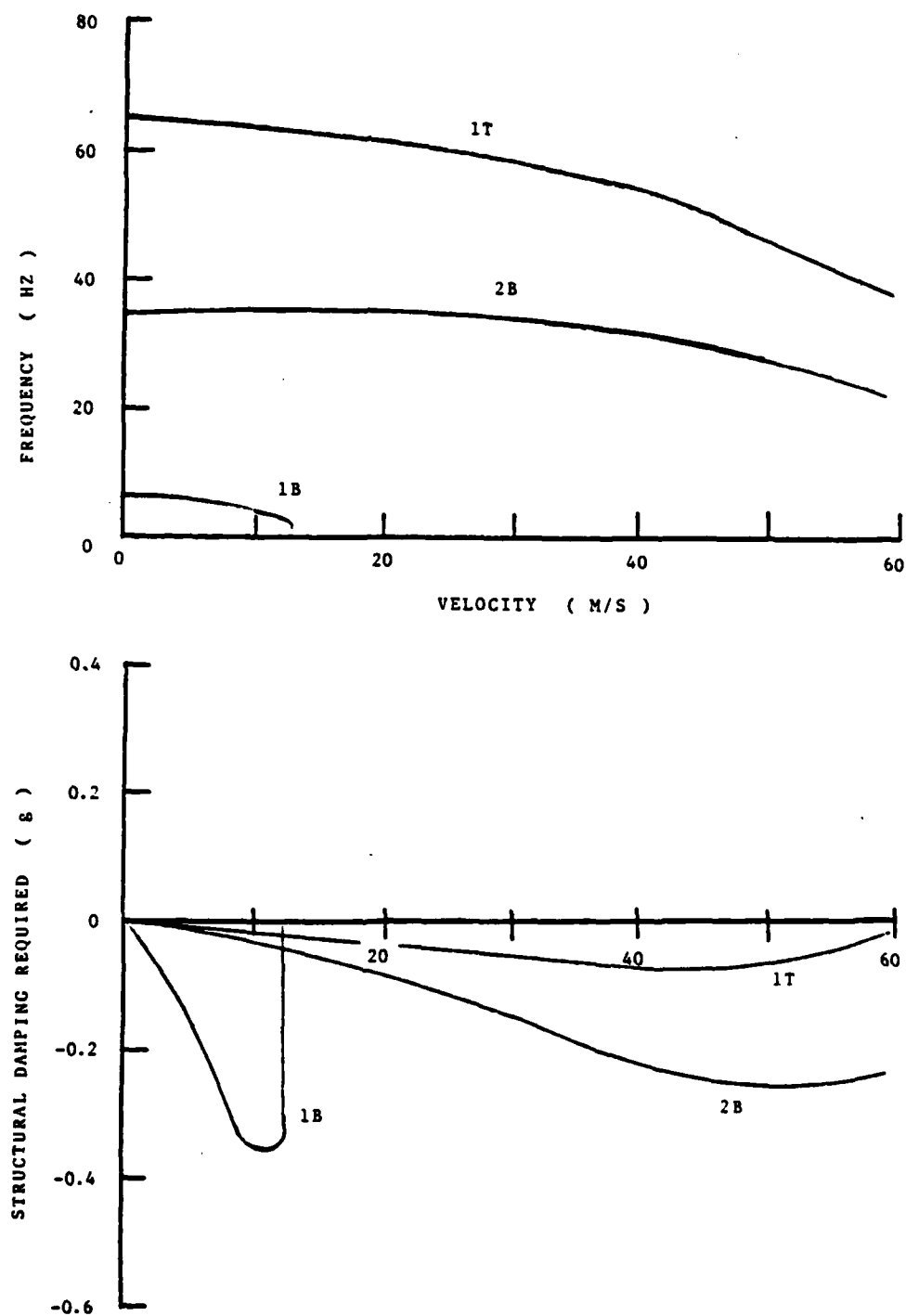


Figure D.33 $\Lambda = -30$, $[\mp 45/0]_s$ layup wing, V-g diagram.

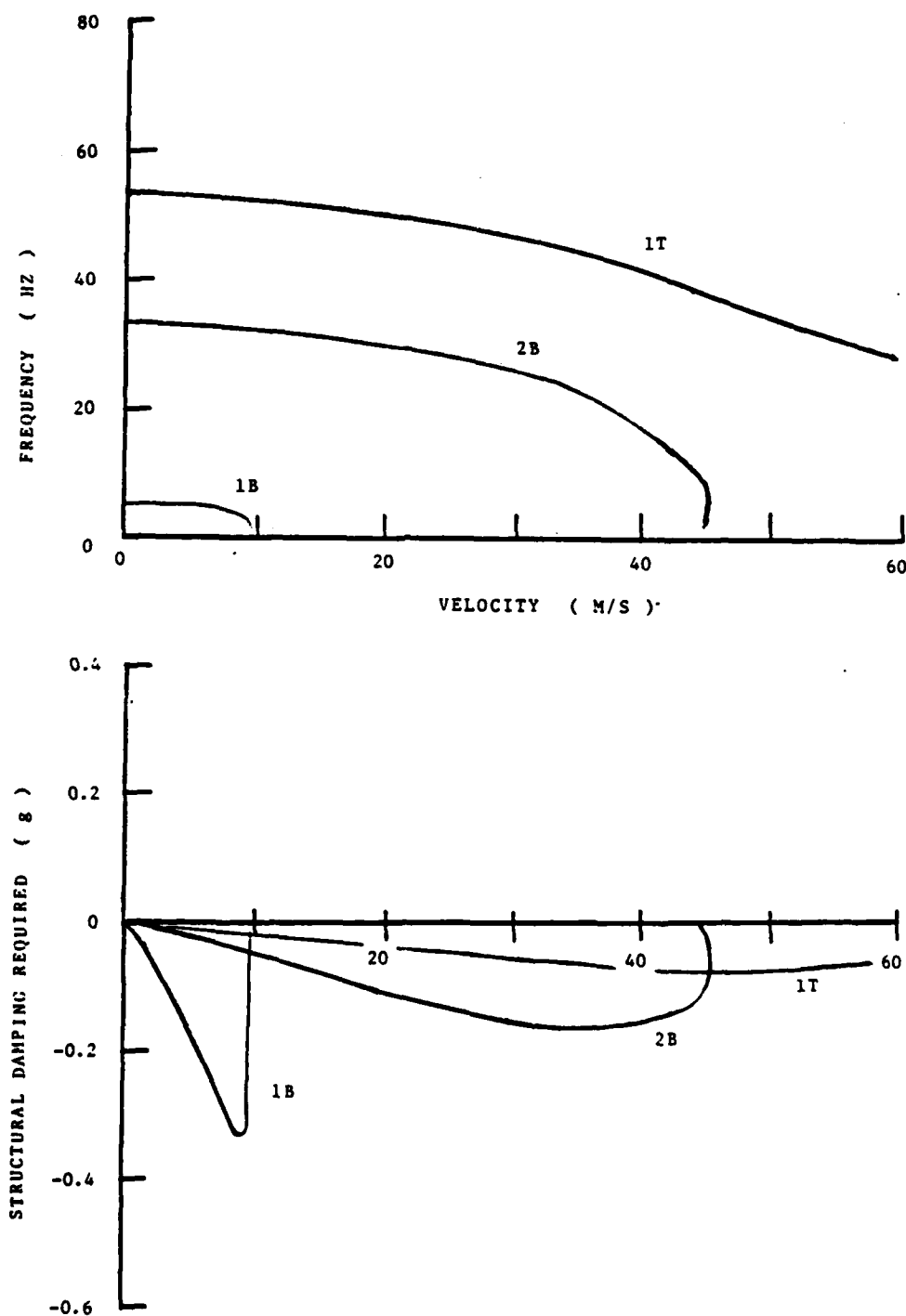


Figure D.34 $\Lambda = -30$, $[-45_2/0]$ s layup wing, V-g diagram.

ABOUT THE AUTHOR



Captain Brian J. Landsberger is an Air Force fighter pilot. Following graduation from the United States Air Force Academy in 1972, up to April of 1981 he has been flying for the Air Force. His expertise is in tactical aviation, having flown the F-4 Phantom and the OV-10 Bronco. This includes two assignments to The Republic of Korea where he was a forward air controller, an air liason officer for the 26th Korean Infantry Divison and a Flight Commander in the 497th Tactical Fighter Squadron. After returning from Korea, he entered the Massachusettes Institute of Technology, under the sponsorship of the Air Force Institute of Technology. While at M.I.T. he has worked in the M.I.T. Laboratory for Advances Composites (TELAC), concentrating on aeroelastic applications for composite material. From M.I.T. Captain Landsberger went to work for the Flight Test Center at Edwards Air Force Base, California.

